UNIVERSITY OF SOUTHAMPTON

Magnetoresistance in constrained domain walls

by

Yudong Wang

A thesis submitted in partial fulfillment for the degree of Doctor of Philosophy

in the

Faculty of Engineering and Applied Science

Department of Electronics and Computer Science

April 2013

UNIVERSITY OF SOUTHAMPTON

ABSTRACT

FACULTY OF ENGINEERING AND APPLIED SCIENCE
DEPARTMENT OF ELECTRONICS AND COMPUTER SCIENCE

Doctor of Philosophy

by Yudong Wang

In magnetic materials, domains of magnetic orientation in opposite direction are often alternated. The transition in orientation between these domains, the domain wall, is not abrupt but spatially extended. When a current is passed through the magnetic material, the resistance of the material is dependent on whether such domain wall exists, which in its turn depends on the external magnetic field. This magneto-resistance is larger for smaller domain walls. Although the domain wall width is in principle a materials parameter, by patterning the magnetic sample into certain nanostructures, it is possible to constrain the domain wall such that its width is smaller than its natural unconstrained width.

We have measured domain wall magnetoresistance in a single lithographically constrained domain wall. An H-shaped Ni nanobridge was fabricated by either e-beam lithography or a combination of e-beam lithography and helium ion milling. The two sides of the device are both single magnetic domains showing independent magnetic switching. The connection between the sides constrains the domain wall when the sides line up antiparallel. The magnetoresistance curve clearly identifies the magnetic configurations that are expected from a spin-valve like structure. The room temperature domain wall measurements give a magneto-resistance ratio of 0.1 % for the 94 nm and 0.2 % for the 32 nm constriction.

Although these values are in itself small, they are the first results on lithographically prepared single domain spin valves. The single-layered device might allow for easier fabrication and space savings for high dense storage applications as compared to giant magneto-resistance and tunneling magneto-resistance. Also, the research of spin-based logic devices will benefit from the physical understanding that follows from measurements of magneto-resistance devices without material interface.

To fabricate electrically functional devices on this size scale, significant development in the fabrication methods was required. The electron beam lithography for metal lift-off process is developed for the high resolution and accurate alignment work. A checkerboard dose sensor has been investigated to detect the base dose for the proximity effect correction in the e-beam lithography. A helium ion beam milling process is developed used to overcome the limitation of the e-beam lithography lift-off process. A resistance model has been used to measure the milling rate with layer accuracy of close to 1nm. The experimental He ion milling efficiency for Ni calculated from these measurements gave a value of 0.044 atoms/ion which is the half the value from finite element simulation.

The same advanced fabrication process has also been used to create a 20 nm gap in a plasmonic nanoantenna. Its resonant spectrum has been measured using optical methods and agrees very well with theoretical prediction based on the geometry of the nanoantenna. This fabrication also gives rise to the possibility to fabricate an electrical controllable plasmonic dimer nanoantenna and the design of such elecro-optical modulator is presented.

Contents

Declaration of Authorship

I, Yudong Wang, declare that the thesis entitled Magnetoresistance in constrained domain walls and the work presented in it are my own. I confirm that:

This work was done wholly or mainly while in candidature for a research degree at this University;

Where any part of this thesis has previously been submitted for a degree or any other qualification at this University of any other institution, this has been clearly stated;

Where I have consulted the published work of others, this is always clearly attributed;

Where I have quoted from the work of others, the source is always given, with the exception of such quotations, this thesis is entirely my own work; The plasmonic nano-antenna work includes the device fabrication which was done by myself, optical measurement and finite difference in time domain simulation carried out by Martina Abb and boundary element method simulation carried out by Pablo Albella. We were named on the same paper published at ACS nano at 2012 (included in the publication list).

I have acknowledged all main sources of help;

Where the thesis is based on work done by myself jointly with others, I have made clear exactly what was done by others and what I have contributed myself;

Parts of this work have been published in research journals as indicated in the list of publications provided with this manuscript.

Signed:

Date:

List of Publications

Journal Publications

Y. Wang, C. H. de Groot, D. Claudio-Gonzalez, & H. Fangohr, (2010). **Magnetoresistance in a lithography defined single constrained domain wall spin-valve.** *Applied Physics Letters*, 97(26), 262501. doi: 10.1063/1.3531666. (selected as frontier research and published in AIP (American Physical Society)'s Virtual Journal (http://www.vjnano.org))

N. Unal, M. D. B. Charlton, **Y. Wang**, U. Waizmann, T. Reindl, & U. Hofmann (2011). **Easy to adapt electron beam proximity effect correction parameter calibration based on visual inspection of a "Best Dose Sensor" .** *Microelectronic Engineering.* doi: 10.1016/j.mee.2011.02.066.

Y. Wang, S. A. Boden, D. M. Bagnall, H. N. Rutt & C. H. de Groot (2012) **Helium ion beam milling to create nano-structured domain wall magnetoresistance spin-valve** *IOP Nanotechnology* Vol.23, p395302 (selected as an article of particular interest and promoted as a news item on the website nanotechweb.org)

M. Abb, **Y. Wang**, P. Albella, C. H. de Groot, J. Aizpurua, and O. Muskens (2012) **Interference, coupling, and nonlinear control of high-order modes in asymmetric nanoantennas**, *ACS Nano* Vol.6, No.7 pp6462-6470

Conference Publications

Y. Wang, C. H. de Groot, D. Claudio-Gonzalez, H. Fangohr (2010) **Domain wall magnetoresistance E-beam Fabrication and MR measurement** *SEPNET Spintronics* 2010 London (poster)

Y. Wang, K. de Groot, H. Fangohr, D. Gonzalez (2011) **Magneto-resistance in a lithography defined single constrained domain wall spin valve.** *Conf. IEEE Intermag BD-07 Taipei*, Taiwan (oral)

Y. Wang, C. H. de Groot, D. Claudio-Gonzalez, R. R. J. Gibbs, H. Fangohr (2011) **Domain wall Magnetoresistance E-beam fabrication and MR measurement**, *IEEE Summer School* New Orleans, U.S.A.(poster)

Y. Wang, C. H. de Groot, D. Claudio-Gonzalez, H. Fangohr(2011) **Magnetoresistance in a lithography defined single constrained domain wall spin valve.** *EUROMAT 2011*, A24-0855, Montpellier, France (oral)

Y. Wang, C. H. de Groot, D. Claudio-Gonzalez, M.D. B. Charlton (2011) **Magnetoresistance in a lithography defined single constrained domain wall spin valve.** *SPIE 2011* San Diego, 8100-24 (Invited oral, Paper see SPIE Digital Lib.)

Y. Wang, C. H. de Groot, D. Claudio-Gonzalez, R. R. J. Gibbs, H. Fangohr (2012) **Magneto-resistance in a lithography defined single constrained domain wall spin-valve**, *JAIST ISEN 2012* Kanazawa, Japan (poster)

Y. Wang, S. A. Boden, D. M. Bagnall, H. N. Rutt & C. H. de Groot (2012) **Helium ion beam milling to create nano-structured domain wall magnetoresistance spin-valve** *NN 2012*, W2, Thessaloniki, Greece (oral)

Y. Wang, S. A. Boden, D. M. Bagnall, H. N. Rutt & C. H. de Groot (2012) **Helium ion beam milling and electron beam lithography to create sub-20nm sized domain wall magnetoresistance spin-valve** *MNE 2012*, Toulouse, France (poster)

Acknowledgements

I would like to express my sincerest gratitude for the help that people have given me. Without your caring support this thesis would not have been possible. A special thank to my supervisor Prof. Kees de Groot for his guidance, support, the innumerable helps throughout every step of my PhD research, study funding, correcting papers, daily life and this thesis. In particular, I am very appreciative of the intellectual freedom, patience, trust and encouragement which he has afforded during my whole graduate research. A special gratitude to Dr. Martin Charlton for his kind and patient supervision on the E-beam lithography system, pattern generator softwares and theory on proximity effect corrections, useful discussions on the science and support in both my study and daily life.

I would like to thank every member of the nano research group for their help, kindness and the happy times over the past 3 years. I want to give my thanks to Dr. Otto Muskens for his patient support and guidance on the plasnomic nanoantenna project. Thanks to Dr. David Gonzalez for all his support and suggestions on the domain wall magnetoresistance fabrications and analysis. Thanks to Dr. Martina Abb for her excellent cooperation during the plasmonic nanoantenna project. Thanks to Dr. Stuart Boden for the great collaboration of the HIM related projects and his patient help on experiment and improving the papers. Thanks to Dr. Harold Chong for his useful discussions on e-beam, FIB, MFM and AFM, and the helpful suggestions on my study. Thanks to Dr. Yoshishige Tsuchiya for the endless help on the cryogenic measurement system and discussions on signals and noises. Thanks to Prof. Hiroshi Mizuta for the discussions on spintronics and his kind invitation to the lab seminar in Japan. Thanks to Prof. Darren Bagnall and Prof. Harvey Rutt for the helium ion beam milling project. Thanks to Prof. Peter Ashburn for the MOSFET related discussions.

I would like to thank all the colleges who are working together in the cleanroom. I would like to give my thanks to Peter Ayliffe for all his help on e-beam lithography system; Sunkai for his endless help on photo-lithography, thermal oxidation and etching processes; Kian for all his useful helps on lithography, sample packaging, and machine lift-off processes; Ruiqi for the discussions on e-beam

lithography and pattern generator softwares; Yunpeng for the proof reading of the thesis; Stuart Pearce for his help on e-beam evaporators; Khaled for his discussions on magnetoresistance and e-beam lithography; Xiaoli for her discussions on the spintronics projects; Owain for his help on cleanroom instruments trainings; Jim for the help on evaporator; Zak for the graphene related discussions; Ruomeng, Yunpeng, Shuojin, Longtao, Xingzhao, Ahmed, Suhana, Ibrahim, Sara, Ioannis, Mario, Hwanjit, Feras, Taha, Ken, Nima, Mehdi, Kanad for all the helps and best times spent together in the cleanroom, office and bars.

I would like to dedicate this thesis to my loving wife Qiong Liu.

Chapter 1

Introduction

Spintronics is a fast growing research field which looks at both spin and charge signal of electrons. Especially as metal-oxide-semiconductor field-effect transistors (MOSFETs) technology is its limitation on par with the tunnelling distance of electrons. Spintronics provides an emergent possible solution to next generation of electronic logic by bridging the gap between classical MOSFET theory and the onset of the great significance of electron spins. Electron spin was discovered in the 1920s, but this physical phenomenon was not utilised in logical devices due to the lack of understanding until 1980s. One of the most important discoveries relating to the electron spin is magnetoresistance which is known as the resistivity variation caused by the interaction between electron spins and magnetisation. Giant magnetoresistance (GMR) awarded the 2007 Nobel Prize was firstly discovered by Grünberg *et al* in 1988. Almost at the same time in the year 1989, Fert's team reported a very large GMR effect [1]. In 1995 a tunnelling magnetoresistance (TMR) of 11.8% at room temperature was found by Moodera *et al* [2]. This then led to a significant increase in hard drive storage density, because of the use of TMR in its sensors. Soon after, the magnetoresistance attracted more and more researchers into various fields such as ballistic magnetoresistance (BMR), colossal magnetoresistance (CMR) and domain wall magnetoresistance (DWMR). Based on that research spin based logic device [3] became possible, and research on spintronics came into fruition.

In this thesis the basic theory about spintronics and popular research areas will be introduced. Among these areas there is a topic named domain wall magnetoresistance (DWMR). Domain wall magneto-resistance (DWMR) occurs when electrons travel from one side of the magnetic domain wall to another non-adiabatically. It has been reported in many different structures such as ring structure [4, 5, 6],

line structure [7, 8, 9, 10, 11, 12], atom-contact structure [13, 14], zigzag structure [15, 16] and bridge structure [17, 18]. In 1999, Bruno [19] proposed that in nano-structured devices the domain wall width can be constricted by geometrical means. The decrease of the domain wall width could exponentially increase the domain wall magnetoresistance according to the models of Morosov's reported in 2004 [20], and Ieda's reported in 2007 [21]. However both of these models are theoretical, because the fabrication of a measurable single constricted domain wall device is challenging. In line-shape devices, the DWMR effect is relatively small because the classic resistance of the line hides it. In the point connecting structures the magnetoresistance can be very large due to the ballistic transport of the electrons, but it is not caused by domain wall due to the adiabatical transport of the electrons. Moreover the fabrication procedures such as mechanical break junctions [22], electrical break junctions [23] and electrochemical junctions [24] are not suitable for industrial fabrications [25], and the measurements are subject to artefacts [26]. In this work an H-shaped single domain wall magnetoresistance spin-valve is analysed experimentally. It is fabricated by industrial capable top down processes and measured by a four point measurement circuit. The domain wall width of our spin-valve can be controlled by the length of the bridge between two domain pads [18]. Both electron beam lithography and helium ion beam milling methods are used in order to reduce the bridge length down to sub-20 nm region. The research based on such a device could not only benefit the understanding of physics of DWMR but also give possibilities to fabricate faster and denser logical devices.

This thesis contains the analysis, fabrication and measurement of the H-shaped DWMR devices. In Chapter 2 basic magnetism, magnetoresistance and the latest research of DWMR will be introduced. Chapter 3 contains fabrication processes for H-shaped devices, especially methods to control the geometrical sizes, such as electron beam lithography and helium-ion beam milling. In Chapter 4, the device's magnetoresistance behaviour will be presented and discussed. A model based on spin energy transition will be introduced as well. In Chapter 5 a nano-antenna related to thin film surface plasmonic resonance research will be introduced. The nano-antenna can be fabricated by the electron beam lithography and helium ion beam milling. The structure of the nano-antenna is similar to our H-shaped DWMR spin-valve but no bridge between two antenna rods. As similar to DWMR effect, the plasmonic interaction signal can be significantly increased by reducing the width of the gap between two antenna rods down to sub-20 nm.

Chapter 2

Magnetism and electron-spins

2.1 Background

When we want to discuss domain wall magnetoresistance (DWMR), we should explain firstly what the domain wall is. However, before we could describe the magnetic domain and domain wall, we have to start with magnetisation in ferromagnetic materials. In magnetic view the materials being discussed here include non-magnetic, paramagnetic, ferromagnetic and antiferromagnetic materials. The magnetisation inside the material can be divided into two contributions, spin orbital moment and spin moment. In paramagnetic material the directions of spin orbital and spin moment are random because of the thermal energy. The sum of the total amount of these vectors is zero, so the total magnetisation is zero. Below a critical temperature the vectors start to align themselves along certain directions and the paramagnetic material becomes a magnetic material. The critical temperature is named the Curie temperature (T_c). T_c of nickel which we used in this experiment is 627 K. Below T_c the magnetic interaction between spins in the magnetic material can be described by several energy terms. This interaction will determine the orientations of the magnetisation inside the magnetic material such as the formation of domain walls. Below we are going to discuss in detail how the energy terms influences the magnetisation.

2.2 Energy states in magnetic materials

The magnetisation in the magnetic material follows a common principle that its total energy in a finite space prefers the lowest state. In ferromagnetic materials this means changing the direction of each cell's magnetisation. However, the stable state may not be the state at minimum energy. There might be several local minimal stable states in a system (Figure 2.1). We define the local minimal stable states at points where $\frac{\partial E}{\partial \theta} = 0$ and $\frac{\partial^2 E}{\partial \theta^2} > 0$. To change the system from one state to another needs external energy, such as thermal energy, external magnetic field or current spin torque.

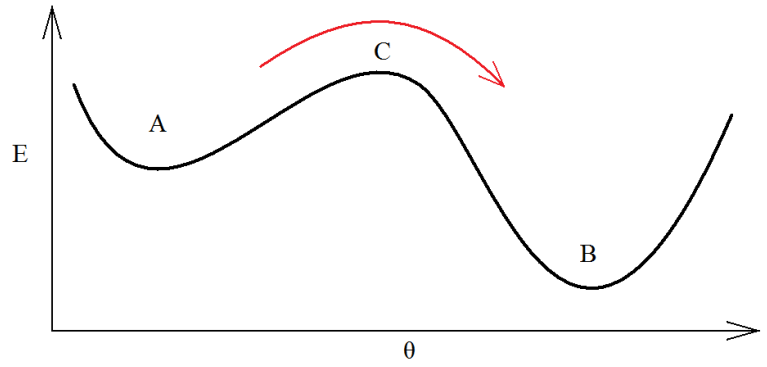

FIGURE 2.1: A plot of Energy E, as a function of angular θ of a finite magnetic system. State A is a local minimum energy state while State B is the lowest stable state. State C is the energy barrier between states A and B. The system requires additional energy which is as least the difference between states C and A to move from state A to state B

In our experiment the device will be operated in an external magnetic field. The total energy we are discussing here can be shown as,

$$E_t = E_{ex} + E_a + E_z \tag{2.1}$$

where E_t is the total magnetic energy, E_{ex} is the exchange energy which aligns the magnetisation of the neighbouring cells parallel or antiparallel to each other, E_a is the anisotropy energy which forces the magnetisation to follow the lattice direction, geometrical easy direction or strain direction and E_z is the Zeeman energy which forces the magnetisation to follow the external magnetic field. The details are explained below.

Exchange interaction is a kind of strong quantum mechanical interaction within a finite magnetic domain. The interaction exists between any two magnetic cells.

The cell size could be as small as one atom. However, in most simulations we have to define the cell size as large as several nano meters in order to reduce the calculating time. The value of E_{ex} can be calculated from the Heisenberg Hamiltonian (Equation 2.2).

The Heisenberg Hamiltonian as a function of angle between neighbour cells' magnetisation, θ and is given by,

$$\begin{aligned} H_{ex} &= -2\sum_{j>i} J_{ij} S_i \cdot S_j \\ &= -2JS^2 \sum_{j>i} \cos\theta_{ij} \\ &= -2JS^2 \sum_{j>i} (1 - \sin^2\frac{\theta_{ij}}{2}) \\ &\approx \frac{1}{2} JS^2 \sum_{j>i} \theta_{ij}^2 + C \end{aligned} \tag{2.2}$$

where S_i and S_j represent spins of two distinct atomic sites and J is the exchange integral of the overlap of the wave functions of the i^{th} and j^{th} atoms. When $J > 0$ the material is ferromagnetic whereas $J < 0$ correspond to antiferromagnetic materials. θ_{ij} is the angle between spin i and j.

If we consider one dimension in a 3-D space, the total exchange energy can be described by the sum of exchange energy of the nearest neighbour spins shown as [27],

$$E_{ex} = \int \frac{N_v JS^2}{2} (a\nabla\theta)^2 dL \tag{2.3}$$

where N_v is the density of the nearest neighbour spins, a is the spin lattice constant, L is the length of a row of a^3 cells and $A = a^2 N_v JS^2/2$ is the exchange stiffness. When we extend this model into three dimensions the equation can be written as [28],

$$E_{ex} = A \int (\nabla m)^2 dV \tag{2.4}$$

where $m = M/M_s$ is the saturation magnetisation constant. When the spin lattice constant a is relatively small (e.g. 4 nm),$\nabla\theta \approx \nabla m$.

E_a can be divided into three parts (Equation 2.5). These are magnetostatic energy

E_{ms} magnetocrystalline energy E_{mc} and magnetoelastic energy E_{me}.

$$E_a = E_{ms} + E_{mc} + E_{me} \tag{2.5}$$

The E_{ms} reduces the surface magnetic charge which generates a demagnetizing field through the magnetic material. The magnetic charge is caused by one end of a magnetic dipole at the surface of a piece of magnetic material. The demagnetizing field which is anti-parallel to the magnetisation orientation inside the material results in the magnetostatic energy E_{ms} (Equation 2.6). When the magnetisation follows a certain direction the system has the lowest anisotropy energy. We call this direction easy axis. Normally in a bulk structure (Figure 2.2), if the magnetocrystalline and stress anisotropy is negligible the easy direction will be along the long axis like Z. This is because the XY plane has less total magnetic charge than the XZ or YZ plane and the demagnetisation field is weaker along the easy direction Z compared to X and Y.

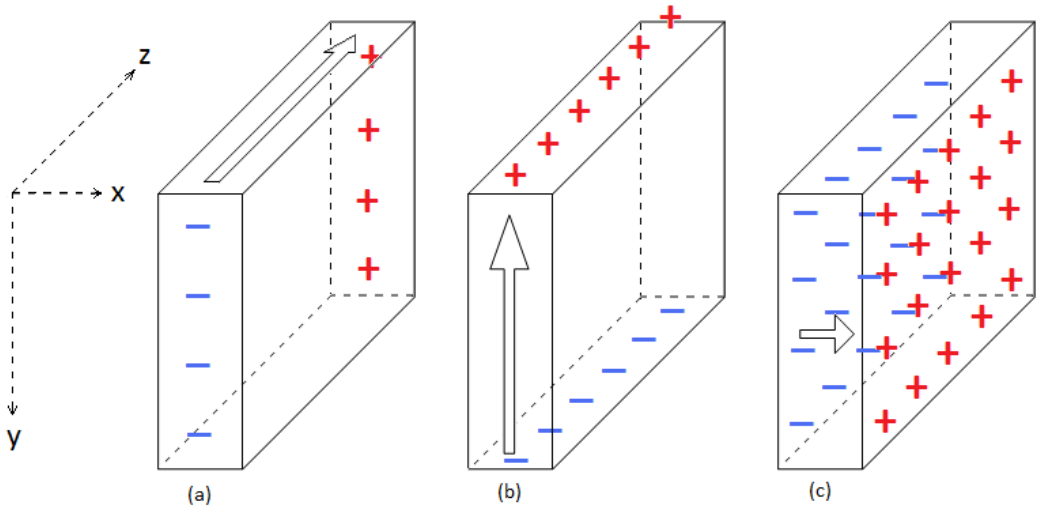

FIGURE 2.2: The schematic 3D diagram of surface magnetic charge and demagnetisation field. The geometrical size of the cube has the relation of $L_z > L_y > L_x$. The plane area has the relation of $S_{xy} < S_{xz} < S_{yz}$. Z is the easy axis because S_{xy} has the smallest amount of surface magnetic charge

The magnetostatic energy is given by,

$$E_{ms} = -\frac{1}{2}\int_{sample} \mu_0 H_d \cdot M dV = \frac{1}{2} N \mu_0 M_s^2 \tag{2.6}$$

where H_d is the demagnetisation field, M is the magnetisation of the domain and N is the demagnetizing factor depending on the shape of the magnetic material.

N's value is smaller when there is less surface magnetic charge. For example in Figure 2.2 the geometrical length of the cube is $L_z > L_y > L_x$ and the demagnetizing factor has the relation of $N_x > N_y > N_z$. M_s is the saturation magnetisation which depends on the type of the material.

The E_{mc} forces the the magnetisation to align with the crystal. The energy is mostly caused by the spin-orbit coupling. Different crystal lattices have different forms of magnetocrystalline energy. The energy in a uniaxial lattice can be shown as,

$$\begin{aligned} E_{u\_mc} &= \int K_1 \left(\cos^2\varphi \sin^2\theta + \sin^2\varphi \sin^2\theta\right) dV \\ &= \int K_1 \sin^2\theta dV \end{aligned} \tag{2.7}$$

where E_{u_mc} is the uniaxial magneto-crystalline energy, K_1 is a constant depending on material and temperature, whose unit is J/m^3. When $K_1 > 0$ the easy direction follows the Z axis whereas when $K_1 < 0$, the easy axis is within plane A (Figure 2.3). In this figure, Z is the main symmetry axis of the magnetic crystal. θ is the angle between the magnetisation and Z axis. A is the basal plane perpendicular to the symmetry axis.

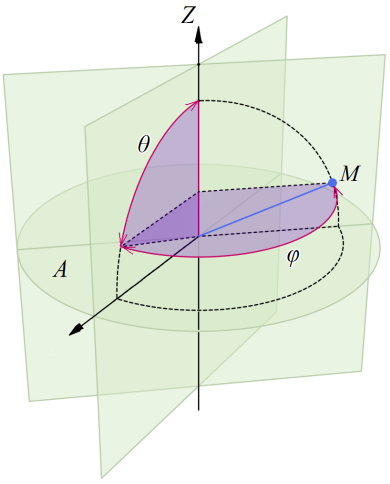

FIGURE 2.3: Spherical polar coordinates of the uniaxial lattice. Z is the main symmetry axis of the magnetic crystal. θ is the angle between the magnetisation and Z axis. A is the basal plane perpendicular to the symmetry axis.

E_{mc} in a hexagonal lattice is given by,

$$E_{h\_mc} = \int \left(K_1 \sin^2\theta + K_2 \sin^4\theta + K_3 \sin^4\theta \cos 6\theta\right) dV \tag{2.8}$$

where K_1 and K_2 are energy density constants. The hexagonal magnetocrystalline

energy, E_{h_mc} is dominated by the first two terms. The influence of higher order terms is largely reduced by thermal agitation. Table 2.1 shows how K_1 and K_2 determine the magnetic characteristic of the lattice. Figure 2.4 shows the hexagonal lattice structure and easy axes of its. For example, the cobalt lattice has parameters of $K_1 = 45 \times 10^4 J/m^3$ and $K_2 = 15 \times 10^4 J/m^3$, and thus the symmetric axis is its magnetic easy axis.

TABLE 2.1: Easy directions of a hexagonal lattice depending on energy density constants

Condition	Easy axes
$K_1 = K_2 = 0$	isotropic
$K_1 > 0$ and $K_2 \geq 0$	c (symmetry axis)
$K_1 < 0$ and $K_2 \leq 0$	a (basal plane)
$K_1 K_2 < 0$	b (easy cone)

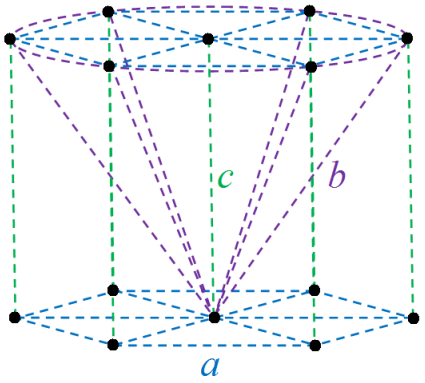

FIGURE 2.4: hexagonal lattice. c is a sixfold rotation symmetry axis, a is the lattice direction in the basal plane, b is the cone direction

The energy in a cubic lattice can be given as,

$$E_{c\_mc} = \int \left[K_1 \left(\alpha^2\beta^2 + \beta^2\gamma^2 + \gamma^2\alpha^2\right) + K_2\alpha^2\beta^2\gamma^2\right] dV \tag{2.9}$$

where K_1 and K_2 are energy density constants, $\alpha = \cos\varphi \sin\theta$, $\beta = \sin\varphi \sin\theta$ and $\gamma = \cos\theta$. α and θ are the angles in spherical polar coordinates. If K_2 is negligible, when $K_1 > 0$ the easy axis is the $< 100 >$ direction and when $K_1 < 0$ it is the $< 111 >$ direction. In other situations, the easy axis follows the α and θ when $\frac{\partial E}{\partial \theta} = 0$ and $\frac{\partial^2 E}{\partial \theta^2} > 0$. For example, for Fe $K_1 = 4.5 \times 10^4 J/m^3$ and $K_2 = \pm 0.5 \times 10^4 J/m^3$. K_2 can be neglected, therefore $< 100 >$ direction is the easy axis.

The E_{me} (Equation 2.10) forces the magnetisation to follow the strain directions.

This is defined by,

$$E_{me} = \frac{3}{2}\lambda_s \sigma \cos^2\theta \tag{2.10}$$

where λ_s is the saturation magnetostriction, σ is the strain, θ is the angle between the magnetisation and the strain direction.

At last, the Zeeman energy aligns the magnetisation to the external magnetic field. It can be calculated by,

$$E_z = -\int \mu_0 H \cdot M dV = -\int \mu_0 H M_s \cos\theta dV \tag{2.11}$$

where H is the external magnetic field, M is the magnetisation, M_s is the saturated magnetisation, θ is the angle between magnetisation and the external field.

TABLE 2.2: Summary of energy terms and their influence on the magnetisation

Energy term		Influence to magnetisation
Exchange		neighbours to follow the same direction
Anisotropy	magnetostatic	to follow the geometrical easy axis
	magnetocrystalline	to follow certain lattice directions
	magnetoelastic	to follow the strain direction
Zeeman		to follow the external magnetic field

2.3 Magnetic domain wall

Magnetic domain wall is a region in the ferromagnet materials, in which the magnet polarisation switches from one direction to another. Firstly pointed out by Bloch in 1932 [29], the structure of the domain wall is determined by the interaction between exchange and anisotropy. The width of the domain wall, W_{dw}, can be defined by [19],

$$W_{dw} \equiv 4\left[\int_{-\infty}^{+\infty} \dot{\theta}^2(x)\, dx\right]^{-1} = 4\left[\int_{-\frac{\pi}{2}}^{+\frac{\pi}{2}} \dot{\theta}^2 d\theta\right]^{-1} \tag{2.12}$$

where $\dot{\theta}$ is the magnetisation rotation angle between two neighbouring cells, and dx is the distance between the two cell. This is the definition of the domain wall width of a magnetic domain wall in an infinite system where at $-\infty$ the angle of magnetisation is $-\pi$ whilst at $+\infty$ the angle is π.

In a piece of ferromagnetic material, there might be any number of magnetic domain walls, or even no domain wall at all. This depends on the material as well as its geometrical size and shape. An unconstrained domain wall usually appears in a large sized system where the exchange energy E_{ex} dominates the anisotropy energy E_a. In bulk ferromagnets, the domain walls can be seen as unconstrained. For Ni, the material used in our experiment, the unconstrained domain wall width was found to be 134.1651 nm theoretically by Fangohr *et al* [30]. The simulation was done in OOMMF with the parameter $M_s = 490$ kA/m, $A = 9 \times 10^{-12}$ J/m, and $K = 2000$ J/m^3. This result agreed with the value 134.1641 nm calculated by Equation 2.13 reported by Bruno in 1999 shown as [19],

$$W_{dw_0} = 2\sqrt{A/K} \tag{2.13}$$

where A is the exchange stiffness and K is the uniaxial anisotropy. This equation comes from the definition shown in Equation 2.12 when the sum of exchange energy and uniaxial anisotropy energy is the minimum value. The demagnetisation is not taken into account in the unconstrained domain wall.

If we think about a finite system and the domain wall is highly constrained, the definition of domain wall width can be W_{dw} where the angle of magnetisation θ rotates from 0° to 180° ($[0, \pi]$). If we assume a constant value of $d\theta/dL$, in the uniaxial crystal it can be calculated by the equations below. The exchange energy caused by the spins inside the domain wall is derived from Equation 2.2,

$$E_{ex} = A\int_{-\infty}^{\infty} \nabla\theta^2 dL = A\sum_{n=1}^{N}\left(\frac{\pi}{N}\right)^2 a = A\frac{\pi^2}{N}a \tag{2.14}$$

where a is the lattice constant, N is the number of lattice along the width of domain wall. The uniaxial magnetocrystalline energy is derived from Equation 2.7,

$$\begin{aligned} E_{u\_mc} &= K\int \sin^2\theta dV = Ka^3\sum_{n=1}^{N}\sin^2\frac{n\pi}{N} \\ &= Ka^3\sum_{n=1}^{N/2}\left[\sin^2\frac{n\pi}{N} + \sin^2\left(\frac{n\pi}{N}+\frac{\pi}{2}\right)\right] \\ &= Ka^3\sum_{n=1}^{N/2}\left[\sin^2\frac{n\pi}{N} + \cos^2\frac{n\pi}{N}\right] = \frac{1}{2}KNa^3 \end{aligned} \tag{2.15}$$

In order to change the integration to a sum we assume θ is constant in a cross sectional area perpendicular to the domain wall width direction.

The minimum energy state is given as,

$$E' \equiv E'_{ex} + E'_{u\_mc} = -A\frac{\pi^2}{N^2}a + \frac{1}{2}Ka^3 = 0 \tag{2.16}$$

As it is an unconstrained domain wall in a infinite system, the minimum energy should be at a single point. The domain wall width which gives minimum total energy is given as,

$$W_{dw_0} = Na = \sqrt{2}\pi\sqrt{\frac{A}{K}} \tag{2.17}$$

It can be seen that the exchange energy of a domain wall is minimised by compelling the number of spins along the domain wall width as large as possible whereas the anisotropy energy prefers a small value of N leading to a short W_{dw_0}.

This value is about double Bruno's result (Figure 2.5). With this method the W_{dw} only counts the sharp rotating area which is believed to be the main contribution to the domain wall magnetoresistance, but neglects the region where the rotating is not obvious. Especially in a nano-meter sized finite system where the domain wall is not completely from 0° to 180°, the description of the sharp rotating area only is more accurate to discuss the spin transport (to be discussed in detail in the result section). There are two types, Bloch-type and Néel-type of domain walls.

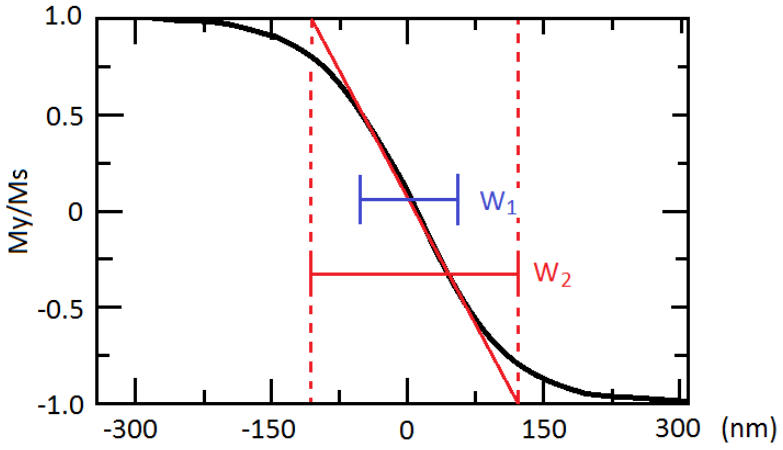

FIGURE 2.5: Schematic diagram of the unconstrained domain wall width in an infinite system defined by Bruno, $W_1 = 2\sqrt{A/K}$(blue) and in a finite system, $W_2 = \sqrt{2}\pi\sqrt{\frac{A}{K}}$

Figure 2.6a shows the structure of a Bloch-type domain wall. This type of domain wall appears when the exchange energy of rotations along xy plane exceeds the anisotropy energy of magnetisations in xz plane. It is more likely to appear in the

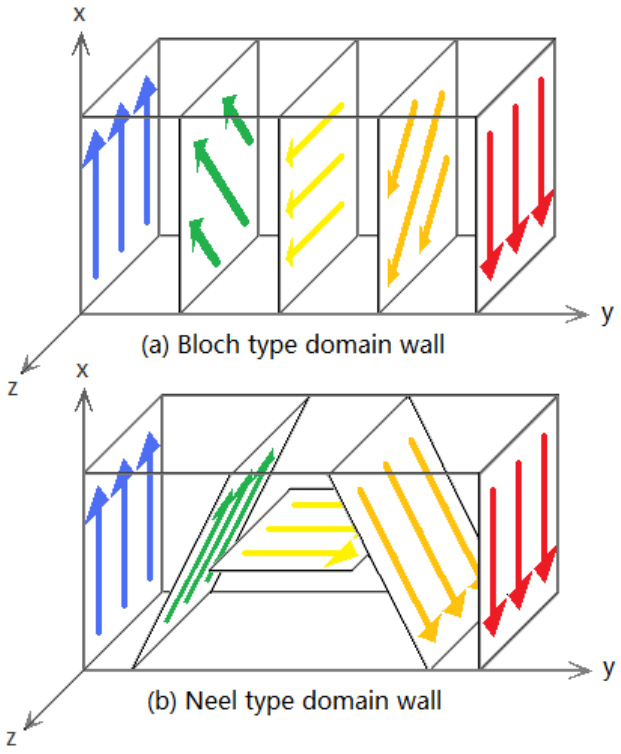

FIGURE 2.6: (a) Schematic 3D diagram of a Bloch type domain wall. The rotation of magnetisation is in XZ plane. The domain wall width direction is in Y axis. (b) Schematic 3D diagram of a Néel type domain wall. The rotation of magnetisation is in XY plane. The domain wall width direction is in Y axis.

bulk structures where xz plane' dimensions are similar or larger than W_{dw}. The unconstrained domain walls discussed above are all Bloch walls. Also a material with large exchange stiffness (A) would prefer to have a Bloch-type domain wall. Figure 2.6b shows the structure of a Néel-type domain wall. This type of domain wall appears when the cost on the anisotropy energy of magnetisation in xz plane exceed the exchange energy of rotations along xy plane. It usually exists in thin films where the anisotropy energy of the out of plane field is much larger than the in plane exchange energy.

As we mentioned above, magnetic domain walls in thin films are mostly Néel-type because the magnetisation prefers to follow a long geometrical direction which is in plane to reduce the shape anisotropy or demagnetisation. For example, in a piece of nickel thin film whose thickness is 20 nm and size 200×500 nm^2, the magnetisation will follow the 500 nm direction naturally. Furthermore there will be no domain wall in this system, because the nickel's unconstrained W_{dw}, 134 nm, is close to its dimensions. In this case we call this piece of thin film the single domain

system. When increasing the thin film to a large area such as 2×5 μm^2, there might be various of domain walls inside [31, 32]. The domain walls measurement methods such as magnetic force microscope (MFM) and Lorentz transmission electron microscope (Lorentz TEM) are useful for determining important magnetic parameters, such as spin lattice energy density constant K_a and exchange stiffness A.

The shape influences the stability of the domain wall. For instance in a long smooth magnetic thin film wire, a domain wall can be moved along the wire by an external force such as a current, magnetic field or polarised laser [33]. However, if there is a constriction structure along the wire such as a neck or bridge, the domain wall can be attracted and pinned [34, 35, 36].

2.4 Magnetoresistance

2.4.1 Introduction

Magnetoresistance is a change in resistance due to the application of an external magnetic field or magnetisation. It was firstly discovered in 1856 by William Thomson. The materials that he investigated show a resistivity which changes with the angle between external magnetic field and current direction. The resistivity is high when they are parallel whereas it is low when they are perpendicular to each other. This is caused by Lorentz force and known as ordinary magnetoresistance. Later he did the same experiment in Ni and found the same effect but greater in magnitude. Currently this is known as anisotropy magnetoresistance (AMR). In 1988, another important discovery in the magnetoresistance area, giant magnetoresistance (GMR) was firstly discovered by Grünberg's group. Almost at the same time in 1989, Fert's team reported a very large GMR effect [1]. This effect has been used in hard drive sensors leading to improved hard disk density in the following years. Around 1994, Moodera's research team at MIT demonstrated large tunnelling magnetoresistance (TMR) at room temperature based on a CoFe/Al_2O_3/Co stack structure [2], which was a huge improvement compared to the low temperature TMR discovered by Julliere in 1975 [37] or the room temperature TMR discovered by Terunobu Miyazaki in 1991 [38]. Again the hard disk storage density improved about 100 times with the TMR read head. After this milestone a significant number of researchers joined this field and various forms of magnetoresistance appeared during the following years, such as TMR with quantum effect, ballistic magnetoresistance (BMR), colossal magnetoresistance (CMR)

and domain wall magnetoresistance (DWMR). In the next sections we will discuss the major magnetoresistance effect in more detail.

2.4.2 Anisotropic magnetoresistance

Anisotropic magnetoresistance (AMR) is the variation of resistivity of ferromagnetic materials depending on the angle between the current and magnetisation direction. The ferromagnet conductor shows high resistivity when the magnetisation direction is parallel to the current, but low resistivity when antiparallel (Figure 2.7). The resistivity in the demagnetised state has a relation to the high

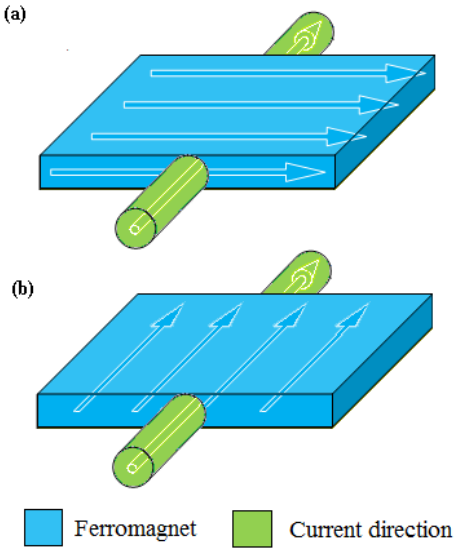

FIGURE 2.7: Schematic 3D diagram of the anisotropy magnetoresistance. (a) Low resistivity state. The magnetisation direction is perpendicular to the current (b) High resistivity state. The magnetisation is parallel to the current

and low resistivity shown as,

$$\rho_{av} = \frac{1}{3}\rho_{\parallel} + \frac{2}{3}\rho_{\perp} \tag{2.18}$$

where ρ_{av} is the demagnetised resistivity, $\rho_{\parallel}$ is the high resistivity and $\rho_{\perp}$ is the low resistivity. The average resistivity takes 1/3 contribution from the parallel state and 2/3 from the perpendicular state. The reason is that at demagnetised state magnetisation components are randomly distributed along three axis. Therefore one third of them follow the current orientation and two thirds are in the plane

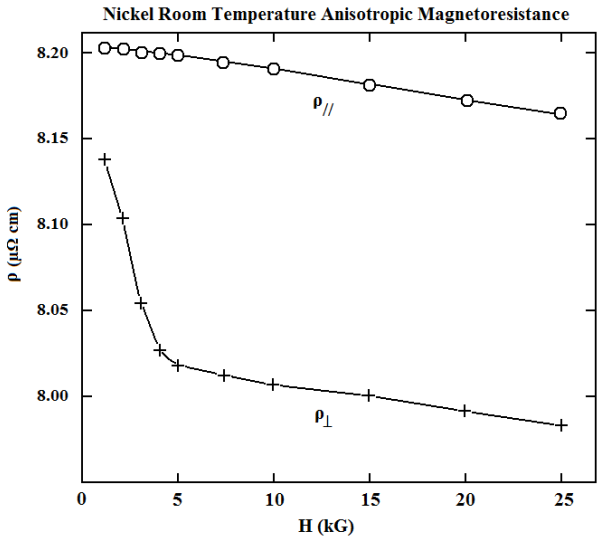

FIGURE 2.8: Plot of resistivity ($\mu\Omega$cm) as a function of external magnetic field (kG), reported by McGuire in 1975. The magnetic material was $Ni_{0.9942}Co_{0.0058}$ at room temperature. The circles on the curve $\rho_{\|}$ mark the resistivity when applied magnetic field is parallel to the current. The crosses on the curve $\rho_{\perp}$ mark the resistivity when applied magnetic field is perpendicular to the current. After Mcguire *et al* [39], copyright IEEE

perpendicular to the current. When the angle θ between the current and magnetisation is between 0° and 90° the AMR is given as,

$$\begin{aligned} \rho_{(\theta)} &= \rho_{\|}\cos^2\theta + \rho_{\perp}\sin^2\theta \\ &= \rho_{\perp} + \left(\rho_{\|} - \rho_{\perp}\right)\cos^2\theta \end{aligned} \tag{2.19}$$

It can be seen that the resistivity decreases when the angle between the current and magnetisation increases from 0° to 90°. The AMR ratio of a material is then given as,

$$r_a = \frac{\rho_{\|} - \rho_{\perp}}{\rho_{av}} \tag{2.20}$$

The AMR ratio is a percentage of the average resistivity change due to the AMR effect. It is independent of the magnetic field, and only relates to the material property. For instance, AMR ratio of Ni is around 2.5% according to McGuire's report in 1975 [39] (Figure 2.8). The measurement was based on ferromagnetic material $Ni_{0.9942}Co_{0.0058}$ at room temperature. There is a parallel AMR curve and a perpendicular AMR curve. It can be clearly seen that parallel resistivity is larger than the perpendicular resistivity. The parallel curve is almost flat whereas the

perpendicular decreases noticeably at the field 0 - 5 kG and becomes flat at higher field. In the parallel case the magnetisation of the nickel wire always follows its easy direction which is parallel to the current. However, in the perpendicular case, when the shape anisotropy exceeds the influence of Zeeman energy (0 - 5 kG), the magnetisation still follows the wire's easy direction. When the external magnetic field is larger than 5 kG, the cost on the Zeeman energy exceeded the shape anisotropy and the magnetisation follows the field direction. This process is indicated by the decrease of the perpendicular curve.

2.4.3 Giant magnetoresistance

The giant magnetoresistance (GMR) effect happens in a multi-layer structure in which magnetic and non-magnetic thin films are deposited alternately. There are two types of GMR effect; current in the film plane and current perpendicular to the film plane. Figure 2.9 shows the operation of the current in plane GMR device. When there is no external magnetic field, the magnetisation of all ferromagnetic layers are coupled to their neighbours oppositely due to the antiferromagnetic indirect exchange coupling or demag field. At this state, electron spins with both orientations are in low conductance spin channels due to the spin collision at the interfaces between ferromagnetic and non-magnetic layers. We call this the high resistance state (Figure 2.11b). When we apply an external magnetic field $\pm\mu_0 H_s$, all the ferromagnetic layers' magnetisation is saturated in the field direction. At this state, the electron spins with the orientation in the same direction as the external magnetic field do not have spin collisions at the interfaces, thus they are in a high conductance spin channel. We call this low resistance state (Figures 2.11(a)(c)). The field $\pm\mu_0 H_s$ is called the saturating field. Its value is determined by the coupling between the neighbour ferromagnetic layers which depends on the thickness of the non-magnetic layers. Figure 2.10 shows that the GMR curve of three types of devices whose non-magnetic layers are 1.8 nm, 1.2 nm and 0.9 nm thick. It can be seen that the GMR ratio increases when the thickness of the non-magnetic layers is reduced. Thinner non-magnetic layer gives larger GMR ratio, but requires larger saturation field H_s to switch. The magnetoresistance curve was measured at 4.2 K and the maximum magnetoresistance ratio was about 80% with respect to the low resistance state. Both H_s and magnetoresistance ratio decrease with the increase of temperature. H_s is reduced by about one third, while magnetoresistance ratio is reduced by a factor of 2. However it is still significant at room temperature.

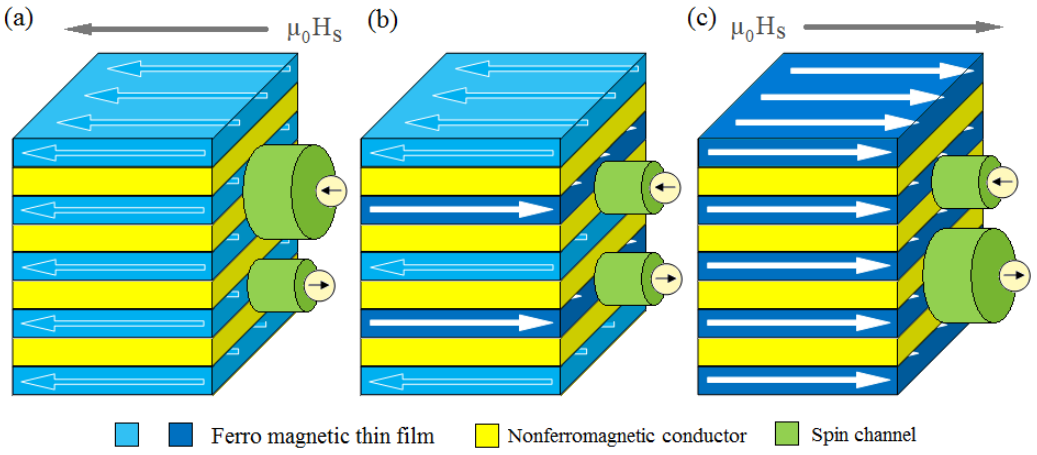

FIGURE 2.9: Schematic 3D diagram of a current in plane GMR structure. (a) magnetisation of all layers are saturated in left direction by an external magnetic field $-\mu_0 H_s$. Electrons whose spin orientation is the same as $\mu_0 H_s$ have a wide channel whereas the opposite orientation has a narrow channel. (b) magnetisation of all layers coupled oppositely by the exchange interaction between the neighbour layers. Electrons with both spin orientations have narrow channel. (c) magnetisation of all layers saturated at right direction by an external magnetic field $+\mu_0 H_s$. Electrons' channels are similar to the state shown in (a). (a) and (c) show low resistance states whereas (b) shows a high resistance state. The structure can be expressed by $[F_x N_y]_n$ where F is a type of ferromagnetic material, x is its thickness, N is a type of non-magnetic material, y is its thickness, n is number of the repeats of the $F + N$ layers.

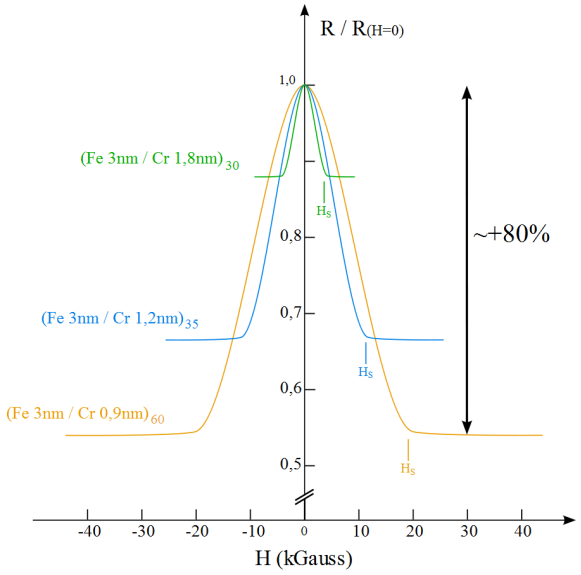

FIGURE 2.10: Magnetoresistance of three types of Fe/Cr stacks at 4.2K. The current and external magnetic field are along the same axis in the plane of the layers. After Baibich *et al* [1]

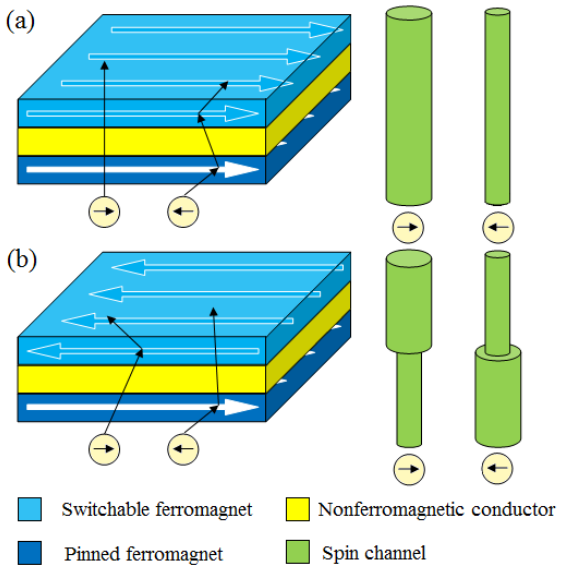

FIGURE 2.11: Schematic 3D diagram of the structure and operation of a current perpendicular to plane GMR spin-valve. (a) parallel state (b) antiparallel state. The parallel state has low resistance whereas antiparallel state has high resistance, because of the size of spin channel shown in the diagram

Another type of GMR is when the current is perpendicular to the film plane which is called GMR spin-valve (Figure 2.11). It normally contains three main layers. A pinned layer whose magnetisation does not change with the external field is normally pinned by an antiferromagnetic substrate, and a free layer works as a switch of the spin-valve. The magnetic materials could be Ni, Co and Fe. A non-magnetic conducting layer such as Cr, Cu, Ru or Ag [1, 40] separates the pinned and free layers. When the free layer is parallel to the pinned layer the electrons whose spins have the same orientation with the layers travel in a wide spin channel whereas the oppositely oriented electron spins have a narrow channel. When the two layers are antiparallel, electron spins in either orientation have a narrow channel in the layer with the opposite magnetisation. Therefore, the resistance of a parallel state is smaller than the antiparallel state.

Recent research announced that a graphene layer can be used as the separation layer for a GMR spin-valve [41]. However the spin-valve with a middle layer of graphene is more like a tunnelling magnetoresistance (to be introduced in the next section), because the graphene is not conductive in its perpendicular direction.

2.4.4 Tunnelling magnetoresistance

Tunnelling magnetoresistance (TMR) is similar to GMR but has a non-magnetic insulating layer instead of a conducting one. The insulating layer is normally 1 - 2 nm thick, such that the electrons can tunnel through. The materials of the insulating layer could be Al_2O_3 [2], Ga_2O_3 [42], MgO [43] and graphene [44].

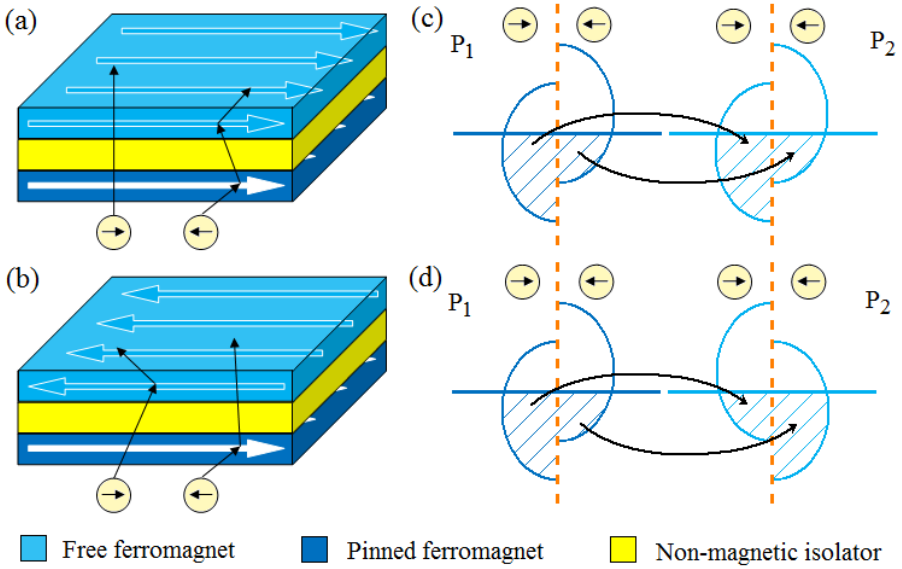

FIGURE 2.12: Schematic diagram of a TMR spin-valve at (a) parallel state and (b) antiparallel state. The spin polarisation of the pinned layer is P_1 and P_2 in the free layer. (c, d) show the spin transport in a tunnelling way. There is no spin flip during the tunnelling process.

Figure 2.12 shows the schematic diagrams of the tunnelling process of electrons with both up and down spins in (a) parallel state and (b) antiparallel state. Here we define spin-up as when the spin orientation is the same as the magnetisation of the pinned layer whereas spin down is the opposite. Figure 2.12(c, d) show the electrons' spin-up and spin-down energy band diagram and tunnelling processes respectively. The possibility of electron spins tunnelling through a TMR spin-valve is given in Table 2.3.

TABLE 2.3: Probabilities of electrons tunnelling through a TMR spin-valve

TMR state	Spin orientation	Probability of tunnelling
Parallel	$\rightarrow$	$(50\% + P_1/2)\,(50\% + P_2/2)$
	$\leftarrow$	$(50\% - P_1/2)\,(50\% - P_2/2)$
Antiparallel	$\rightarrow$	$(50\% + P_1/2)\,(50\% - P_2/2)$
	$\leftarrow$	$(50\% - P_1/2)\,(50\% + P_2/2)$

For example the first row shows in parallel state the spin-up electrons has the probability of $(50\% + P_1/2)(50\% + P_2/2)$ to tunnel through a TMR spin-valve. Thus the conductivity (σ) of the parallel and antiparallel states has a relation to the probability shown as,

$$\begin{aligned} \sigma_P &\propto (1 + p_1)(1 + P_2) + (1 - P_1)(1 - P_2) \\ \sigma_{AP} &\propto (1 + P_1)(1 - P_2) + (1 - P_1)(1 + P_2) \end{aligned} \tag{2.21}$$

where σ_P is the conductivity of the parallel state, σ_{AP} is the conductivity of the anti-parallel state. The magnetoresistance ratio can be given with respect to the high or low resistance state,

$$r_{TMR} = \frac{R_{AP} - R_P}{R_P} = \frac{\Delta\sigma}{\sigma_{AP}} = \frac{2P_1P_2}{1 - P_1P_2} \tag{2.22}$$

where r_{TMR} is the TMR ratio, R_{AP} is the electric resistance of a TMR device in anti-parallel state, R_P is the electric resistance of a TMR device in parallel state ,$\Delta\sigma = \sigma_P - \sigma_{AP}$ is the conductance change between parallel and antiparallel state, P_1 and P_2 are spin polarisations in the pinned and free layers respectively.

However the magnetoresistance ratio in the TMR effect is not a constant property. In the experiment the TMR ratio decreases with the increase of supply voltage (Figure 2.13). The decrease was almost linear so the TMR effect is more likely to have a constant bias change than a constant resistant ratio. The result also shows the annealing process helps to increase the TMR ratio, because it increases the quality of the interface.

2.4.5 Quantum tunnelling magnetoresistance

The quantum tunnelling magnetoresistance (QTMR) is a combination of a quantum dot single electron transistor and a TMR spin-valve [45]. The structure of QTMR is similar to TMR, but a quantum dot is used instead of a tunnelling film. In this structure the tunnelling becomes much more complex, because a spin-flip is possible inside the quantum dot. To explain this effect we have to explain firstly what is Coulomb blockade of a quantum dot single electron transistor.

The coulomb blockade requires that the dot charging energy is larger than the thermal energy in order to avoid tunnelling current generated by thermal excitation (Equation 2.24). The coulomb blockade also requires the resistance between the pads and dot to be larger than the quantum resistance to prevent classical

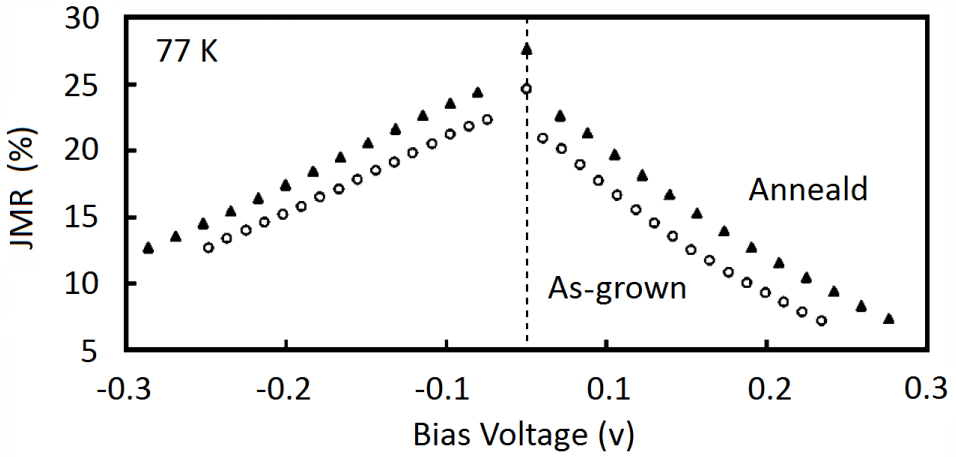

FIGURE 2.13: Bias dependence of TMR for a $Co/Ga_2O_3/Ni_{80}Fe_{20}$ junction with 1.4 nm thick Ga_2O_3 layer at a temperature of 77 K. The empty circle was from a device as-grown whereas the solid triangle was from a device after 1 hour vacuum annealing at 140 °C. In both devices the TMR ratio decreases when the absolute value of the bias increases. After Li *et al* [42], copyright AIP

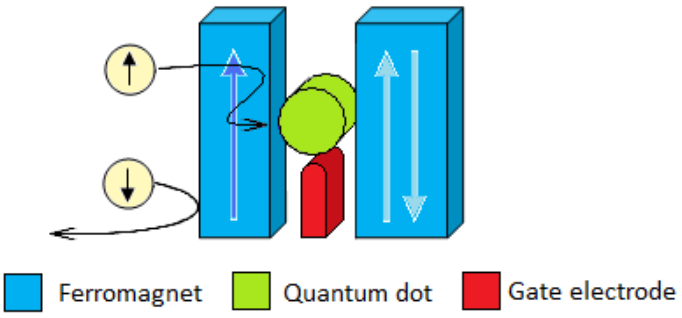

FIGURE 2.14: Schematic diagram of a quantum tunnelling magnetoresistance spin-valve with a side gate. The left hand side is a pinned pad, the middle is a quantum dot, the right hand side is a free pad, underneath is a side gate. The electrons with spin-up and spin-down show the transport when spin polarisation is 100%

current (Equation 2.25). The quantum resistance, $R_0 \approx 12906.4\Omega$ comes from the quantum conductance, $G_0 \approx 7.74809 \times 10^{-5}\Omega^{-1}$. In a ballistic transport system such as a conductive point contact, the conductance has to be an integer multiple of G_0, shown as,

$$G_0 = 2e^2/h \tag{2.23}$$

where e is the charge of an electron and h is Plank constant. It is not necessary that all types of conductance have to be an integer multiple of G_0, but only the

ballistic channels. When the resistance is larger than the quantum resistance there is no classical current, but only tunnelling current through the blockade. This requirement is mathematically described as,

$$E_c = \frac{e^2}{C_t} > E_t = k_B T \tag{2.24}$$

where e is the charge of an electron, C_t is the total capacitance of the quantum dot, E_c is the charging energy, E_t is the electron thermal energy, k_B is the Boltzmann constant, T is the temperature. The ballistic resistance is required to be larger than the quantum resistance,

$$R_b > R_0 \approx 12906.4\Omega \tag{2.25}$$

When the system meets the requirement of a coulomb blockade, the number of electrons inside the quantum dot can be tuned by the gate voltage by controlling the energy state of the dot shown as,

$$V_g \quad = n\frac{e}{C_t}, |V_{ds}| < V_{CB} \quad = \frac{e}{2C_d} \tag{2.26}$$

where V_g is the gate bias, n is the number of electrons inside the quantum dot, e is the charge of an electron, C_t is the total capacitance of the dot $C_t = C_l + C_r + C_{gd} + C_d$, C_l and C_r are the dot to left pad and dot to right pad capacitance respectively, C_{gd} is the gate to dot capacitance, C_d is the self-capacitance of the dot, V_{ds} is the drain source voltage, V_{CB} is called coulomb blockade voltage.

When $\pm V_g$ is at points where $n = 0, 1, 2, 3...$, the energy of the dot is at a stable state, therefore there is no current tunnelling through the blockade when $V_{ds} < V_{CB}$. However when $\pm V_g$ is at points where $n = \frac{1}{2}, 1\frac{1}{2}, 2\frac{1}{2}, 3\frac{1}{2}...$ the energy of the dot is at a unstable state, and the number of electrons inside the dot starts oscillating between two integers, therefore the current is tunnelling through the blockade from high bias to low. In a QTMR spin-valve the transport principle is similar to a coulomb blockade. When $n = \frac{1}{2}, 1\frac{1}{2}, 2\frac{1}{2}, 3\frac{1}{2}...$ there is a tunnelling current. Moreover, when the ferromagnetic pads behave like in a TMR spin-valve, the QTMR spin-valve shows low resistance at paralle state whereas it shows high resistance at anti-parallel state. The difference is that in the QTMR device there might be a spin-flip inside the quantum dot. It was reported by Weymann *et al* in 2005 [46] that only when the dot is empty or doubly occupied the transport is carried by non-spin-flip tunnelling whose MR is the same as TMR. Otherwise, the QTMR is reduced below the TMR value, due to electrons losing spin information

inside the quantum dot. Furthermore, the quantum dot may be partly magnetised due to the asymmetry of the pads, this gives another spin polarisation rate P_d (P_d <min(P_1, P_2)). The tunnelling process becomes from P_1 to P_d and from P_d to P_2. If we put the worst case $P_d = 0$ in to Equation 2.22, the QTMR ratio is zero.

2.4.6 Ballistic magnetoresistance

Ballistic magnetoresistance (BMR) is another type of magnetoresistance different from GMR and TMR. It happens when electron travel from one magnetic domain to another adiabatically. For the TMR the electrons tunnel through an insulator barrier by quantum effect, but for the BMR the electrons travel through an atomic contact [13] or carbon nanotube (CNT) [47, 48] without scattering but still in a classical way (Figure 2.15). The conductance of an ballistic transport is [25],

$$G = \frac{2e^2}{h} \sum_{i=0}^{n} T_i \tag{2.27}$$

where e is the charge of an electron, h is the Planck constant, T_i is the probability of transport in channel i. For a ballistic channel $T_i = 1$. G has to be an integer multiple of the quantum conductance G_0 [49] (Equation 2.23).

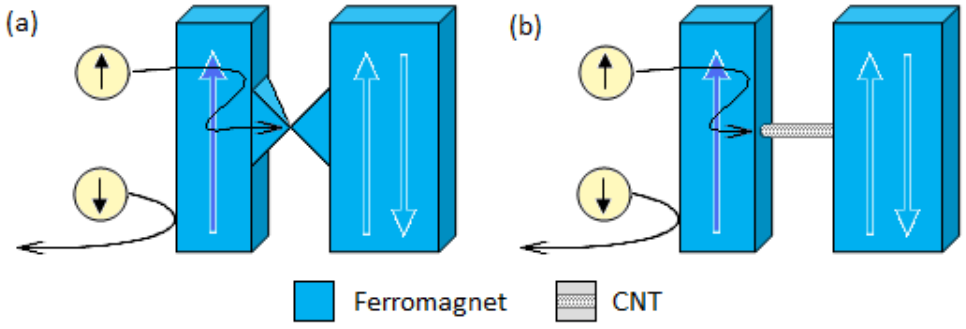

FIGURE 2.15: Schematic diagram of a BMR spin-valve with (a) an atomic contact and (b) a carbon nanotube.

Figure 2.16 shows a carbon nanotube BMR spin-valve and its magnetoresistance curve reported by Tsukagoshi *et al* in 1999 [47]. A distinct step-like spin-valve behaviour is shown from the measurement results from three different devices. Due to non-perfect contact between CNT and Co, the measurement did not show

the quantum conductance. From these results we cannot determine whether spin-flip exists when electrons travel through the long channel.

There is another type of ballistic which is similar to AMR. When the ballistic current is parallel to the magnetisation it is in low conductivity state, whereas perpendicular shows high conductivity. Figure 2.17 shows an example of such a device (a,b) and its magnetoresistance curve (c,d) reported by Sokolov *et al* in 2007 [13]. From the step like curve it can be seen that a distinct quantum conductance was recorded in a reproducible step-like magnetoresistance curve. The conductance has a step value of e^2/h which is half of the quantum conductance ($2e^2/h$). The reason is that one of its channel is spin dependnt, either up or down state spins are able to travel through the channel. It can be seen from Figure 2.17 (d), when the angle between external field and current θ is between 70 ° and 140 ° the conductance increase by 1 spin quantum conductance. And this behaviour is distinctively different from AMR.

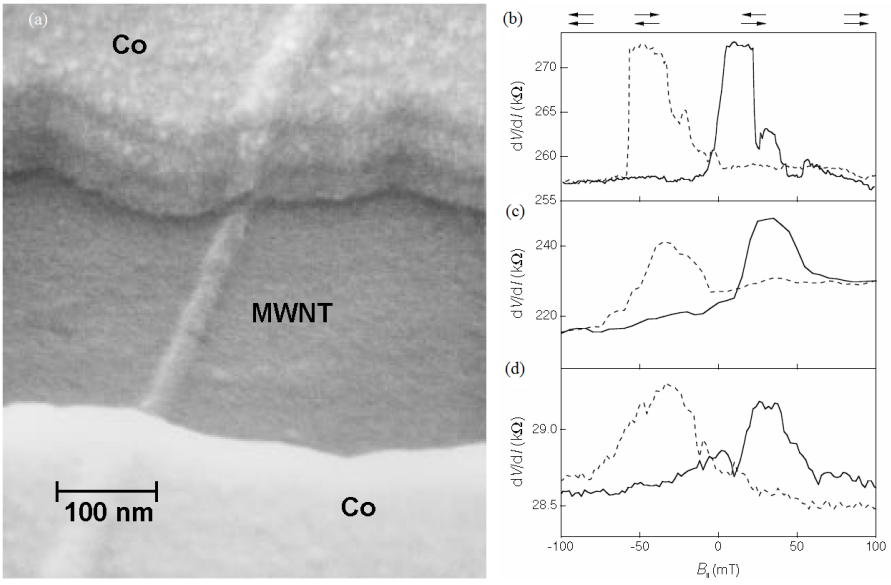

FIGURE 2.16: (a) SEM micrograph of a multi-walls carbon nanotube (MWNT) spin-valve. (b, c, d) Plots of magnetoresistance against of external magnetic field of three different MWNT spin-valves. The resistance difference is due to the contact between Co and CNT. The $\Delta R/R$ is approximately 6% in (b), 9% in (c) and 2% in (d). After Tsukagoshi *et al* [47], copyright Nature

2.4.7 Colossal magnetoresistance

The colossal magnetoresistance (CMR) is similar to the TMR effect when the spin polarisation P approaches 100%. If we put $P_1 = P_2 = 100\%$ into Equation 2.22,

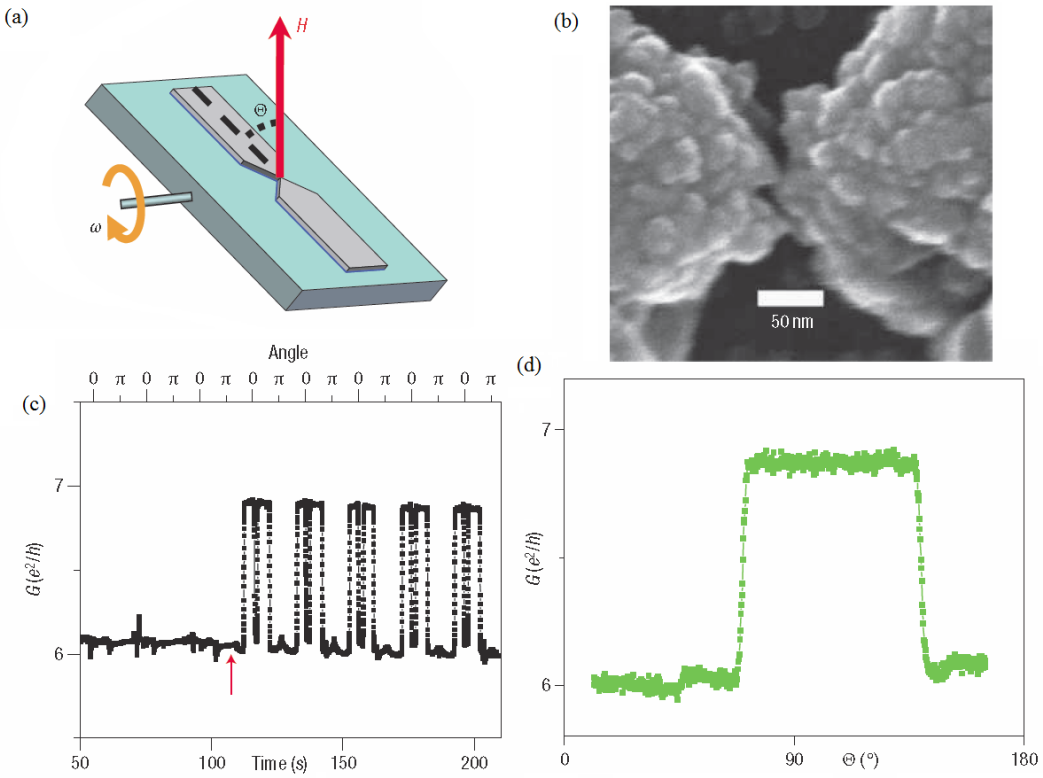

FIGURE 2.17: (a) Schematic diagram of a BMR spin-valve and its operational method (b) High-magnification micrograph of a Co atomic contact (c) Plot of conductance against time of a device shown in (a) rotated with angular frequency, $\omega = 2\pi/T$ ($T = 20$ s) in the saturation magnetic field at room temperature. The magnetic field was turned on at an instant indicated by the red up arrow, after which a periodic magnetoresistance with one quantum conductance was recorded. (d) Half a cycle, 0 - 180° magnetoresistance curve of what is shown in (c). After Sokolov *et al* [13], copyright Nature

the TMR ratio can be ∞. The CMR exists in a type of materials which change between metallic and semiconductor in the pure spin current (to be explained in the following section) by switching its magnetisation direction [50, 51]. The popular materials are $LaSrMnO_3$ and $LaCaMnO_3$, in which Mn^{4+} ions have only t_{2_g}-state electrons, whereas Mn^{3+} ions have one electron in e_g state (Figure 2.18). Because of the Hund's rule coupling, the e_g and t_{2_g} electrons prefer the same spin orientation. Thus only spin-up electrons exist in the e_g state, and all the conducting electrons in the material are polarised to its magnetisation direction. This is known as the half metallic characteristic, because for spin-up electrons the conductivity is high (similar to metal), whereas for spin-down electrons the conductivity is low (similar to semiconductor). With this behaviour the CMR can be as high as 72,000% at 4.2K [52]. At room temperature, the CMR ratio can still be considerablly larger than 50% [53]. The spin mobility of both metal and

semiconductor states can be tuned by the contents of Mn^{4+} and Mn^{3+} [54].

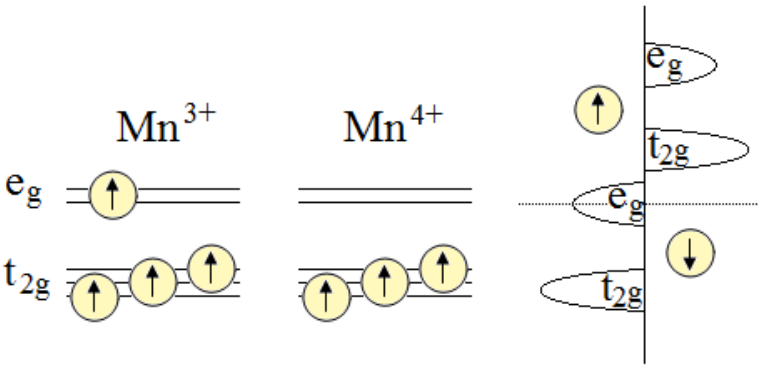

FIGURE 2.18: Schematic diagram of the electron energy states of Mn^{3+} and Mn^{4+} ions. Half metallic property is shown in the energy band diagram

2.5 Spin current and spin torque

Spin current is a type of spin-depended transport. In nano structures this phenomenon is of great interest because of the potential to build spin based logical devices, such as spin based transistors and memory cells. Research in this area indicates that the spin polarised carriers can be injected into non-magnetic metal materials or semiconductors. This was firstly reported by Johnson and Silsbee in 1985 [55]. However, a recent article by Zhang *et al* (2011) announced a pure spin current was generated in a graphene without a magnetic injector [56].

Figure 2.19 shows a simple spin injecting and detecting structure. The polarised spins are injected from the spin injector and driven to the end of a non-magnetic wire by a driven current. On the other side of the non-magnetic material the charge current is zero, but the spin up and spin down currents diffuse equally in opposite directions. A detector with a distance L from the injector can detect the spin accumulation by a voltage signal. The value of the voltage is positive when magnetisation of the detector is parallel to the injector, and negative when antiparallel. The absolute value of the voltage decreases when L increases.

The spin polarisation rate, P is defined as,

$$P = \frac{n_\uparrow - n_\downarrow}{n_\uparrow + n_\downarrow} \tag{2.28}$$

where $n_\uparrow$ is the spin-up carrier density, $n_\downarrow$ is the spin-down carrier density. P is

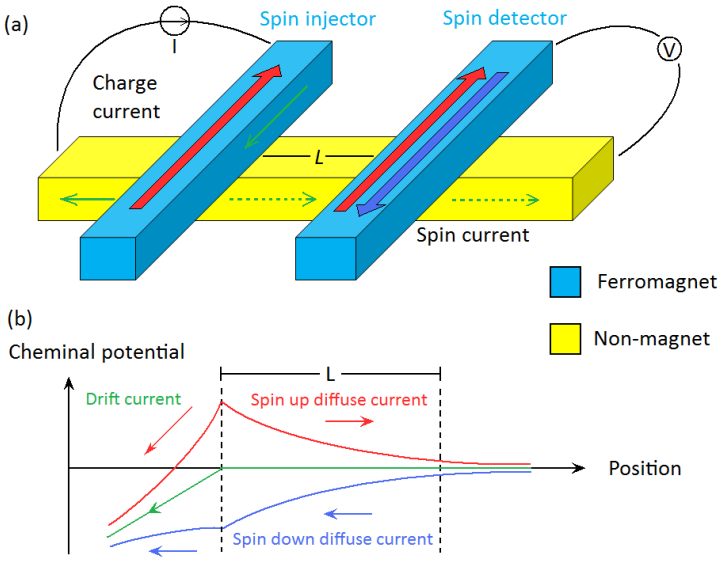

FIGURE 2.19: (a) Schematic 3D diagram of a spin current generating structure. A constant current is driven from a spin injector to one end of a non-magnetic material. At the detector side, a voltage between a spin detector and the other end of the non-magnetic material can be detected. (b) Schematic plot of the potential - position curve. The left and right dashed lines indicate the position of the spin injector and detector respectively. The green curve (middle) shows the potential of the classical current. The red curve (upper) shows the potential of the spin up current, whereas the blue (bottom) curve shows the spin down's.

proportional to the voltage signal of detector. P decays exponentially with length,

$$P = P_0 e^{-\frac{L}{\lambda}} \tag{2.29}$$

where P_0 is the spin polarisation rate of the injector, L is the distance between injector and detector and λ is the spin diffusion length. The value of λ depends on the type of material, crystal structure, purity of a material and temperature [57]. There are several ways to increase the value of P_0. For example a thin tunnelling barrier such as MgO [58], similar to what is used in TMR, could help to reduce the interface spin polarisation loss.

Figure 2.20 shows the difference between a diffuse spin current and a drift spin current. The diffuse spin current has negative magnetoresistance effect whereas the drift spin current has positive magnetoresistance. In a diffuse spin current, the amounts of spin-up and spin-down electrons are similar (unpolarised), but the carriers flow in opposite direction. In the drift spin current, the spin-up and spin-down electrons flow in the same direction, but the quantity of each is not equal (polarised). In a pure spin current all the conducting electrons are polarised in one

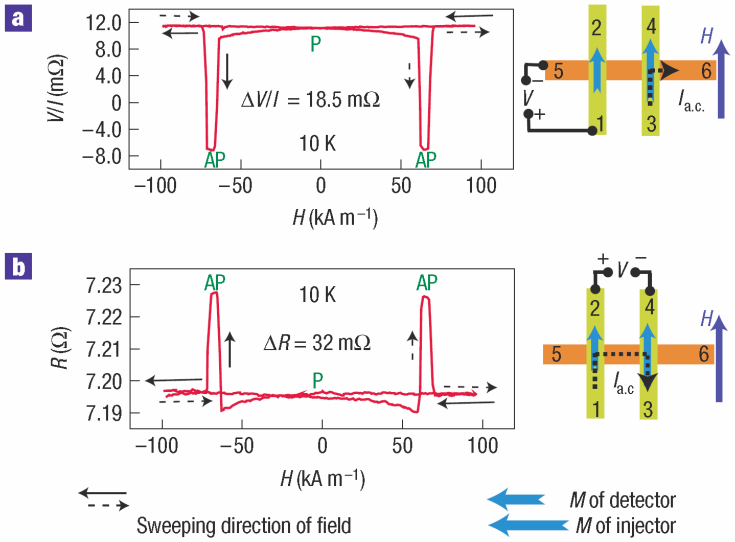

FIGURE 2.20: (a) Non-local diffuse spin current signal as a function of magnetic field. (b) Local-spin drift spin current signal as a function of of magnetic field. The measurement geometry schematic diagrams are drawn beside each plot. After Yang *et al* [59], copyright Nature

orientation. The local and non-local measurements are shown in the schematic diagrams in Figure 2.20. Most magnetoresistance effects we have discussed are local spin-valves, such as GMR and TMR. The domain wall magnetoresistance which we are discussing below is also based on local measurement.

The spin transfer torque is the interaction between spin polarised current and the magnetisation in both spin-valves and spin current devices. Magnetoresistance can be considered as a spin transfer torque interaction of the conducting electron spins caused by the ferromagnet. However if the spin polarised current is large enough the magnetisation orientation of the ferromagnet can be changed due to the spin transfer torque influence. For example, a domain wall can be pushed by the current through a head to head domain wall structure as reported by Lepadatu and Xu in 2004 [60] (Figure 2.21). The measurement started from the antiparallel state with a domain wall in the constriction. As the current increased, it is able to switch the magnetisation on the other side of the domain wall. Thus in the plot the resistance decreases at the minimum current required to switch the other side of the domain wall.

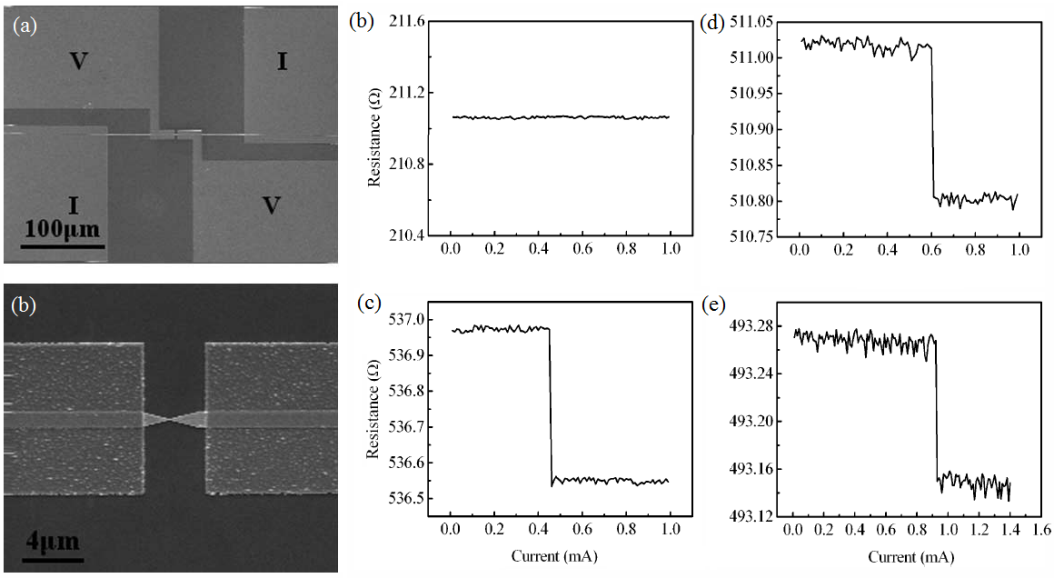

FIGURE 2.21: (a) SEM micrograph of a head to head domain wall spin-valve with measurement setup. (b) SEM micrograph of (a) zoomed in. (c, d, e, f) Plot of resistance to applied current of the device with a constriction width of (a) no constriction (b) 100 nm (c) 200 nm (d) 300 nm. After Lepadatu and Xu [61], copyright IEEE

2.6 Domain wall magnetoresistance

Domain wall magnetoresistance (DWMR) is the difference in resistance of a single ferromagnetic material with and without a domain wall. It can be used to make spin logic circuits [62]. To operate a DWMR spin valve, the magnetisation of the domains can either be switched by an external magnetic field or even a spin current. Spin current induced domain wall movement could help the DWMR effect being established in industry, for it is capable of complete solid state magnetic based storage devices [35].

In 1999, Bruno [19] proposed that in nano-structured devices the domain wall width can be constricted by geometric means. A sudden large expansion of the magnetic area will constrict the domain wall as the cost of increasing the area of the domain wall outweighs the exchange interaction. DWMR occurs when electrons travel from one side of the magnetic domain wall to another non-adiabatically. It is reported in many different structures (Table 2.4). In line-shaped devices, the magneto-resistance effect of the domain wall is relatively small because the classical resistance of the line hides the DWMR effect. In the point connecting structure the magnetoresistance can be very large due to the ballistic transport of the electrons, but the fabrication procedures such as mechanical break junc-

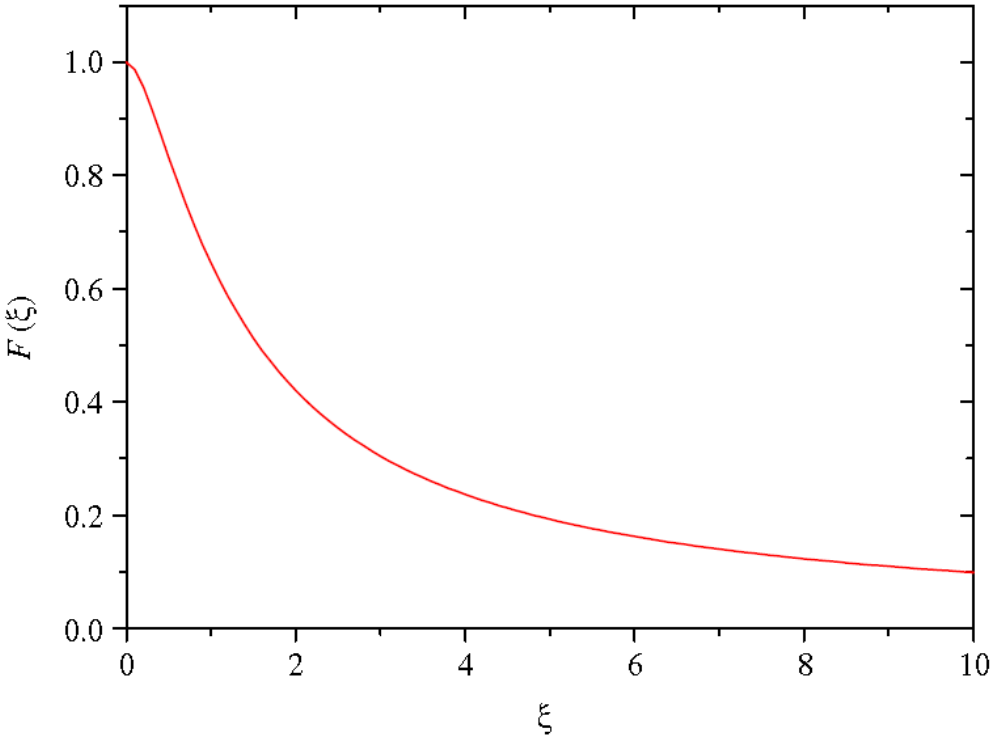

FIGURE 2.22: Plot of $F(\xi)$ as a function of $\xi = w/\lambda_F$ where w is the domain wall width and λ_F is the spin diffusion length. After Ieda *et al* [21], copyright MMM

tions [22],electrical break junctions [23] and electrochemical junctions [24] are not suitable for industrial applications [25], and the measurements are subject to artefacts [26]. An overview is given in Table 2.4.

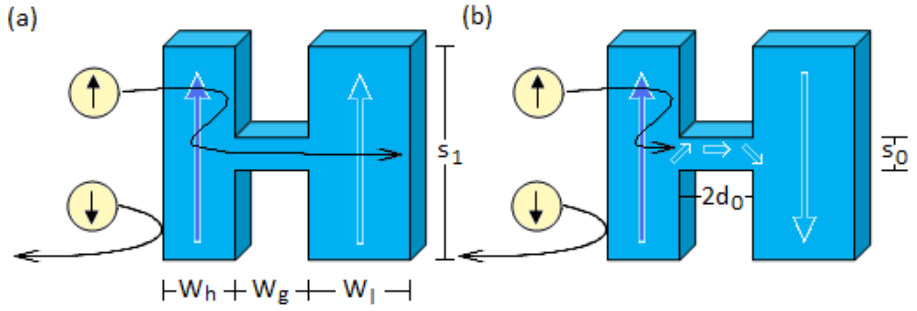

FIGURE 2.23: Schematic diagram of a domain wall magnetoresistance spin-valve at (a) parallel and (b) antiparallel state. The spin transport shows an ideal situation when in a material with a spin polarisation rate 100%, which could result very large DWMR

The DWMR phenomenon could be explained by the collision between the carrier spins and the domain wall. Morosov and Sigov in 2004 [20] reported a multilayer

TABLE 2.4: Overview of research work on domain wall magnetoresistance

Structure	Researcher	year	Found
Line	Lepadatu *et al* [36]	2010	Spin current domain wall pinning
	Haug *et al* [8]	2009	Domain switching process
			DWMR ratio 0.06%
	Bogart *et al* [9]	2009	DWMR wire width & thickness
	Ebels *et al* [12]	2000	DWMR in a straight wire
			DWMR ratio 8Ω/1390Ω at 77K
Head to head domains	Arnal *et al* [10]	2007	Ion beam etched DWMR structure
			MR ratio 0.5kΩ/41kΩ
	Lepadatu *et al* [60]	2004	RM ratio 0.13%
	Ruster *et al* [11]	2003	Further etching the wire DWMR structure
			DWMR ratio 2000% at 4.2 K
	Miyake *et al* [63]	2002	MR ratio 0.8Ω/581Ω at 50K
Ring	Chen *et al* [5]	2007	Magnetic tunnel ring junction
			8% MR ratio
	Klaui *et al* [4]	2003	34nm bottle neck in a ring
			MR ratio 0.5 Ω/118Ω
	Lai *et al* [6]	2003	MR ratio 0.05Ω/47.1Ω
	Yu *et al* [64]	2003	8 half rings in series
			MR ratio 0.3% at 10K
Zigzag Cross	Gao *et al* [65]	2004	MR ratio 0.05% at 300K
	Tsai *et al* [15]	2002	0.1% at 250K
	Xu *et al* [16]	2000	45° domain wall
			MR ratio 0.04Ω/136.26Ω
Bridge	Hickey *et al* [66]	2008	bridge size 200nm×200nm
			0.06% DWMR
	Ruotolo *et al* [17]	2007	bridge size 3μm×500nm
			MR ratio 0.6% at 4.2K
	Claudio-Gonazalez *et al* [18]	2010	bridge size 60nm×41nm
			estimated MR 1.53Ω
Atomic contact	Sokolov *et al* [13]	2007	MR ratio 1/7 e^2/h(quantum conductance)
	Montero *et al* [14]	2004	MR ratio 2Ω/1050Ω
pinhole	Prieto *et al* [67]	2003	DWMR 0.1Ω at 77K

Bloch wall electron scattering model shown as,

$$\frac{\Delta\sigma}{\sigma_0} \approx \frac{4\pi^2 E_f \tau}{h(k_F b)(k_F L)} e^{-\pi q_0 L} \tag{2.30}$$

where σ is the conductivity, E_f is the electron Fermi energy, τ is the electron mean free time across a Bloch wall, h is the Planck constant, k_F is the electron wave vector component, b is the mean domain thickness, L is the Bloch wall thickness, $q_0 = k^F_{max} - k^F_{min}$, k^F_{max}, k^F_{min} are the Fermi wave vectors of sub-bands. For example, with $E_f = 3$ eV, $\tau = 10^{-3}$ s, $k_F = 1$ Å^{-1}, $b = 100$ Å, $L = 20$ Å and $q_0 = 0.1$ Å^{-1},

one finds $\Delta\sigma/\sigma_0 = 0.02$ [20]. The DWMR phenomenon can also be explained by a spin accumulation model as reported by Ieda *et al* [21], and described by,

$$\Delta R = 2P^2\rho_0\lambda_F A^{-1} F(\xi) \tag{2.31}$$

where P is the polarisation of the conduction spin, ρ_0 is the classical resistivity, λ_F is the spin diffusion length, A is the cross sectional area of the constriction, and $F(\xi)$ is a function of the ratio w/λ_F in which w is the domain wall width. Reduction of the domain wall width will increase $F(\xi)$'s value [21] (Figure 2.22).

In this report we are going to introduce the fabrication and magnetoresistance measurement results of an H-shaped spin-valve in nanometer size. Especially we are going to discuss the physics of the domain wall magnetoresistance when the domain wall width is constricted down to sub-50 nm region. Figure 2.23 shows the schematic diagram of the H-shaped spin-valve in both the parallel and antiparallel state. Similar to TMR and GMR, the resistance is low in the parallel state and high in the antiparallel state. The magnetoresistance ratio is largely influenced by the material's spin polarisation. The electron spins transport in Figure 2.23 relates to the ideal case when $P = 100\%$. The geometrical parameters of our DWMR spin-valve include the width of the high coercive side, W_h, the width of the low coercive side W_l, the length of the bridge $2d_0$, the gap width W_g ($W_g = 2d_0$), the width of the bridge s_0 and the height of the domain s_1. The operation of the H-shaped spin valve is controlled by W_h and W_l, whose value determines the switching point of each domain in a sweeping external manetic field.

Fangohr *et al* have previously shown using a micro-magnetic simulation that the domain wall width can be reduced by scaling the geometrical size of the bridge either through a reduction of the s_0/s_1 ratio or through limiting the bridge length $2d_0$ [30]. Using the s_0/s_1 ratio of 0.05, 0.10 and 0.15, we can calculate the value of the domain wall width once demagnetisation effects are taken into account (Figure 2.24). This calculation is based on Bruno's domain wall width model (Equation 2.12). If we put the $s_0/s_1 = 0.10$ results of the w_{dw} into Equation 2.31, together with a spin polarisation of $P = 20\%$, $\lambda_F = 21$ nm and $\rho_0 = 520$ nΩm [18] we arrive at a value of $\Delta R/R$ as a function of $2d_0$ (Figure 2.25). It can be seen that the DWMR ratio is expected to increase significantly when the bridge length is shorter than 20 nm.

A similar structure was reported by Hickey *et al* in 2008 [66] (Figure 2.26). The magnetoresistance ratio was reported to be between 0.04% and 0.08%. Their MOKE measurement magnetic hysteresis curve indicates that the antiparallel state

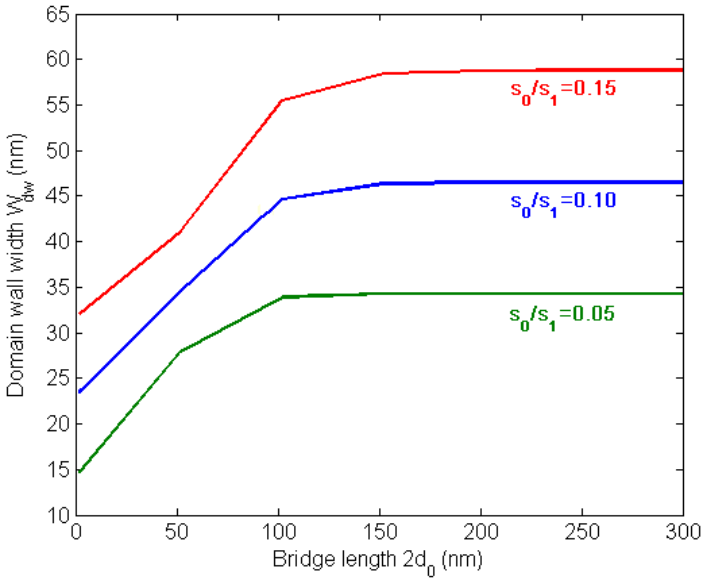

FIGURE 2.24: Plot of domain wall width as a function of bridge length of an H-shaped spin-valve. s_0 is the width of the bridge and s_1 is the height of the domain.

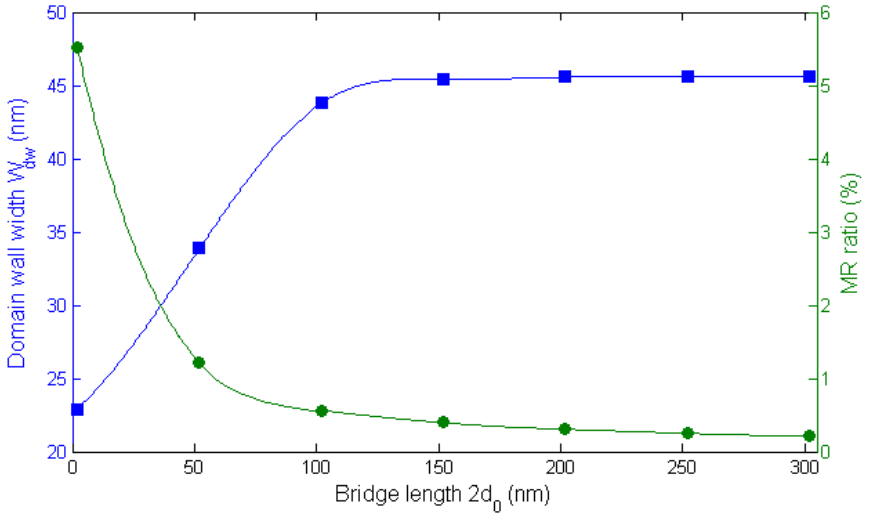

FIGURE 2.25: Plot of the domain wall width w_{dw} (left hand side curve blue) domain wall magnetoresistance ratio $\Delta R/R$ (right hand side curve green) as a function of bridge length $2d_0$ of an H-shaped spin-valve with $s_0/s_1 = 0.10$.

in the tank structure (Figure 2.26b) is more distinct than the rectangular one (Figure 2.26a). The tank's magnetoresistance curve has better step-like shape, because its shape anisotropy is larger. The domain wall of their H-shaped device was not constricted, for the geometrical size is much larger than the constrained region. And inside those domains there are multiple number of domain walls because of its big size and non-perfect thin film.

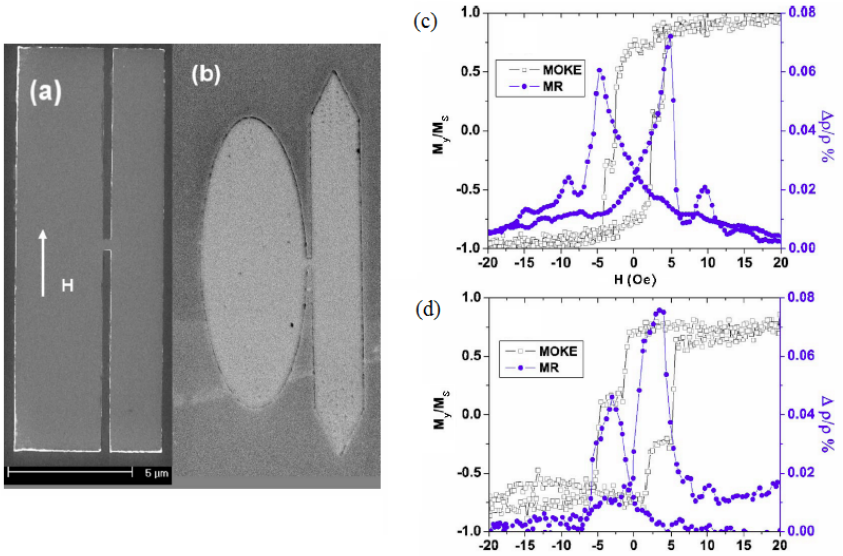

FIGURE 2.26: SEM micrographs of the (a) rectangular and (b)tank shaped H-shaped structure. (c, d) Plots of M_y/M_s (left hand side black empty squares) and $\Delta\rho/\rho$ (%) (right hand side blue solid dots) as the function of applied external magnetic field (Oe) of (a, c) respectively. After Hickey *et al* [66], copyright AIP

Another type of DWMR could be a pin-hole spin-valve between two magnetic pads (Figure 2.27). The behaviour of the pin-hole spin-valve is similar to a current perpendicular to plane GMR or TMR, for is has parallel and antiparallel states showing low and high resistance, respectively. The pin-hole spin-valve's domain wall width W_{dw} is determined by the height of the pin-hole h which can be controlled by the separation layer's thickness. The diameter of the pin-hole d is limited by the resolution of the e-beam lithography. The domain wall of a pin-hole spin-valve is determined by the value of d/h [68]. It is Bloch type if $d/h \geq 1.35$ whereas it is Néel type if $d/h \leq 1.35$. The advantage of the pin-hole spin-valve is that w_{dw} can be constricted down to sub-20 nm region, therefore it may have large magnetoresistance ratio. The drawback is that the capacitance between two pads could be significant which increases the RC time and reduces its operating speed. Especially when h is scaled down to sub-10 nm the exchange coupling between two domains and tunnelling current may also cause problems.

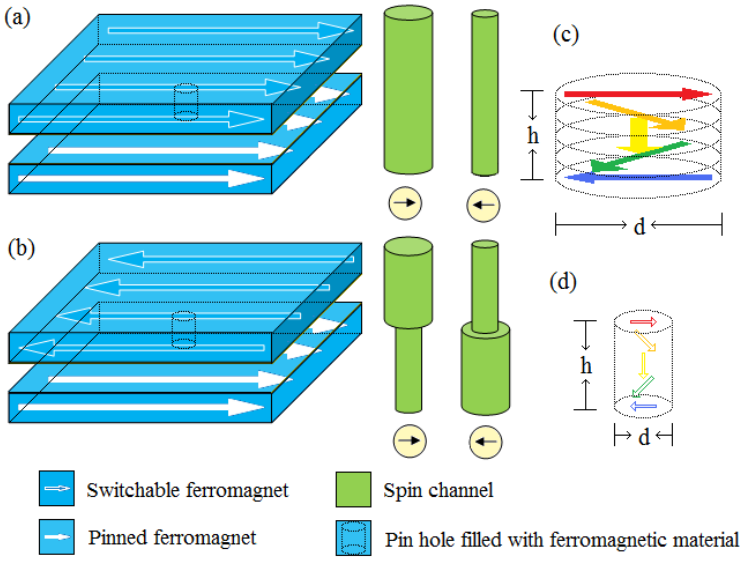

FIGURE 2.27: (a, b) Schematic diagram of a pin hole DWMR spin-valve at (a) parallel and (b) antiparallel states. (c, d) Schematic diagram of a (c) Bloch type domain wall inside a pin hole whose $d/h \geq 1.35$ and (d) Néel type domain wall $d/h \leq 1.35$. d is the diameter and h is the height of the pin hole.

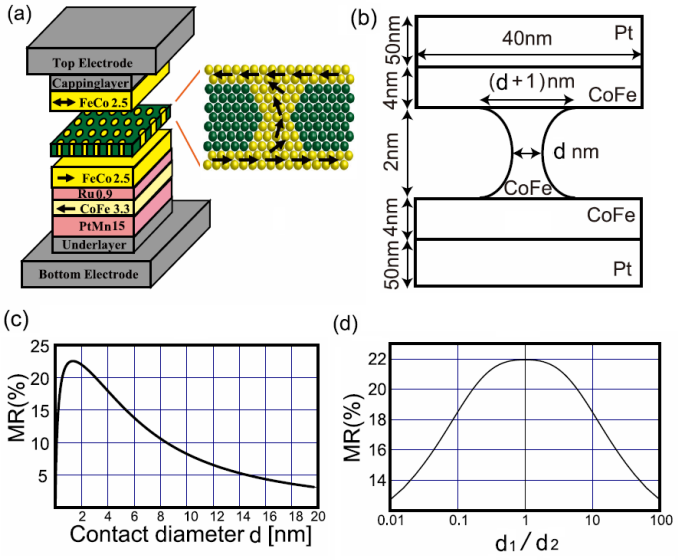

FIGURE 2.28: (a) 3D schematic diagram of a multi-pin-hole spin-valve structure and the domain wall inside a pin-hole. (b) schematic diagram of a pin-hole cross section. (c) plot of magnetoresistance ratio as a function of the pin-hole diameter, r. (d) plot of magnetoresistance ratio as a function of the neighbour's d_1/d_2 ratio. After Sato *et al* [69], copyright IEEE

Figure 2.28 shows the theoretically expected magnetoresistance ratio from a multi-pin-hole spin-valve structure reported by Sato *et al* in 2010 [69]. Figure 2.28(a) shows a possible structure of a pin-hole spin-valve. Figure 2.28(b) shows the material and geometrical parameters of the pin-hole spin-valve for simulation. Figure 2.28(c) shows that the magnetoresistance increases when d decreases, but reaches a peak at about 1 nm and decreases suddenly when d is below 1 nm. Figure 2.28(d) indicates that the size variations of the diameter of the pin-holes reduces the magnetoresistance ratio.

Chapter 3

Development of e-beam and helium ion beam writing

3.1 Device layout

Nano fabrication is one of the most important technologies in both research and industry. Applications such as computing, communication, health care, energy and material science are benefiting from nano fabrication technologies. In this field the control of size and shape is critically important, because smaller features could result in larger density, lower power consumption, better portability and multi-functionality. The size control can be achieved by patterning method also known as top down approach and self-assembling bottom up process. The nano fabrication we use is top down and is mainly cleanroom technologies such as lithography, metallisation, etching, lift-off, ion beam milling etc. In this chapter full fabrication procedures of the H-shaped domain wall magnetoresistance (DWMR) spin-valve are introduced, including structure design, lithography, metalisation, lift-off and helium ion beam milling. The purpose is to fabricate measurable DWMR devices where the domain wall constriction width is as narrow as possible.

Figure 3.1 shows a schematic diagram of the cross section view of the device structure. The substrate is a $< 100 >$ P-type 6" silicon wafer with 100 nm SiO_2 thermally grown on the front side. The first and second Au layer is patterned by photolithography as such large areas would lead to too long exposure time in e-beam lithography. The third and fourth Au layers are patterned by e-beam lithography to achieve a high alignment accuracy to the magnetic layer and further reduces the layer thickness from 20 nm to 12 nm. The device is fabricated as

the fifth (last) layer to avoid damage caused by further processing. A number of fabrication ideas have been processed to achieve this final structure. For simplicity we do not introduce all intermediate structures. The reason why a 5-layered structure is necessary will be explained below.

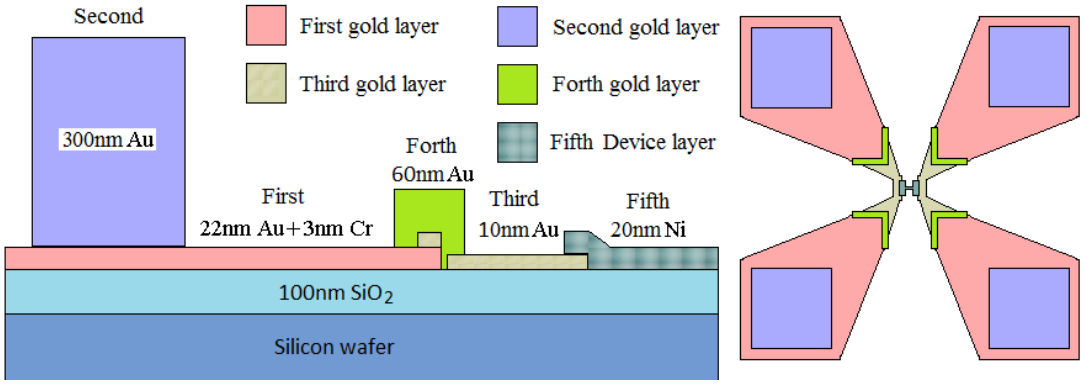

FIGURE 3.1: Schematic diagram of the cross section view of the fabrication processes. The first and second layers are fabricated by photolithography and metal lift-off. The subsequent layers are patterned by E-beam lithography.

The first Au layer is patterned by photolithography instead of e-beam lithography, because this reduces the e-beam exposure time which is very expensive. In addition during e-beam exposure it is necessary to use proximity effect correction to reach the correct exposure dose. To simplify the proximity effect correction, it is advantageous to have large patterns in a different exposure from the small ones. The details about the proximity effect correction will be discussed in Section 3.5. The second 300 nm thick Au layer by photolithography is to put measurement probes on. Patterns in this layer should be far (2 mm) from the e-beam patterns, because 300 nm Au is thicker than an single layer of e-beam resist (around 100-250 nm) and influences the e-beam resist coating. This is also the reason why the thickness of the connecting wires in the first layer is limited to 25 nm.

The device has to be fabricated in the final layer to avoid variation or damage caused by Au contact processes. For example the Ni thin film could be oxidised during baking or etched in developer. An experimental result shows that the Ni became non-conductive after the deposition of a Au layer as shown in Figure 3.2. Figure 3.2(a, b) are images of a non-conducting device taken by helium ion-beam microscope with (b) at higher resolution than (a). It can be seen that the Au wires are connected to the Ni film. The I-V measurement indicates that the Au wires were conducting, but the Ni film was not. The Ni film has been confirmed to be conductive before the Au layer is put on, therefore it became non-conductive during the following processes. All the e-beam resist spinning, baking, exposure

and development processes have direct contact with the Ni thin film. Any damage during these processes could result in degration to the Ni film. The third Au

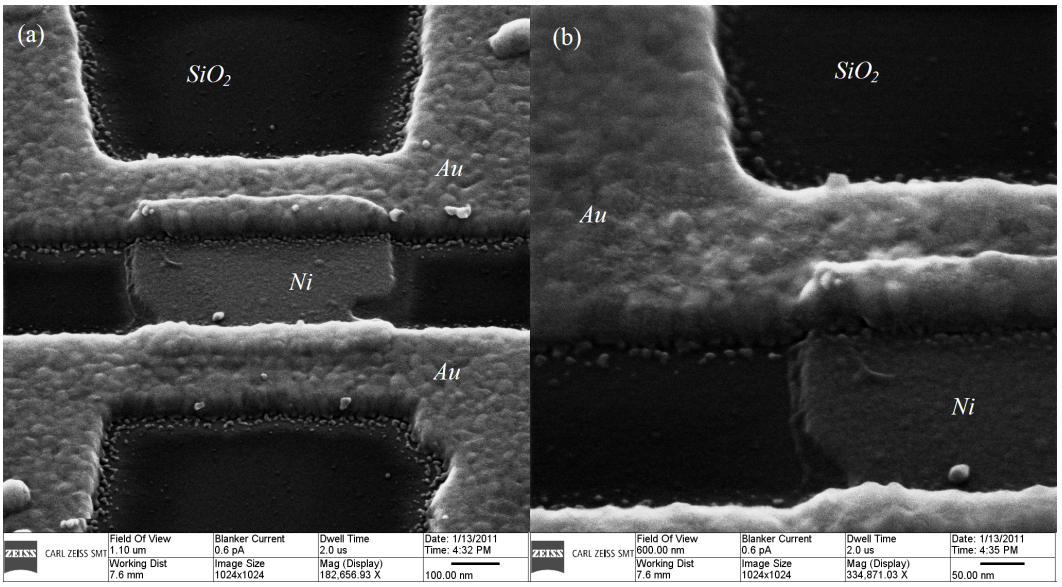

FIGURE 3.2: (a, b) 45° tilted HIM micrograph of the connection between the Au and Ni thin film. It can be seen two Au wires are on top of a piece of Ni film and there is almost no gap between the two metal layers. They are showing the same device with different magnification.

layer fabricated by e-beam lithography is for lithography alignment purpose. The maximum allowed value of the alignment mismatch to connect a Au wire to our H-shaped spin valve is smaller than 50 nm. Figure 3.3 shows a schematic pattern to explain the alignment allowance. Figure 3.3(a) shows the connection between the Ni film and Au film. The limit of alignment is on the narrow (high coercive) side of the spin-valve. Figures 3.3(b,c,d) show the far right, middle and far left allowed positions of the Ni film. The alignment mismatch between a photolithography layer and an e-beam lithography layer is larger than 50 nm, because the aligner EVG620T's UV lamp has two energy peaks around 365 nm (i-line) and 436 nm (g-line) whose pattering size variation is about 100 nm. The size variation of the photolithography could come from the resist spin coating, gap width between mask and wafer, development condition and lamp's age, but largely depended on the exposure wave length. The same variation in e-beam lithography can be well controlled down to sub-20nm region. The fourth layer of Au is used to connect the first and third layers. When we put a thin layer on top of a thicker layer, there is a gap at the joint. Figure 3.4(a) shows the position where the disconnection happens. Figure 3.4(b) shows the gap between two layers which results an open circuit. Thus a fourth layer of Au thicker than both first and third layers is used

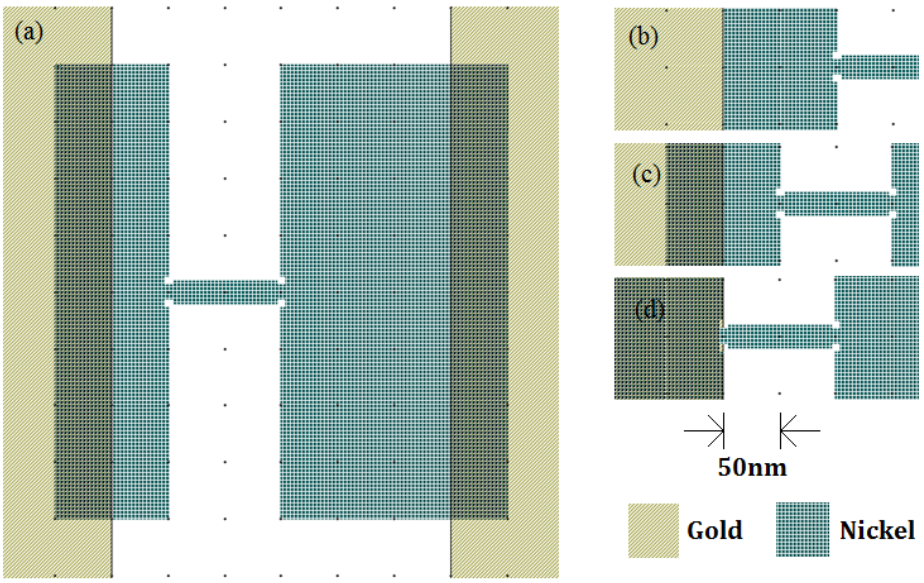

FIGURE 3.3: (a) Schematic diagram of an H-shaped spin-valve connecting to two Au wires. The distance between two dots is 50 nm. (b) maximum allowed displacement to the far right. (c) non-displacement position. (d) maximum allowed displacement to the far left

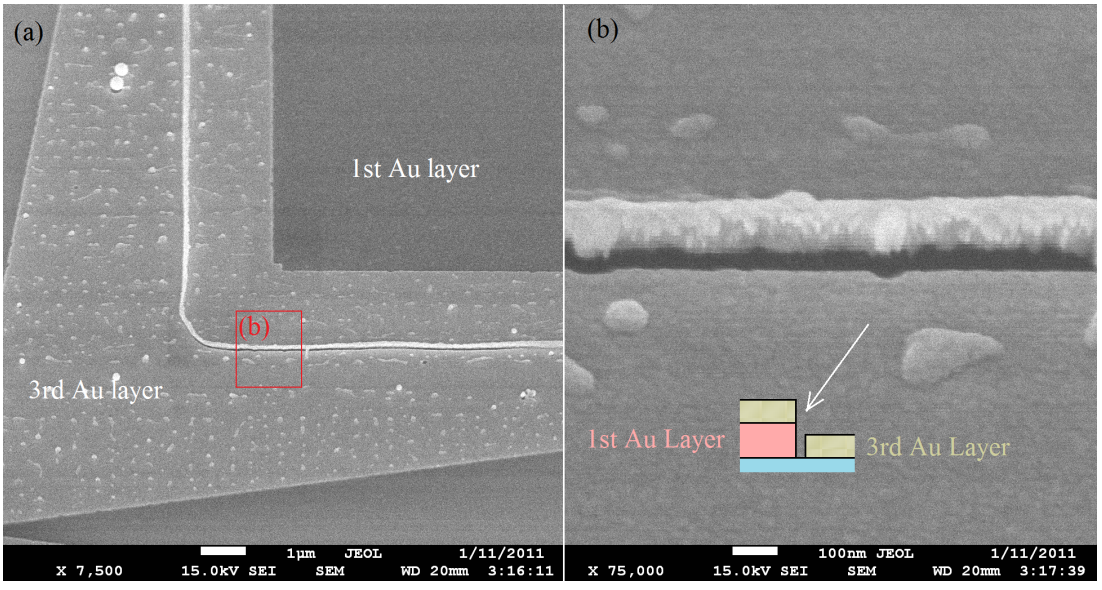

FIGURE 3.4: (a) SEM micrograph of a gap between the first and third Au layers without the fourth. (b) tilted SEM micrograph of the disconnected gap at higher magnification. A schematic diagram shows the cross section of overlapping and the imaging angle

to solve this problem. The reason why a gap appear here is due to the positive photoresist lift-off which is explained in the following section. The fabrication procedures could be found in Tables 3.1 and 3.2. Details of each process are introduced in the related sections.

TABLE 3.1: Fabrication procedures of photolithography

Procedures	Steps
Layer 1 Au	6" wafer $<100>$ P 1-36 Ω
Oxidation	Thermal oxidation 100nm Wet
Lithography	Dehydration for 2 hours 210 °C
	S1813 at room temp 30 min
	Spinning 5000 rpm 1.2 μm
	Hot-plate 95 °C for 2 min
	Exposure 620T 1.8 s 36 mJ/cm^2
	Developer FM319 30-32 s
	Water rinse 30s
Au deposition	Au 22 nm on Cr 3 nm BAK600
	Room temperature 5×10^{-6} mBar
	Cr deposition rate 5 Å/s
	Without breaking the vacuum
	Au deposition rate 1 Å/s
Lift-off Machine	Soak 3×2 min NMP
	1.5 Bar NMP spin speed 200 rpm
	0.5 Bar Water spin speed 200 rpm
	N2 blow + spin 1500 rpm dry
Layer 2 Au	6" wafer
Lithography	Dehydration 2 hours 210 °C
	AZ9260 room temp 30 min
	Spinning 4000 rpm 6 μm
	Hot-plate 110 °C for 165 s
	Room Temperature 30 min in Air
	Exposure 620T 12 s
	AZ400:water 1:3 for 105 s
Au deposition	Au 300nm BAK600
	Room temperature 5×10^{-6} mBar
	Deposition rate 1 Å/s
Lift-off Machine	Soak 5× 2 min NMP
	1.2 Bar NMP spin speed 200 rpm
	Water clean spin speed 200 rpm
	N2 blow + spin 1500 rpm dry

Table 3.2: Fabrication procedures of e-beam lithography

Procedures	Steps
Layer 3 & 4 Au	25×45 mm^2 chip
Lithography	No dehydration
	PMMA MMA room temp 30 min
	MMA spinning 5000 rpm 150 nm
	Hotplate 150 °C for 65 s
	PMMA spinning 5000 rpm 250 nm
	Hotplate 180 °C for 65 s
	Exposure dose 800 μC/cm2
	Developer MIBK:IPA 1:1 90 s
	IPA rinse 30 s
Au deposition	Au 12 nm L3 & 60 nm L4 LAB700
	Pressure 5×10^{-6} mBar
	Soak power 10%
	Deposition rate 1 Å/s
Lift-off	Manual soak in acetone 10 min
	Gently blow with pipette
Layer 5 Ni	25 ×45 mm^2 chip
Lithography	No dehydration
	PMMA MMA Room temp 30 min
	MMA spinning 5000 rpm 150 nm
	Hotplate 150 °C for 65 s
	PMMA spinning 5000 rpm 250 nm
	Hotplate 180 °C for 65 s
	Exposure dose 1000 $\mu C/cm^2$
	Developer MIBK:IPA 1:3 120 s
	IPA rinse 30 s
Ni deposition	Ni 20 nm + Au 2 nm LAB700
	Pressure 5×10^{-6} mBar
	Ni soak power 23% 25 min
	Deposition rate 1 Å/s at power 20%
	without breaking the vacuum
	Au soak power 10%
	Deposition rate 1 Å/s
Lift-off	Manual soak in acetone 5 min
	Gently blow with pipette

3.2 Photolithography

Photolithography is widely used in the semiconductor industry in both micro- and nano-fabrication. It selectively removes parts of a thin layer of photoresist to generate patterns on a substrate. Similar to photography, it uses light to transfer patterns from mask to photoresist and washes away the exposed (positive photoresist) or unexposed (negative photoresist) area chemically. The intensity of the UV, DUV or EUV light is high and the sensitivity of the resist is relatively low such that being exposed to yellow light does not lead to the exposure. The minimum feature size of the contact mode is given by [70],

$$CD = c\sqrt{\lambda h} \tag{3.1}$$

where CD is the minimum feature size (critical dimension), c is a constant in most cases equals to $\sqrt{2}$, λ is the incident wavelength and h is the thickness of resist. As we are using a hard contact mode, there is no gap between photoresist and mask. We can calculate for our aligner EVG 620T with a wavelength of (i-line) 365 nm and 1.2 μm S1813 photoresist CD is about 936 nm.

The experimental difference between positive and negative photoresist is summarized in Table 3.3. For lift-off processes it is required that the resist is removed in areas where metal is required. For the positive resist, the metal patterns designed in the software (Layout Eidt Pro. v11, L-edit) is transparent on the mask. We call this dark field mask which means the empty fields in the design are not transparent on the mask. For the negative photoresist, we still draw the metal pattern in the design, but make a light field mask afterwards. The light field mask means the empty fields in the design are transparent. During exposure the resist close to the mask absorbs more energy than the bottom, thus the side wall of the positive resist has an acute angle whereas the negative has an obtuse angle. An obtuse angle results in an undercut naturally, therefore in most lift-off processes, negative resist is preferred. However, in our experiment positive resist was used due to the requirement of electron beam alignment. Figures 3.5 and 3.6 show the lift-off process of the two types of photoresist. Due to the shape of side wall, the edge of metal film is tilted up when positive resist is used. This structure has better electron back scattering signal which gives better E-beam alignment. Figures 3.7 and 3.8 show the SEM micrographs of the cross section view of positive and negative resists respectively after metal deposition.

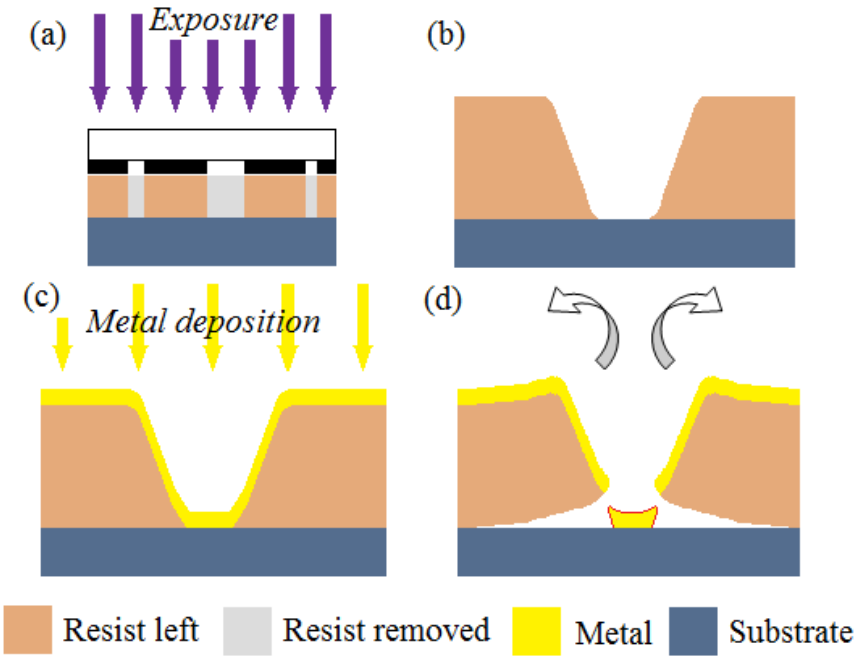

FIGURE 3.5: Schematic diagram of cross section view of positive photoresist lift-off (a) light field mask exposure. Metal is deposited on the transparent area. (b, c, d) lift-off processes. The edge of metal films is tilted up, due to the shape of resist.

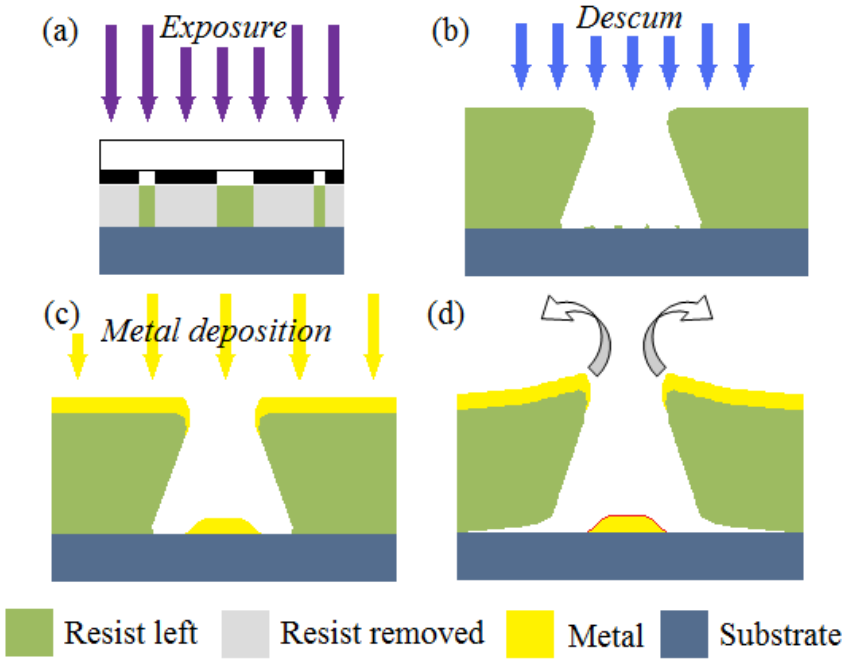

FIGURE 3.6: Schematic diagram of cross section view of negative photoresist lift-off (a) dark field mask exposure. Metal is deposited on the non-transparent area. (b, c, d) lift-off processes. The edge of metal films has a down slope, due to the shape of resist. (b) Descum process to clear the resist dots on the bottom

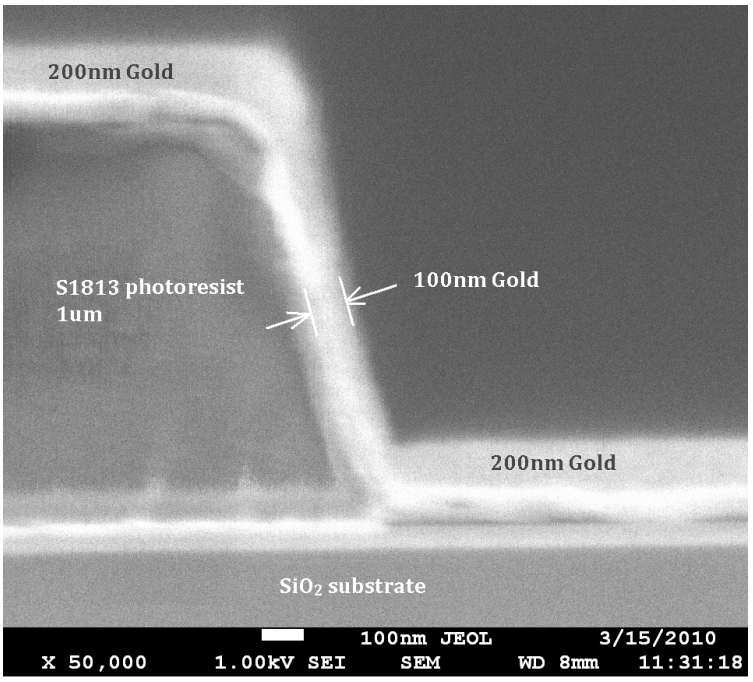

FIGURE 3.7: SEM micrograph of the cross section view of S1813 positive photoresist after Au deposition. The exposure condition was 5000 rpm room temperature spinning, 95 °C baking for 2 min, exposure dose 365 nm - 436 nm i-line + g-line 20 mW/cm^2 × 1.8 s (36 mJ/cm^2), development in FM 319 RT 30 s, and water rinse 30 s.

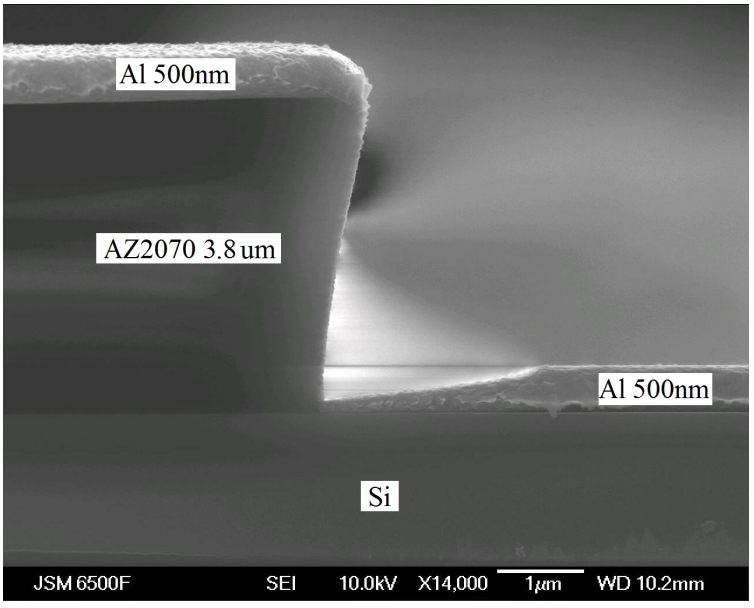

FIGURE 3.8: SEM micrograph of the cross section view of AZ2070 negative photoresist after aluminium deposition. The exposure condition was 6000 rpm RT spinning, 110 °C baking for 1 min, exposure dose 365 nm i-line 9.5 mJ/cm^2 × 7.9 s (75 mJ/cm^2) , development in AZ726 MIF for 75 s and water rinse 30 s. (Thanks to Dr. Kai Sun for supplying the SEM image)

TABLE 3.3: Difference between positive and negative photoresist for lift-off process

Photoresist	Positive	Negative
Cleared area	exposed	unexposed
Mask	dark field	light field
Resist side wall	$\leq 90°$	$\geq 90°$
Undercut	additional layer required	undercut naturally
Lift-off pattern edge	tilted up	down slope
Descum	not required	required

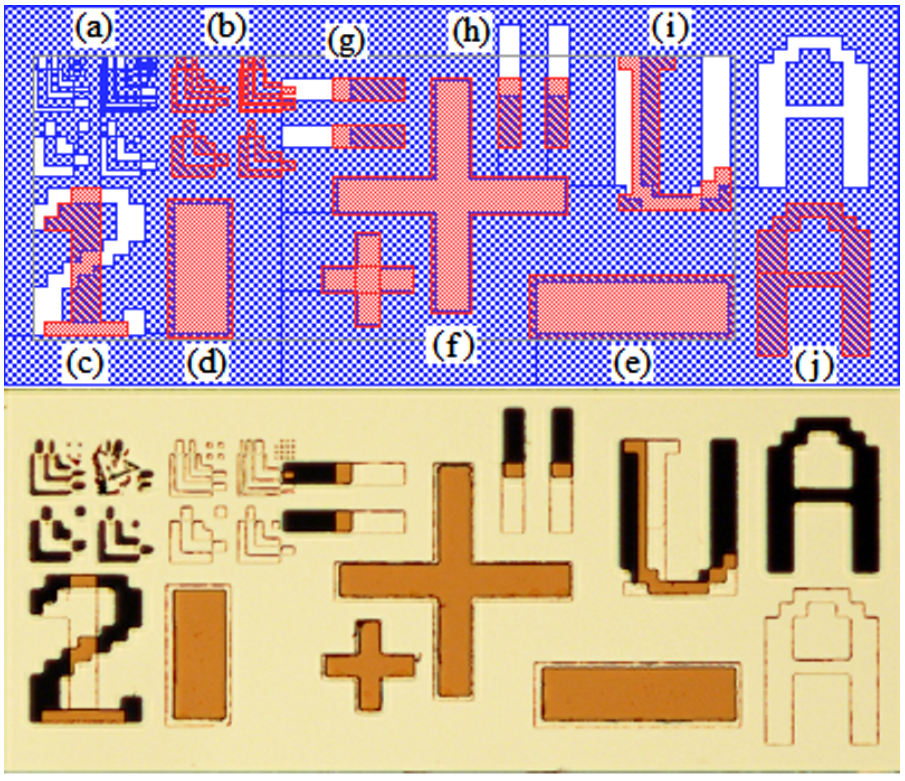

FIGURE 3.9: Schematic diagram of the alignment mark and the optical microscope micrograph of the patterns after alignment. (a, b) resolution test patterns for the second and first layers respectively. (c) The layer number. (d, e) alignment marks for low magnification microscope, 2 μm accuracy. (f) alignment mark for coarse alignment, 1 μm accuracy (g, h) alignment marks for fine alignment, 0.5 μm accuracy. (i) Name for the upper or under layers. (j) Name of alignment marks

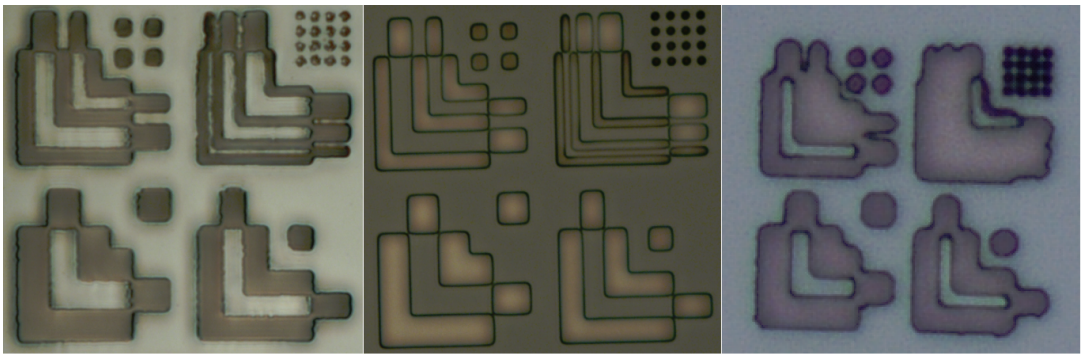

A B C

FIGURE 3.10: The optical microscope micrographs of the resolution test patterns of (a) AZ2070, (b) S1813 and (c) AZ9260. The wavelength used in the test was 436 nm. The resist thickness is (a) 3.6 μm, (b) 1.2 μm and (c) 6 μm. According to Equation 3.1, in the hard contact mode the theoretical resolution is (a) 1.7 μm, (b) 1 μm and (c) 2.3 μm. The experimental results are (a) 2 μm, (b) 1 μm and (c) 3 μm.

Figure 3.9 shows the photolithography alignment mark design and an optical microscope image of an alignment result. Figures 3.9(a, b) are resolution sensors to detect the resolution in an exposure. Some alignment mismatch is due to the low resolution, thus the sensor is needed. For example the resolution of S1813 (1.2 μm), AZ2070 (3.6 μm) and AZ9260 (6 μm) was tested to be 1 μm, 2 μm and 3 μm, respectively (Figure 3.10). Figure 3.9(c) indicates the number of which layer the mark is on. In some project there are more than 10 masks. This number could help to recognise which layer the mark belongs to, especially for the marks on the wafer. Figures 3.9(d, e) are alignment marks used in an aligner with only low magnification microscopes. The alignment accuracy is better than 2 μm. Figure 3.9(f) is the alignment mark for coarse alignment whose accuracy is about 1 μm. Figures 3.9(g, h) are alignment marks for fine alignment whose accuracy is about 0.5 μm. Figure 3.9(i) is to indicate which layer is being focussed on by the optical microscope during the alignment process Figure 3.9(j) is the name of the alignment mark. For example, 'A' is to align Layer 2 to Layer 1 and 'C' is to align Layer 4 to Layer 2.

3.3 Metal evaporation

The thin film magnetic material and Au wires are deposited by an electron beam evaporator. The material is placed in a crucible and heated up by an accelerated electron beam in a vacuum environment. The metal atoms will be evaporated and

deposited on all surfaces facing the crucible. The deposition rate is tested by a Au crystal sensor. The thickness deposited on the sample is proportional to the sensing thickness. The ratio between the deposition and sensing, also known as 'tooling factor' is tested by the average of 3 depositions. The evaporator Leybold Optics BAK600 and LAB700 will be used in the experiment. Numerous facts influencing the film quality, such as beam deflection, soak power, soak time, vacuum level and substrate temperature will be discussed in the next few paragraphs.

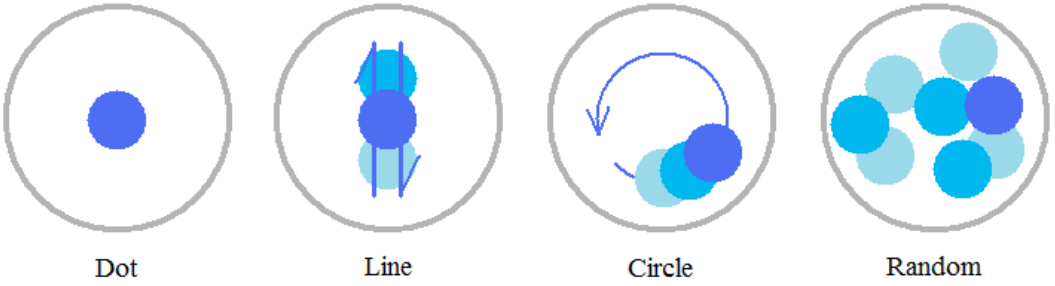

FIGURE 3.11: Schematic diagram of electron beam deflection patterns of the evaporator. The outer circle indicates the edge of the crucible and dots are the beam spots.

The deflection is controlled by a voltage bias added in a plane X-Y perpendicular to the beam path. Figure 3.11 shows some commonly used deflections. The beam spot in the crucible is a dot when no bias is added, a line shape when only X or Y has an added sine signal, a circle when X and Y are added sine signals with the same frequency but a $\pi/2$ different phase and random when adding random signals. Which spot to use is determined by the size of the beam spot and crucible, material and deposition rate. The spot and circle shapes are frequently used. In the BAK600, the crucible size is around 1.5 cm in diameter, for most materials the dot pattern is used to get a stable deposition rate and a uniform film. In the LAB700, the crucible is about 5 cm, so normally circular deflection pattern is preferred.

In our evaporators several parameters need be considered to control the electron beam power, such as rise time, soak time, soak power and deposition rate. The acceleration voltage is a constant value in the evaporator, and the soak power is a percentage value proportional to the emission current. Figure 3.12 shows the power versus time curve of a deposition cycle. The soak power 1 is the power the evaporation is about to start but almost no deposition happens at this power. It requires rise time 1 to increase power and keep this power for a period which is

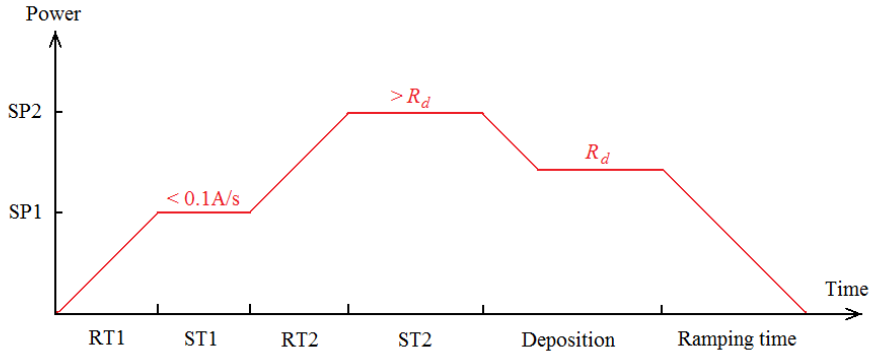

FIGURE 3.12: Plot of power against time of a deposition process. The parameters rise time (RT), soak time (ST), soak power (SP), deposition rate (R_d) and ramping time are set manually in the evaporator

called soak time 1. This process ramps up the power evenly to prevent exposure due to the uneven heating. The soak power 2 is normally the power which gives the required deposition rate. The calibrated soak time 2 and soak power 2 can give an even deposition rate when the evaporation starts. For some materials requiring high purity such as Ni a long soak time 2 can help to get rid of oxide on the surface of the material. However for expensive materials such as Au a short soak time 2 could save the cost. Normally the deposition rate setting is the same rate as soak power 2, but in our experiment, a higher soak power 2 is selected to clean the seed before deposition starts. A ramp down time after evaporation is unnecessary for most materials. It could help to release strains due to the fast cooling, which might cause exposure when it heats up next time. In magnetic materials, the strain could result in magnetisation in a certain direction as we discussed before and it will generate a magnetic field around the crucible. In the evaporation we do not want the electron beam to be bent by an unexpected magnetic field so a ramping time is necessary for Ni deposition.

High vacuum gives better film quality. In our project, all the four layers are deposited under a vacuum of 5×10^{-6} mBar. Also a heated the substrate during the evaporation could help to increase the film quality. However, in a lift-off process it is better not to heat up the resist, because the resist may become hard and difficult to remove. We hence left the substrate at ambient temperature.

The Ni thickness should be as low as possible to avoid out of plain field, because in thin film fabrication evaporated Ni is not a continuous film but has a grain size (cannot be detected in our cleanroom). If it is too thick there will be magnetisation perpendicular to the film. However the reduction to thin film thickness was limited

by several factors. Firstly the Ni film has to be thicker than the Au layer to get a good electric contact (low contact resistance). In the first device the Au wire thickness was 20 nm, so the minimum Ni thickness had to be 20 nm. In the later experiment we optimized the fabrication processes and the Au film thickness was reduced to 12 nm so that the Ni film thickness can be reduced to 14 nm.

3.4 Lift-off

The process of lift-off has already been introduced in the photolithography process. We have explained why we use positive photoresist for lift-off. The drawback of positive photoresist lift-off is that on the slope there is a thin layer of metal connecting the bottom and top layer (Figure 3.7). This connecting layer is thinner than the planar film, it requires high pressure (up to 1.5 Bar) solvent in the lift-of to remove this. Figure 3.13 shows the results of a manual and machinery lift-off experiment. It can be seen the metal on the slope stayed after manual lift-off but was completely removed by machinery lift-off. This problem only exists in the single layer positive photoresist lift-off, but not in a double layer resist with an undercut which will be introduced in the following section.

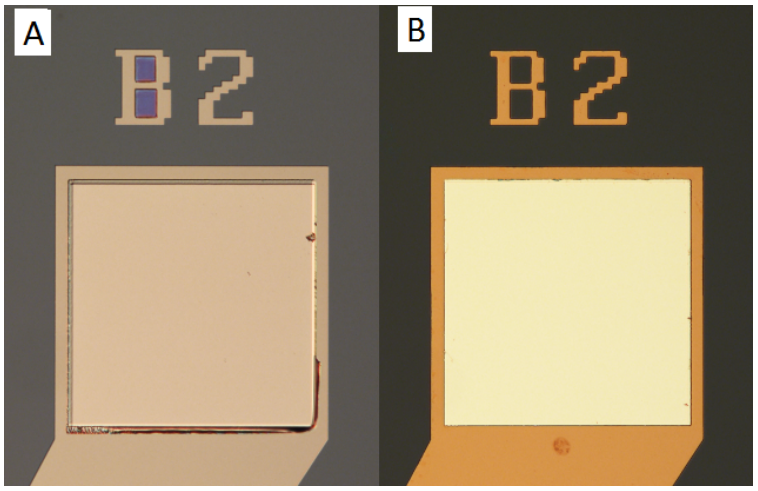

FIGURE 3.13: Optical microscope micrograph of (a) manual (b) machinery lift-off results. It can be seen that in the manual lift-off the island structure like in the letter 'B' is not removed and the edge is not clean, whilst the machine lift-off does not have problems like this.

3.5 Electron-beam lithography

3.5.1 Introduction

Electron beam lithography is a common technology for nanometer sized patterning. Compared to photolithography it has smaller diffraction effect. As we discussed in the photolithography section the minimum pattern size is limited by the lamp's wavelength. The de Broglie wavelength of an electron (4 pm at 100 kV) is much shorter than wavelength of EUV (10 nm - 120 nm). The e-beam lithography is a powerful tool in an experimental lab, but in industry it is not widely used due to its slow writing speed in production processes. However, an instrument named MAPPER (massively parallel electron beam lithography) is being developed to increase the writing speed by generating as many as 13,000 electron beams to write in parallel. It can supposedly write ten 150 mm wafers per hour at a resolution of 45 nm [71].

In our experiment both the H-shaped Ni structure and the Au wires which it aligns to, are fabricated by e-beam lithography and lift-off. In this section, I am introducing the fabrication procedures of the e-beam lithography in detail, especially the method of operating the JEOL 9300FS e-beam lithography system to get high alignment accuracy and the electron beam energy proximity effect correction with the Genesis software. A checkerboard dose sensor and its exposure results are introduced to show the agreement of proximity effect correction theory and experimental practice. At last the limitation of e-beam lithography in the lift-off is discussed together with the cross section micrographs taken by scanning electron microscope (SEM) and helium ion beam microscope (HIM).

3.5.2 Exposure dose and proximity effect correction

As mentioned before, a good lift-off requires an under-cut to separate the top and bottom layers of metal. A common combination is a polymethy methacrylate (PMMA) layer on top of a copolymer (MMA) layer. The molecular weight of the PMMA is larger than the MMA, thus MMA is dissolved faster than PMMA in developer after exposure. Therefore an under-cut structure is created. In our experiment PMMA and MMA bi-layer structure was tested with different exposure conditions. The recipe of processing a PMMA on MMA exposure and lift-off can be found in Table 3.2. The exposure dose is the electron density to be injected

into the e-beam resist during exposure. The dose is proportional to the energy injected in the exposure area. Due to the electron scattering effect the energy distribution has a wider range than the electron beam spot size. Therefore the profile of the removed resist is always slightly different from the exposure pattern. This causes big problems when the patterns are dense and on the nanometer scale. A proximity effect correction (PEC) is introduced to solve this problem by calculating the energy density distribution of an exposed area. Then the pattern can be exposed by optimised shape and dose.

The software we used to do the PEC calculation is called Layout BEAMER developed by GenISys GmbH (Germany) [72]. In the software the exposure energy is given as,

$$E(x,y) = D(x,y) \otimes f(r) \tag{3.2}$$

where E is the absorbed energy in resist, D is the applied dose and $f(r)$ is point spread function given by a multi Gaussion function,

$$f(r) = -\left(g_\alpha(r) + v_1^* g_{\gamma 1}(r) + v_2^* g_{\gamma 2}(r) + \eta^* g_\beta(r)\right) / (1 + v_1 + v_2 + \eta) \tag{3.3}$$

where g_σ is a normalised Gaussion of width σ, α is used for short-range effects such as scattering in the resist, β & η are for the long-range back-scatter contribution and γ & v are for the mid-range effects.

There are two types of PEC which are shape PEC and dose PEC. The shape PEC changes the shape of designed pattern in the exposure process to correct the energy distribution to get the designed pattern. The dose PEC exposes the pattern as it is designed, but uses various of doses in the pattern area. There is a base dose in the dose PEC exposure and the dose variation is based on the base dose, for instance from -20% to 60% of the base dose. For ultra high resolution exposures, both of these methods should be used together to correct the energy distribution. In our experiment only dose PEC is considered. To test the base dose, we developed a checkerboard dose sensor (Figure 3.14). Firstly expose the dose sensor on PMMA + MMA e-beam resist with different doses, for example from 375 μC/cm^2 to 525 μC/cm^2 with a step of 25 nm. Then check the result under an high resolution SEM, such as JEOL 7500 field emission SEM. Figure 3.16 shows a group of exposed patterns from under dose to over dose. The size of the beam blur can be measured from the micrographs of checkerboard. Figure 3.17 shows a plot of the beam blur as a function of the exposure dose from a dose test experiment. The circles are experimental points, and the correct base dose was determined to

be 500 μC/cm^2. Figure 3.15 shows an interesting result found during dose test experiment. The diameter of an island structure cannot be smaller than twice the size of the undercut. Otherwise the island structure disappears because the MMA layer is all etched by the developer.

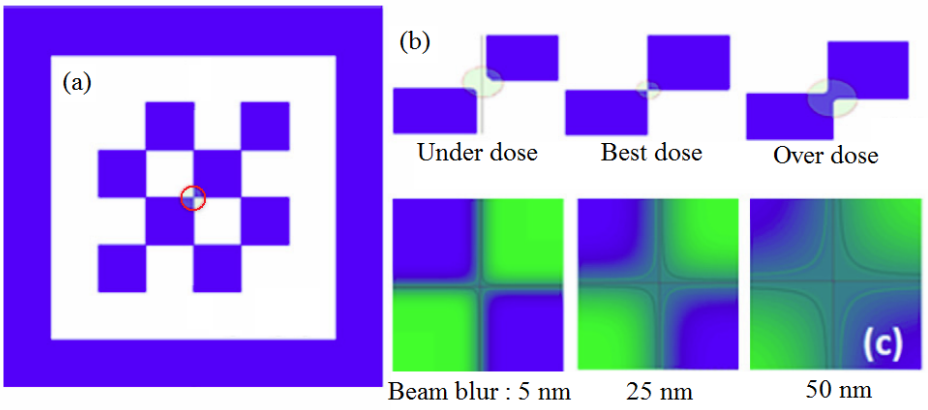

FIGURE 3.14: (a) Schematic diagram of the checkerboard dose sensor. (b) schematic diagram of E-beam resist of the under exposure, correct exposure and over exposure. (c) schematic diagram of the measurement of beam blur size. The blue areas are empty after development

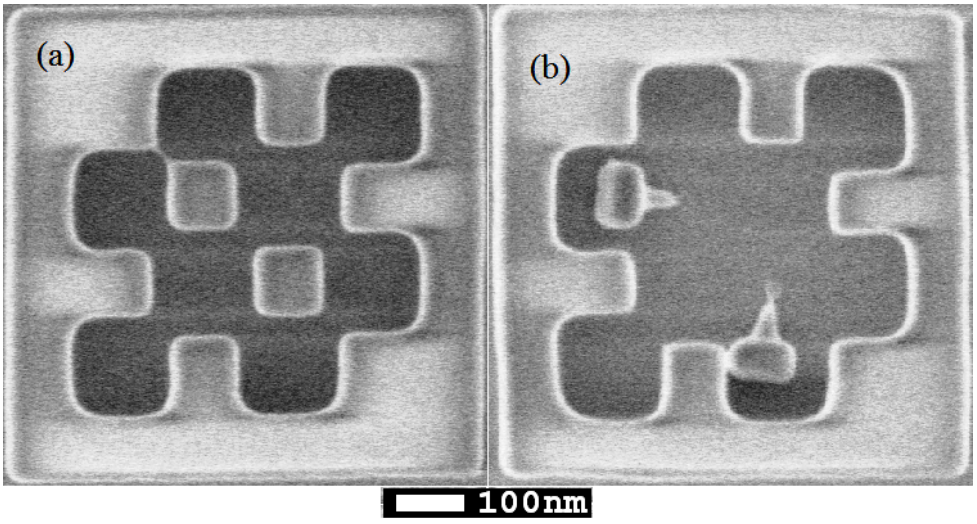

FIGURE 3.15: SEM micrographs of a checker board exposure on the PMMA + MMA bi-layer resist with island structure of 100 nm (a) and below (b). The brighter areas are resist whereas darker areas are empty. (a) the minimum island size which could still stand after exposure. (b) resist islands fallen down due to the undercut etched too much of the MMA layer

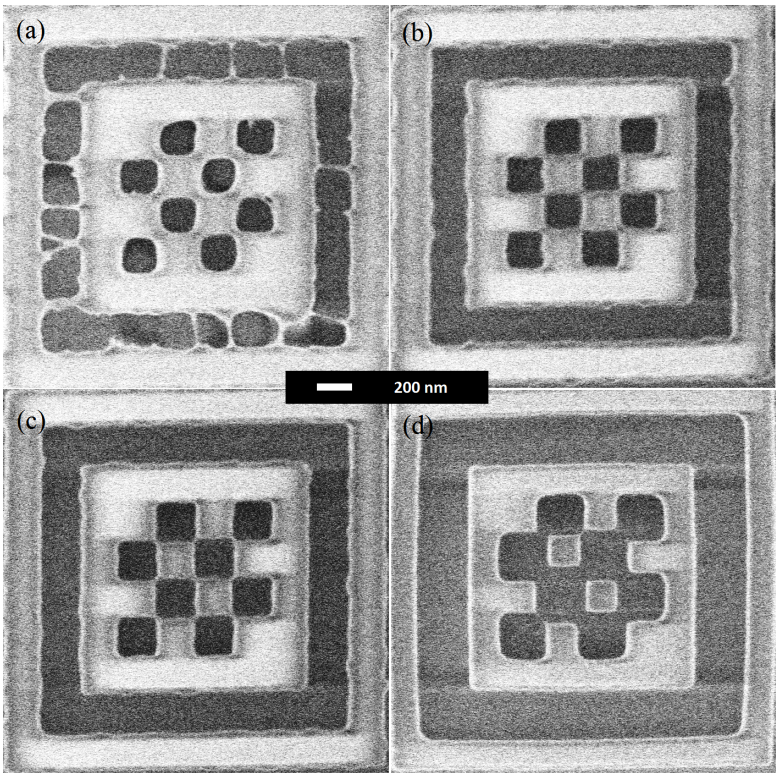

FIGURE 3.16: SEM micrographs of a checker board exposure on the PMMA + MMA bi-layer resist. (a) under-dose, (b) correct dose, (c) slight over-dose, (d) over-dose.

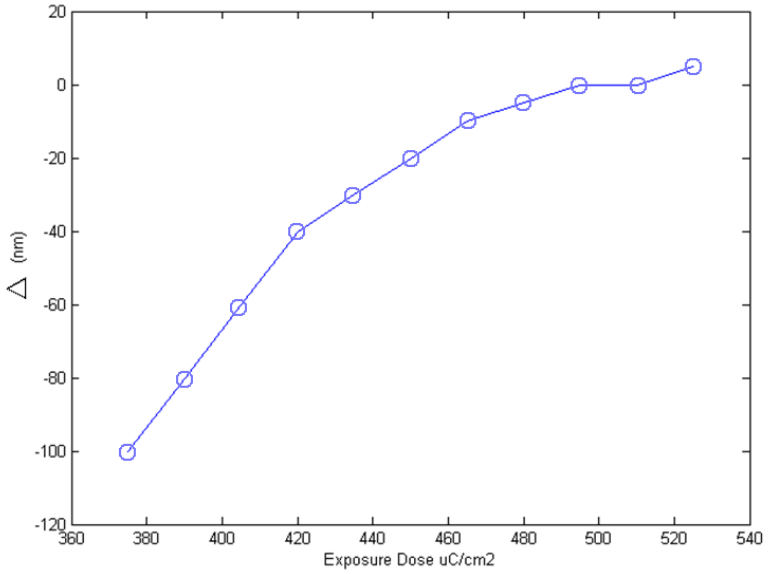

FIGURE 3.17: Plot of beam blur, Δ as a function of exposure dose. Circles are experimental points. The beam blur is the connection size between two empty areas in the checkerboard dose sensor. Positive value means over-dose whereas negative value means under-dose

3.6 Helium-ion Beam Milling

3.6.1 Introduction

Helium ion microscopy is a surface imaging technique which involves scanning a helium ion beam across a sample surface and forming an image from the secondary electron emission. The helium ion microscope (HIM) is similar in operation to a scanning electron microscopy (SEM). The larger mass and smaller de Broglie wavelength of a helium ion compared to that of an electron, in addition to an atomically sharp source, enables the HIM to focus the charged particle beam to a small spot on a sample. Furthermore, as the helium beam enters the sample, it is scattered little as it interacts mainly electronically with the sample in the first few tens of nanometres of the surface. These factors lead to a smaller interaction volume and a higher resolution compared to an SEM. A good field emission gun (FEG)-SEM can achieve an edge resolution of around 1 nm [73, 74] whereas the latest commercially-available versions of the HIM are rated at 0.35 nm [75]. However, the HIM is not only an imaging tool but also a nano fabrication tool. Similar to a gallium focused ion beam system (FIB), the helium ion beam can mill material by direct ablation of surface atoms when the beam dose is large enough, or deposit material when a gas injection system is used [76]. Compared to a FIB, the HIM can generate a smaller beam and so is capable of higher resolution patterning. The low mass of helium compared to gallium results in a much reduced sputtering yield and therefore lower milling rates, making the technique suitable for the controlled milling of sub-20 nm features. The technique, although in its infancy, has been used to mill a variety of materials including monolayers of graphene for nanoelectronic applications [75, 77] and thin SiN membranes for biomolecular analysis applications [78].

3.6.2 HIM milling fabrication

The helium ion beam milling was carried out with a Carl Zeiss OrionPLUS^{TM} HIM. The sample was cleaned by soaking in NMP at room temperature followed by rinsing in IPA to remove organic materials like e-beam lithography resist and carbon tape residue before loading into the HIM. This is an important step because hydrocarbon contamination of this type can be efficiently cross-linked by the helium beam, leading to build-up of material in the area where the beam is scanned and so prevent successful milling. The H-shaped DWMR device pattern was de-

fined in binary bitmap format, with one pixel corresponding to 1 nm^2, and this was imported into the internal pattern generator system of the HIM. The HIM was used in imaging mode to locate and center the pre-defined Ni pad. Imaging was stopped and then the pattern generator was used to direct the beam, milling out the gap region to leave the bridge structure joining the two rectangular regions. The acceleration voltage was 30 kV, and with a milling current of 1 pA, dwell time of 10 μs and pixel spacing of 1 nm, the base dose was 6.154×10^{15} ions/cm^2. Multiple scans (repeats) were used to deliver the required total dose for milling completely through the Ni layer. The required total dose was first estimated by Monte Carlo modelling and then optimised experimentally using SEM inspection and resistance measurements. Several devices were fabricated with different bridge lengths (=gap width). The typical milling time for the optimised dose used to fabricate successful devices was about 70 s.

To determine a rough starting point for the dose required to mill out the gap to create the DWMR device using the He ion beam, Monte Carlo simulations were performed using the SRIM software package [79, 80]. A model was constructed within the software of 30keV helium ions interacting with a 14 nm thick Ni layer on top of a 100 nm thick SiO_2 layer on a silicon substrate. From a simulation of 1×10^5 ions, the sputtering yield, which is the number of atoms removed from the sample per incident ion, was calculated to be 0.09 atoms/ion. From the atomic weight and density of Ni (58.69 and 8.908 g/cm^3, respectively) and the volume of material to be removed, the required total dose is calculated to be 1.39×10^{18} ions/cm^2. This is 223 times the base dose specified in the experimental section and so 223 repeats can be used to deliver the required dose. This represents a lower bound for the actual dose needed to remove the required amount of material because the SRIM simulation assumes that the surface remains flat and featureless. In reality, as the trench is formed it will become increasingly difficult to sputter material due to redeposition on the trench walls. The actual sputtering yield will decrease during the milling operation as more than one sputtering event is required to completely remove an atom from the trench. Therefore, for the experimental optimisation procedure, 200$\times$ the base dose was used as the minimum applied dose.

For experimental optimisation of the milling dose there are several ways to detect the milling depth, including atomic force microscope (AFM) and cross section imaging in SEM or HIM, but in this case the gap width, at around 20 nm, is too small to be measured by these methods. Instead, the milling depth in the 20 nm-wide gap structure was monitored by top-down inspection with SEM and

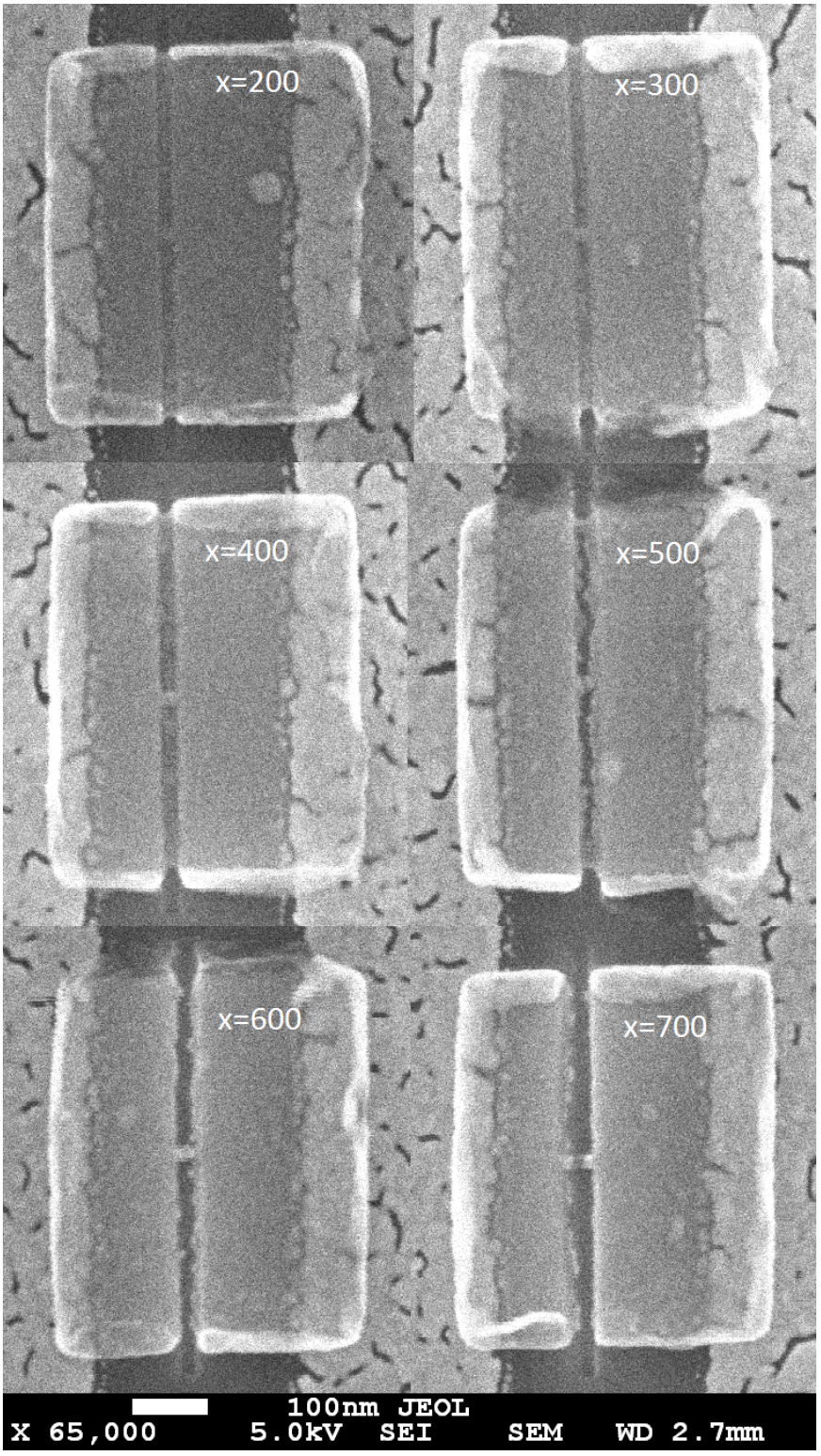

FIGURE 3.18: SEM images showing the device after helium ion milling, with different doses, x, where x refers to the number of repeated scans with a base dose (one scan) of 6.154×10^{15} ions/cm^2. The total dose for each device is therefore x times the base dose. The device is fabricated in a 14 nm-thick Ni layer, sitting on two 9 nm-thick Au wires. The substrate material is 100 nm-thick SiO_2 thermally grown on top of a <100> P-type silicon wafer.

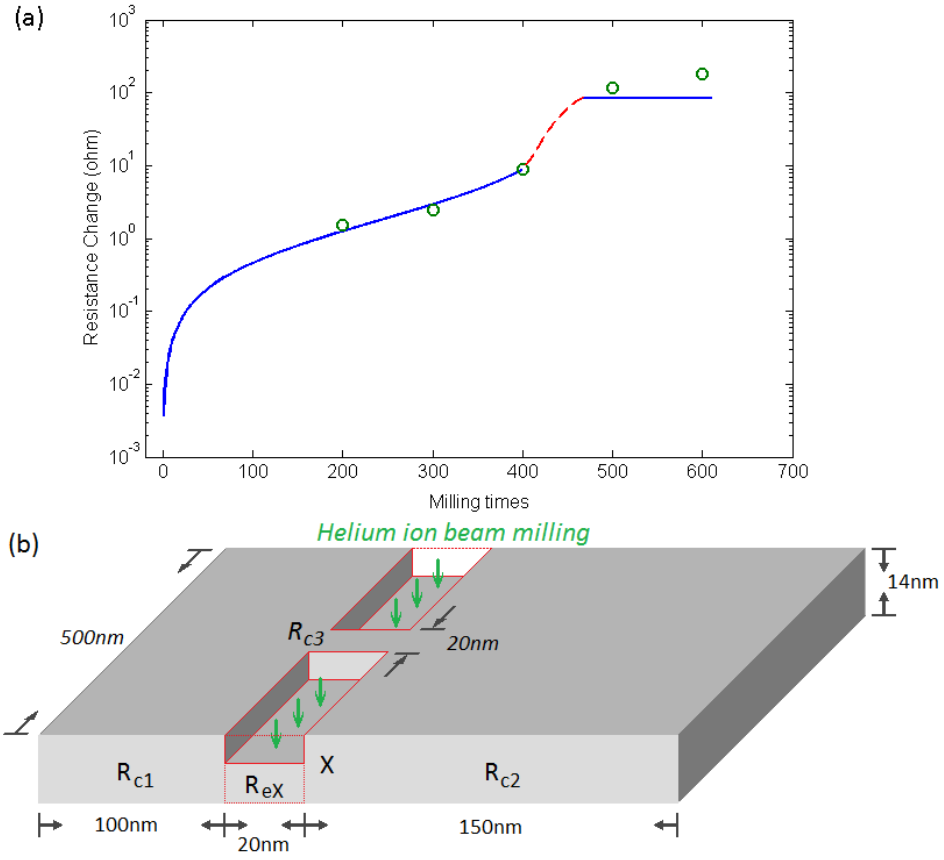

FIGURE 3.19: (a) plot of resistance versus helium ion beam dose. Green empty circles are experimental results. The blue curve is fitted data from the resistance model and measurement result when $x = 200$, 300 and 400. The red dashed line shows the curve when $0.85 \leq x \leq n$ in which region the bridge to pad geometry is taken into consideration; (b) shows the 3-D view of the device in the milling process. R_{c1}, R_{c2}, and R_{c3} are constant during milling and x represents the number of repeated milling scans of the base dose. We assume the milling rate is constant, so x is proportional to the milling depth.

by measuring the resistance of devices given different milling doses. The dose range was from 200 ($x = 200$) to 700 ($x = 700$) repeated milling scans of the base dose. SEM images of the devices milled with the range of doses are presented in Figure 3.18. For the doses when $x = 200$, 300 and 400, the gap is visible but the film appears to be still connected at the bottom, as the contrast from the gap area is higher than that of the substrate. Above a dose of $x = 500$, the contrast from the gap approaches that of the substrate and in the image of dose $x = 600$, the gap appears to be completely milled through. For dose $x = 700$, the bridge appears to be broken, indicating over-milling.

The resistance of each device was measured by a 4-point measurement system in which a constant current is driven through the bridge from two terminals and the

voltage is monitored at the other two ends. The main contribution to resistance originates from the Ni material between the two Au wires, mostly from the bridge structure. The corresponding resistance measurement results of the devices in Figure 3.18 are shown by the green circles in Figure 3.19a. The total resistance R_x can be expressed as a series resistance of the left and right pad (R_{c1}, R_{c2}, respectively) and the parallel resistance of bridge R_{c3} and area to be milled R_{ex} with x the milling quantity as displayed in Figure 3.19b and Eq. 3.4.

$$R_X = R_{c1} + (R_{c3}//\mathrm{R}_{eX}) + R_{c2} \tag{3.4}$$

Here R_x is the resistance after x times repeated milling scans with the base dose, and $x = 0$ is for the original device whose resistance $R_0 = 20\Omega$. The size of each part is measured by the SEM image of the sample. As long as the milling is not complete, $R_{c3} >> R_{e0}$, R_{c1}, R_{c2}, and can be considered to be constant and the change in resistance can be approximated by Eq. 3.5.

$$\Delta R_X = \left(\frac{x}{n-x}\right) R_{e0} (0 \leq x < 0.85n) \tag{3.5}$$

The values for $R_{e0} = 1.82\Omega$ can be calculated using the geometrical structure. We assume a constant milling rate, no redeposition and no substrate drift during the whole process. The variable x is the number of repeated milling scans with the base dose. The value n is the minimum value of x required to mill completely through the film in an ideal case. It can be fitted to the first 3 experiment points when $x = 200$, 300, 400 whose measurement results were $\Delta R_{200} = 1.5\ \Omega$, $\Delta R_{300} = 2.5\ \Omega$ and $\Delta R_{400} = 9.0\ \Omega$. From Matlab curve fit tool, the extracted value $n = 460$. This corresponds to an experimental milling efficiency of 0.044 atoms/ion, which is about half the theoretical milling rate of 0.09 atoms/ion. When the milling time is closer to n ($0.85 < x \leq n$), significant current will flow through the bridge and the pads cannot be considered to have constant resistance. We have simulated this effect with the software COMSOL 4.2a with the same geometrical size as the fabricated device. When the milling time $x \geq n$ (i.e. the Ni film has been etched through) the resistance change of the bridge and pads compared to the unetched film will be 83.3 Ω which agrees with the experimental result when $x = 500$. When $x = 600$ the resistance change is slightly greater than the calculated value, and at $x = 700$ the circuit is open. This is in agreement with the SEM images in Figure 3.18 which show a split in the the bridge structure for the $x = 700$ dose. The cause of this is drift of the sample, and strain as discussed in the next section.

3.6.3 He-induced strain and swelling

During milling, helium atoms are implanted into the substrate and this can cause sub-surface swelling, leading to strain in the Ni surface layer and eventually to failure of the delicate bridge structure. Sub-surface swelling was evident in samples with gap widths larger than 20 nm, as shown in Figure 3.20 and 3.21. With the milling dose fixed, a wider milling width leads to a larger number of implanted ions. Previous studies have shown that the implanted helium can form voids in the underlying substrate which push against the material above and cause a shape change on the surface [75, 81]. It can be seen from Figure 3.20d and 3.21 that the device size increases with increasing amount of injected helium and this leads to rupture of the bridge at the left hand side. According to the SEM images of the same devices taken about one month after milling (Figure 3.21c), there is no evidence of relaxation in the swollen region due to He out diffusion.

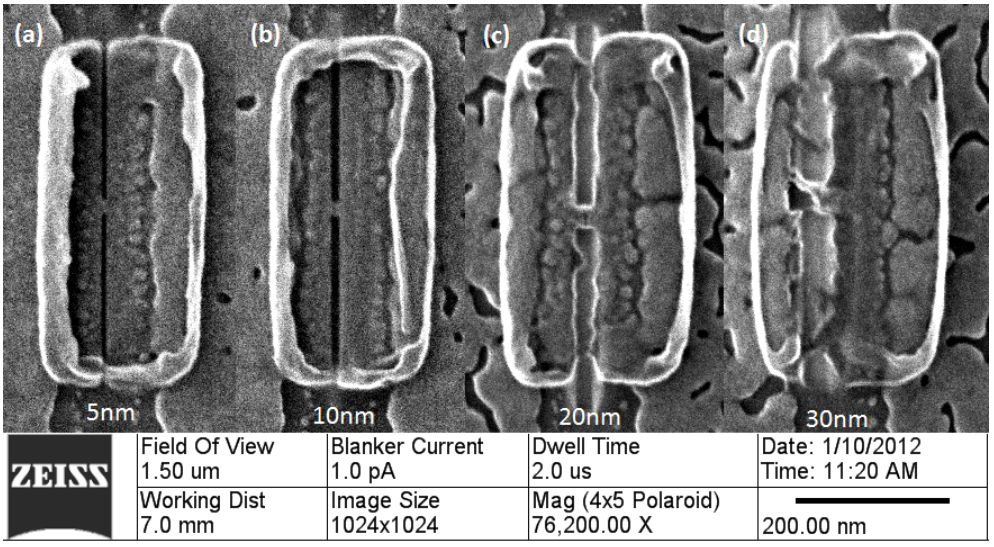

FIGURE 3.20: HIM micrographs of the devices with different pattern width. (a, b, c) devices with milling widths of 5 nm, 10 nm, and 20 nm, respectively, for which the bridge structure remained intact after the milling process. (d) milling width of 30 nm whose bridge was broken due to the strain caused by He implantation into the substrate during milling. The milling dose was 3.69×10^{18} ions/cm^2 for each sample.

The size increase is caused by the high doping density of the He atoms in the Si substrate after milling. The He ions doping concentration can be calculated using the implantation dose, pattern size and interaction volume which is simulated by SRIM. As the milling width is small with respect to the interaction range (250 nm), the He ion doping concentration scales virtually linear with the milling width. Livengood *et.al.* reported in 2009 [82] that at a doping concentration

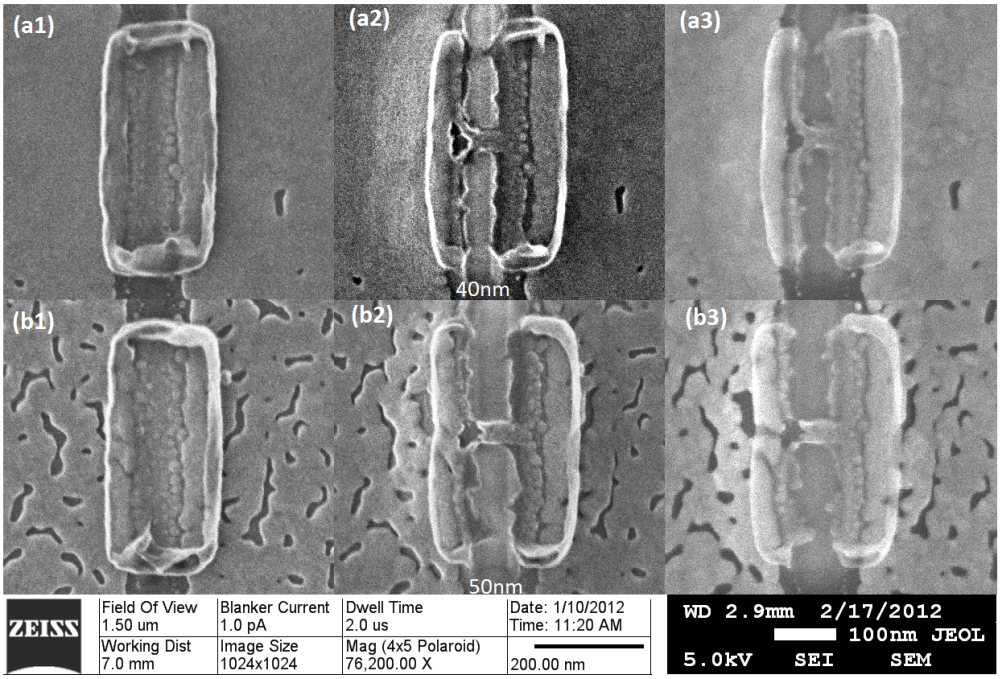

FIGURE 3.21: HIM micrographs of the devices before (a1, b1) and after (a2, b2) milling. The milling width for device a is 40 nm, for device b 50 nm. The center rectangle shaped pattern is the device made in to a 14 nm-thick Ni film, on top of two 10 nm-thick Au wires. From a2 and b2, it can be clearly seen that the substrate has swollen during milling, causing an expansion of the device on the surface. The bridge is broken because of the strain caused by substrate swelling. The milling dose was identical to that used for the device in Figure 3.20, 3.69×10^{18} ions/cm^2. (a3, b3) SEM micrographs of the same devices about one month after milling, which show no evidence of relaxation due to He out diffusion.

of 2×10^{21} atoms/cm^3 nano bubbles with diameter 1 to 3 nm will form in the amorphous region, and at 2×10^{22} atoms/cm^3 nano bubbles with diameter 1 to 30 nm will appear. Our doping concentration is between these two values as shown in Figure 3.22b. In Livengood's work, the implantation area is much larger than the depth. In our work, the milling width is small, compared to the length (about 500 nm) and implantation depth (about 300 nm), and therefore the expansion can be considered to be limited to the direction along the width of the device. We would hence expect a linear dependence of expansion in the direction of the width of the Ni pads with the milling width. This is indeed borne out by the measurements as displayed in Figure 3.22a with a linear fit through the data. The slope of the fit α can tentatively be used to extract the pressure of the He bubbles

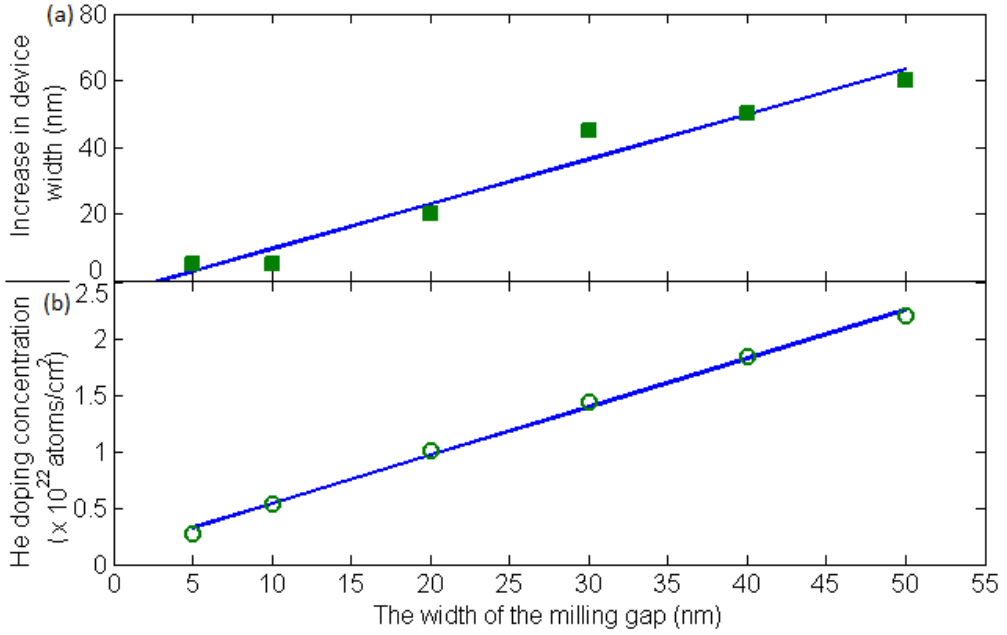

FIGURE 3.22: (a) plot of the increase in device width vs. the milling width. The size is measured from the HIM micrographs shown in Figure 3.20 and 3.21. The green filled squares show the values measured from the HIM image of the devices. The blue line is the linear fit of the experiment points. The off set on the horizontal axis is 3 nm. (b) Plot of the doping concentration vs. the milling width. The green empty circles show the doping concentration calculated with SRIM simulation according to each milling width. The blue line is the linear fit to the calculated data.

as derived from the ideal gas law displayed in Eq. 3.6.

$$P = \frac{RTD_{ion}}{d\alpha} \tag{3.6}$$

where P is the pressure of He bubbles, R is the gas constant, T is the temperature, D_{ion} is the HIM milling dose, and d is the depth of the doped region whose value is 250 nm from SRIM simulation. A pressure of 0.44 GPa is derived in this way The He pressure of 0.44 GPa is very small with respect to the Young's modulus of amorphous silicon 89 GPa [83], indicating that the Si is displaced towards to top surface and stressed for microns along the x-direction, much larger than the device area.

An upper limitation of a 20 nm gap with a 20 nm bridge can be defined for this method on this particular device, above which sub-surface swelling is likely to cause failure of the device. Within this limitation the strain has to be carefully considered, especially in DWMR H-shaped structures, for which strain in the bridge is likely to have a significant influence on the magnetic behaviour. It may be

possible to minimise the strain effect by fabricating the device on a thin membrane so that the ions are not trapped in the substrate. For example, Scipioni *et.al.* [84] milled a 50×50 nm^2 hole through a 100 nm thick suspended Au foil using the HIM method with little shape change in the surrounding material. On the other hand, control of the strain introduced by the helium milling could be useful in tuning the properties of the device, but this requires further investigation.

3.7 Conclusion

Functional single domain wall magnetoresistance spin-valves have been fabricated via e-beam lithography and helium ion beam milling. A 5-layered structure is designed to connect from a sub-100 nm, 14 nm thick spin-valve to a 200 μm, 300 nm thick probing pad. A combination of photolithography and e-beam lithography not only largely reduces the e-beam exposure time but also simplifies the proximity effect correction. A checkerboard dose sensor has been developed to detect the base dose of any type of e-beam resist. The minimum resolution of e-beam lithography PMMA + MMA bi-layer lift-off is about 10 nm for the gap without a bridge and 60 nm gap with the bridge. Helium ion beam milling is used to create patterns below 20 nm. The milling efficiency for Ni is measured to be 0.044 atoms/ion. A resistance to milling depth model is invented to detect the milling depth at a resolution of 2 nm in a sub-20 nm wide gap which is impossible for AMR or cross-sectional SEM. The substrate swelling effect limits the pattern width of helium ion beam milling to below 20 nm region. Helium nano-bubbles appear in the substrate when the concentration of implanted He atoms reaches 2×10^{21} atoms/cm^3.

Chapter 4

Magnetoresistance in domain wall spin-valves

4.1 Resistivity of wires

The resistance was measured by an Agilent B1500 semiconductor parameter analyser and Lakeshore EMTTP4 probe station at room temperature. Figure 4.1 shows the 4-point measurement setup. For two point measurement the result value contains the resistance of the probes, contact and gold wires. In four point measurement the resistance of the those parts (red parts in Figure 4.1(b)) can be neglected as long as we ignore noise sources. The details of the analyses are introduced below.

The resistance R of the gold wire is mainly determined by the geometrical size of the wires. It can be calculated by resistivity ρ of gold and the fabrication parameters. There are two types of gold wires in the pattern layout. In Figure 4.2 each wire between A_1(or A_2, B_1, B_2) and chip center (bottom left in the figure) is one point of the four-point measurement. The resistance of the wires can be calculated by adding up the separated parts L_1 and L_2. L_1 is rectangle while L_2 is assumed to be trapezoid and can be calculated by Equation 4.1. The resistivity of the thin film is larger than the bulk due to the thin film electron mean free path reduction, surface scattering and grain-boundary scattering [85]. Therefore a scattering enhancement parameter f is used to describe the resistivity of thin film $f\rho$.

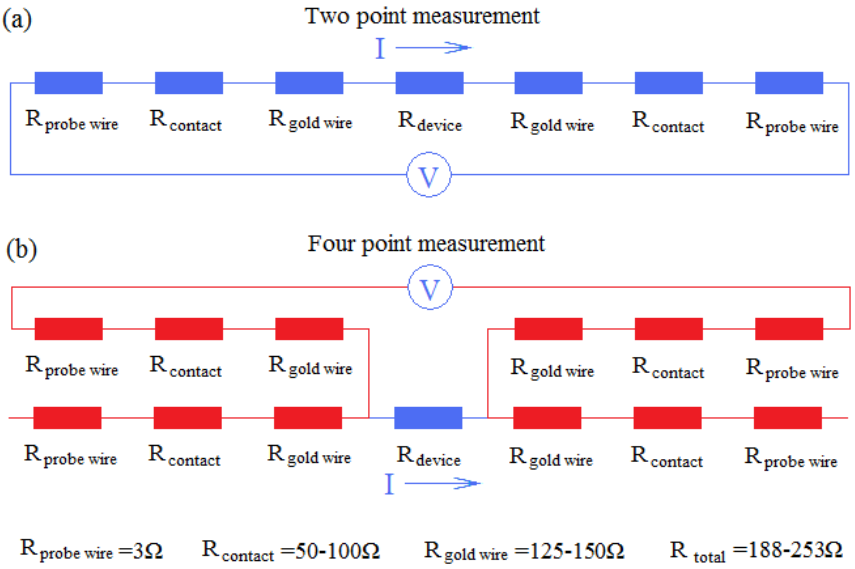

FIGURE 4.1: Schematic diagram of four-probe measurement comparing with two-probe measurement. The blue part is the resistance measured by the voltmeter.

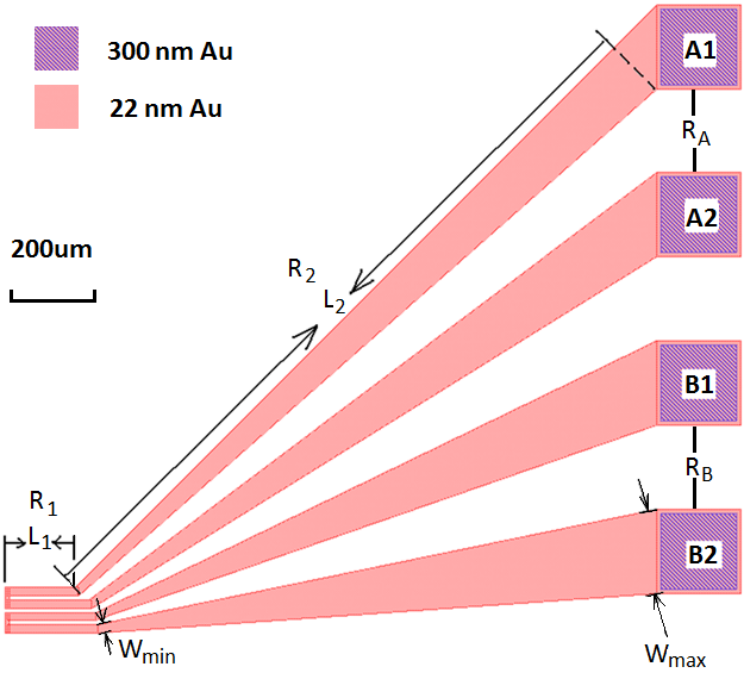

FIGURE 4.2: Schematic diagram of the testing gold wires. The resistance of one probe is calculated by adding up the resistance of L_1 and L_2's together, $R_{A_1} = R_{A_1L_1} + R_{A_1L_2}$. The resistance between two pads is calculated by adding up two probes', $R_A = R_{A_1} + R_{A_2}$

The 22 nm thin gold film resistance is calculated by,

$$R_2 = \int_0^{L_2} \frac{f\rho dL}{T(\frac{(W_{max}-W_{min})}{L_2}L + W_{min})} = \frac{f\rho L_2}{T(W_{max} - W_{min})} \ln\left|\frac{W_{max}}{W_{min}}\right| \tag{4.1}$$

where ρ is the resistivity of gold, L is the length of the gold wire, T is the thickness of the film, W is the width of the gold wire and f is the scattering enhancement due to the thin film effect.

There are mainly two types of gold wires in our experiment as shown in Figure 4.2. Table 4.1 shows the measurement results of resistance of these gold wires. The resistance was measured by a four point measurement setup. We use two terminal of B1500 semiconductor analyser to drive a constant current from Pad A1 to A2 (or B1 to B2) and monitor the voltage with the other two terminal. The sampled positions 1-4 are from the center to edge on a 6-inch wafer. The resistivity of the 22 nm thick Au film are roughly 4 times of the bulk, which agrees with the scaling and interface scattering model described by Sambles *et al* [85]. The scattering factor of Ni film is measured to be 11.6 in a 14 nm thick film (reported to be 7.6 in 20 nm thick film by Gonzalez [28]).

TABLE 4.1: Resistance measurement result

Position	R_A Ω	$R_{(B)}$ Ω	f_A	f_B
1	298.43	247.75	4.0	4.1
2	303.78	251.59	4.1	4.2
3	309.71	256.67	4.2	4.3
4	318.56	263.92	4.3	4.4
Average	307.62	254.98	4.15	4.25

The shape of Au wire A and B are shown in Figure 4.2

The contact resistance between probe and contact pads may change between 10 Ω and 1 kΩ. In our experiment a measurement is stable when the contact resistance is below 50 Ω. The contact resistance can be tested immediately before magnetoresistance measurement after putting 4 probes on the pads. All probes need to be connected together to free static charge, as the static charge could blow off the bridge.

4.2 Domain wall magnetoresistance measurement

4.2.1 Device fabricated by e-beam lithography

The resistance was sampled while sweeping the external magnetic field from −100 mT to 100 mT at the speed of 20 mT/min. The B1500 semiconductor analyser was set to sampling mode and 1 data point per second. The data was integrated during 1 second to average high frequency noise. The device made by only e-beam lithography and its $R - \mu_0 H$ curve is shown in Figures 4.3 and 4.4 respectively.

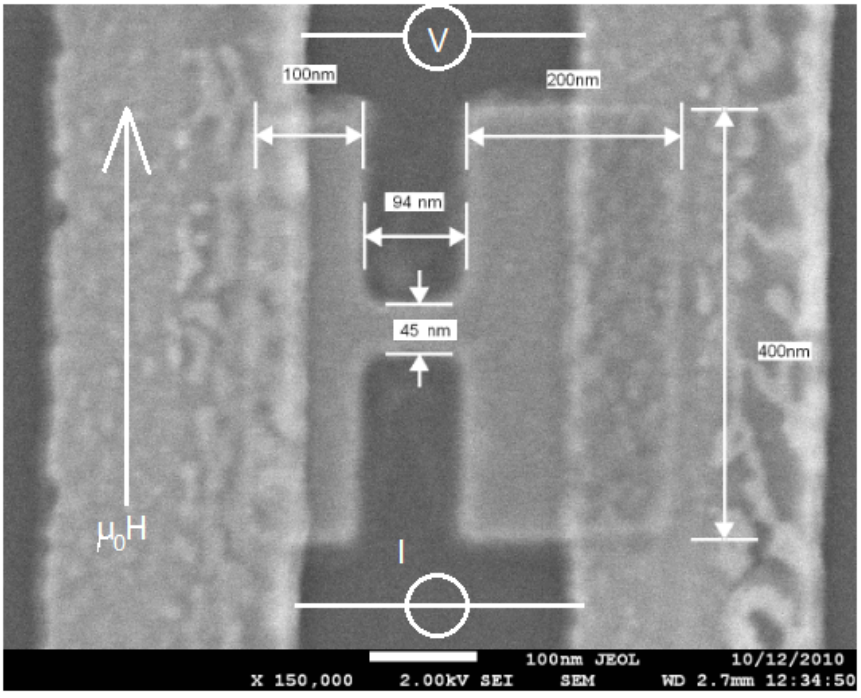

FIGURE 4.3: SEM micrograph of a DWMR spin-valve with a bridge length 94 nm. The H-shaped Ni device is sitting on two Au wires connected to 4 probing pads to allow 4-point measurement. The current source and voltmeter shows the measurement setup and $\mu_0 H$ indicates the orientation of external magnetic field

In the figure the bridge length is 94 nm and bridge width 45 nm. The high coercive side (100 nm × 400 nm) switches at about +25 and -30 mT whereas the low coercive side (200 nm × 400 nm) switches at ±5 mT. The asymmetry of the switching of the high coercive side could be caused by pinned grains on the edge of the Ni film. The magnetoresistance curve was measured at room temperature and ΔR is about 0.4 Ω. The magnetic field data was not collected at the same time when sampling the voltage signal. It was controlled by the magnetic field generator and sweeping was assumed at a constant speed. This could be another reason why the

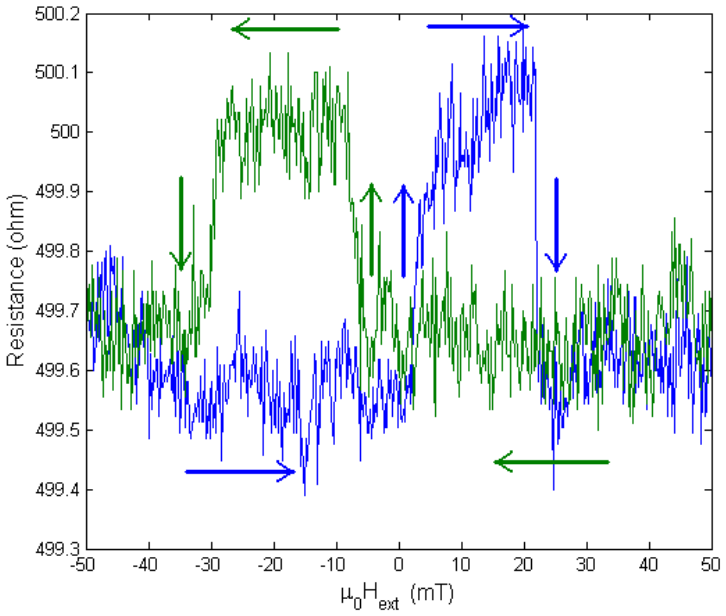

FIGURE 4.4: plot of $R - \mu_0 H$ curve of the device (Figure 4.3) at room temperature. The high coercive (100 nm wide) pad switches at about ±25 mT and the low coercive (200 nm wide) pad switches at about ±5 mT. The ΔR is about 0.4Ω. The arrows indicate the order of data collection during measurement. The result comes from an average of six individual measurement results

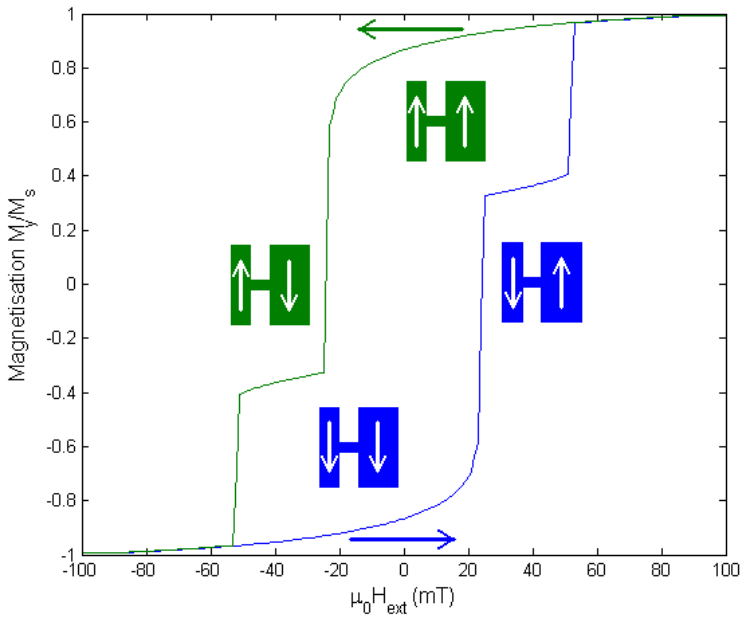

FIGURE 4.5: OOMMF magnetisation-magnetic field hysteresis loops. The model's geometrical size is based on the fabricated device (Figure 4.3). An exchange stiffness of $A = 9 \times 10^{-12}$ J/m and saturation magnetisation of $M_s = 490$ kA/m are used in this simulation. The curve shows both parallel and antiparallel states of our device

switching is asymmetric. An OOMMF simulation was done on the same geometrical size of the device to simulate the switching behaviour (Figure 4.5). The model's geometrical size is based on the fabricated device (Figure 4.3a). An exchange stiffness of $A = 9 \times 10^{-12}$ J/m and saturation magnetisation of $M_s = 490$ kA/m are used in this simulation. The curve shows both parallel and antiparallel states of our spin-valve. The measured switching field is different from the simulated field due to an antiferromagnetic Ni - O bond at the film surface [86]. The formation of NiO happens on any unprotected surfaces including top of the whole film, side of the bridge and domain pads and even the edge of grains in the film. The NiO could separate the grains and significantly increase the resistance of the film. This is the reason why the unprotected devices have a greater value of resistance than the protected ones. If the grains in the Ni thin film were separated, there would be no proper step-like curve in the MR measurement, because the switching of the pads is completely unknown in randomly distributed grains.

4.2.2 Device fabricated by HIM

The bridge of the device can be fabricated by helium ion beam milling instead of EBL (Figure 4.6). The H-shaped DWMR spin-valve is sitting on two gold wires connecting to 4 probing pads to allow 4-point measurement. The gold film is too thin to form a continuous film but still conductive. The Ni device was made by EBL and metal lift-off followed by helium ion beam milling. The bridge length and width in the pattern image are both 20 nm. Due to the swelling of the substrate and substrate drift (details see HIM section in fabrication chapter), the device came out with bridge length of 32 nm and width of 13 nm. The DWMR behaviour could be found in Figure 4.7.

In Figure 4.7 it can be seen that the high coercive (143 nm wide) pad switches at about +40 mT and −50 mT and the low coercive (169 nm wide) pad switches at about ±10 mT. ΔR is about 0.6 Ω at one peak and 0.5 Ω at the other. The step like curve is not very symmetric, however it shows a clear distinction between parallel and antiparallel state. The arrows indicate the order of data collection during measurement. The integrated sampling time was increased to 2 seconds to obtain a more stable measurement.

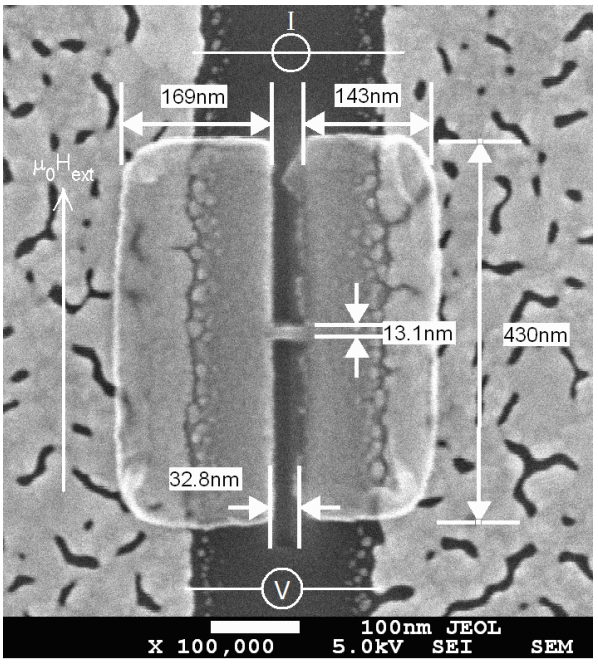

FIGURE 4.6: SEM image of the DWMR device with a bridge length 32 nm. The H-shaped DWMR device is sitting on two gold wires connecting to 4 probing pads to allow 4-point measurement. The gold film is too thin to form a film but still conductive. The Ni device was made by EBL and helium ion beam milling. The designed bridge length and width are both 20 nm. Due to the swelling of the substrate and substrate drift, the device came out with bridge length 32 nm and width 13 nm

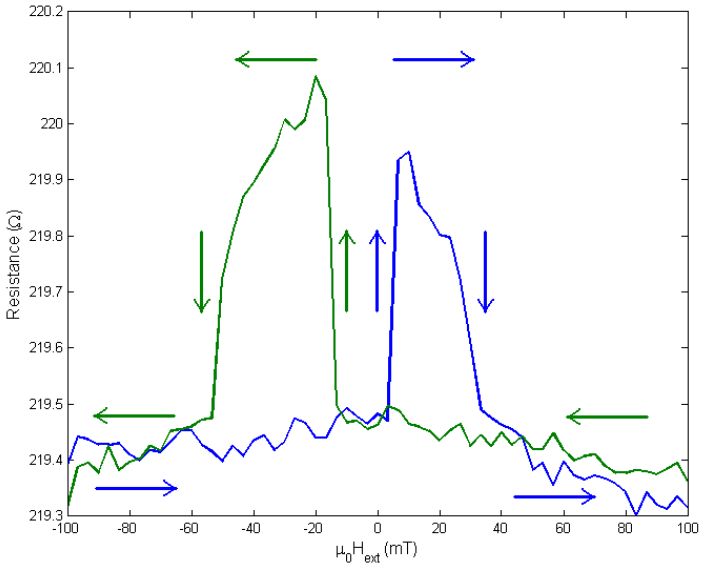

FIGURE 4.7: R-μ_0H curve of the device (Figure 4.6) at room temperature. The high coercive (143 nm wide) pad switches at about +40 mT and −50 mT and the low coercive (169 nm wide) pad switches at about ±10 mT. The ΔR is about 0.5 Ω. The arrows indicate the order of data collection during measurement. The result comes from an average of three individual measurement results

4.2.3 Comparison between e-beam lithography and HIM devices

The bridge length and width of the device made by HIM is smaller than the one made by EBL. The domain wall width of the devices can be calculated by the magnetisation rotating area via Bruno's equation (Equation 2.12). In our experiment the magnetisation was simulated by OOMMF software based on the device's geometrical size. The magnetisation distribution of the device just before and after the appearance of the domain wall is shown in Figure 4.8. The domain wall width can be calculated from the magnetisation distribution by using the Equation 4.2 which is another format of the original Bruno's equation. The calculated domain wall width of the spin-valve made by e-beam lithography only is 93.9 nm whereas by He ion beam milling is 58.7 nm. The domain wall width decreases when bridge length becomes shorter. We have 3 devices made by e-beam lithography showing the DWMR step-like curve and they show similar resistance value of 0.4 Ω. Their calculated domain wall widths are all around 95 nm.

The equation to calculate the domain wall width (Equation 2.12) is written as,

$$W_{dw} = 4\left[\sum_{i=0}^{w/w_0} \frac{(\theta_{i+1}-\theta_i)^2}{w_0}\right]^{-1} \tag{4.2}$$

where W_{dw} is the domain wall width; w is the length of the device at the line across the bridge; w_0 is the distance between two neighbour spins; $\theta_{i+1} - \theta_i$ is the angle between spin direction and magnetisation of two neighbour spins whose distance is w_0 in the OOMMF simulation.

We expect a difference in DWMR of spin-valves with different domain wall width. However, in our experiment, this was 0.4 Ω for the EBL device, similar to the HIM device of 0.5 Ω. They show both positive magnetoresistance. The switching behaviour of these two devices is similar, as the antiparallel state gives high resistance.

The device made by HIM has a big strain inside the bridge as we discussed in Section 3.6.3. The influence of the strain to magnetisation is that the magnetoelastic energy caused by the strain forces the magnetisation to follow the strain direction. In this case the domain wall width becomes longer than the unstrained one. This could be another reason why the DWMR ratio does not increase as expected when the bridge length is reduced to 30 nm. The analytical explanation of this point is discussed in Section 4.5.

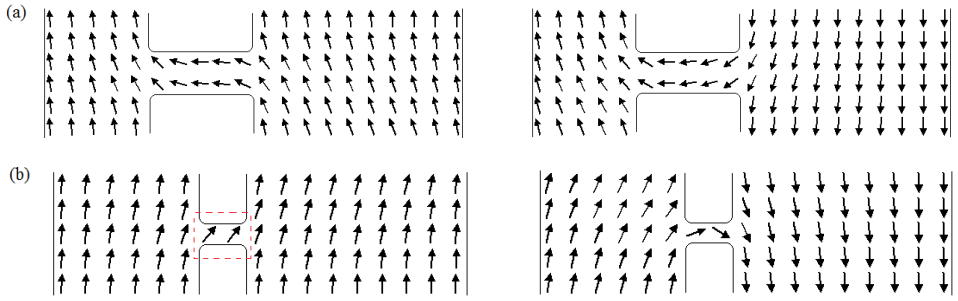

FIGURE 4.8: (a) The simulation results of switching the device with a bridge length of 94 nm. (b) The simulation results of switching the device with a bridge length of 32 nm. The simulation software used was OOMMF, parameters were based on the fabricated spin-valve shown in Figures 4.3 and 4.6. The left side shows the parallel state and there is no domain wall in the bridge. The right side shows the antiparallel state and domain wall appears in the bridge

4.2.4 OOMMF simulation comparison between fabricated and ideal geometries

The magnetisation distribution simulation was carried out by OOMMF version 1.1b2 (1.1.1.2) loaded by Tcl 8.4.5.0 Tk 8.4 platform installed in Windows XP 2002 SP2. The 2-D shape of the device was taken from the SEM pictures of the E-beam and HIM.

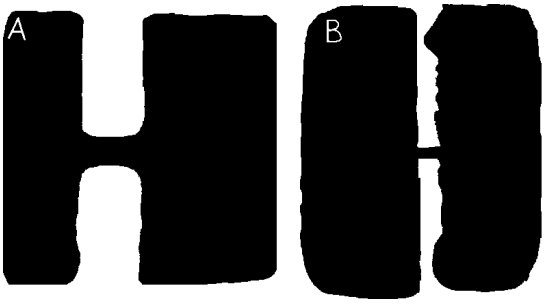

FIGURE 4.9: OOMMF simulation input file for E-beam lithography sample (a) and Helium ion beam milled sample (b). BMP mask files for simulation are included in CD

The simulation setting is listed in Table 4.2. OOMMF is a 3-D simulator but only takes a 2-D masks. Figure 4.9 shows the input masks we used in our simulation, which were taken from the SEM images of the measured devices. The cell size of the simulation was chosen as 5 nm for the E-beam only spin-valve and 4 nm for the HIM milled sample. It is not necessary to go below these values because it increases the simulation time significantly. However the cell size above 5 nm is not

acceptable as well because it loses some of the short distance exchange interaction [28].

TABLE 4.2: OOMMF simulation setting

	M_s A/m	A J/m	K_1 J/m^3	Height nm	Width nm	Thickness nm	cell size nm
Electron beam	4.9e5	9e-12	-5.7e3	400	400	20	5
He ion beam	4.9e5	9e-12	-5.7e3	430	360	14	4

*.mif file included in the CD

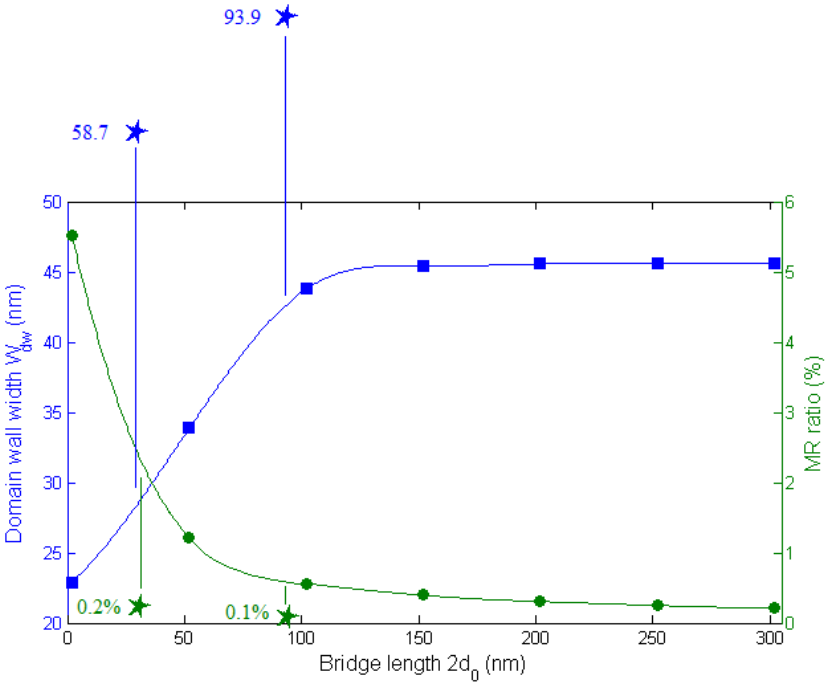

FIGURE 4.10: Plot of domain wall width (left hand side curve blue) domain wall magnetoresistance ratio (right hand side curve green) as a function of bridge length. Blue squares are the domain wall width based on ideal structure with right angles at all the corners whereas blue stars are the domain wall width based on SEM picture of the fabricated samples with round corners. Greed dots are the domain wall magnetoresistance ratio calculated from the ideal samples whereas the greed stars are the same ratio measured from real devices. The device with a bridge length 94 nm was fabricated by e-beam lithography only. The device with a bridge length of 32 nm was fabricated by e-beam lithography followed by Helium ion beam milling. Blue stars show their simulated domain wall width based on the real geometric shapes (Figure 4.9). Green stars show their measured domain wall magnetoresistance ratio.

From the magnetisation distribution results we can calculate the domain wall width through Equation 2.12. The domain wall width based on the ideal structure with right angled corners is 43 nm for the e-beam sample and 28 nm for the He ion beam sample according to the simulation results reported by Fangohr *et al*

at 2008 [30] (Shown as blue curve in Figure 4.10). However the domain wall width based on the fabricated structure with round corners using the same equation is 94 nm for the e-beam sample and 59 nm for the He ion beam milled sample. The difference of domain wall width between round corner and right angled corner is about a factor of 2. Knittel *et al* [87] have reported that a small rounding reduces the coercivity by about a of factor 2 by using Nmag (a magnetisation simulator developed by Fangohr's group at School of Engineering University of Southampton). It can be seen that both results have good agreement that the domain's coercivity is reduced by the rounded corner as well as the constriction of the domain wall is waken at the same time. Therefore the domain wall width increases accordingly, which leads to the reduction of magnetoresistance ratio shown as green stars in Figure 4.10. In theory sharp corners could give better performance to our spin-valves. However the real devices always contain a round corner, which could be one reason why the measured magnetoresistance ratio is lower than the predicted.

There could be several reasons why the DWMR is lower than the estimated values. The green stars in Figure 4.10 are lower than the simulated curve. Firstly the quality of Ni film is not as good as the ideal case that the spin diffusion length λ_F and spin polarisation rate P could be smaller than theory value. There are grains in the evaporated Ni film, NiO on the unprotected edges and rough edge caused by lift-off process. According to Equation 2.31 which is what we used to estimate the result, the reduced P and λ_F largely reduces the DWMR ratio. Secondly, the round corners reduces the coercive of the domain pads, therefore the domain wall width increases accordingly. Thirdly the measurement current density was too high that the bridge was heated up during measurement, which increases the thermal influence to the electron spins in the bridge leading to the reduction of the of λ_F and P. The influence caused by current density and NiO will be explained in detail at the following Section 4.5.

4.3 Anisotropy magnetoresistance discussion

The domain wall magnetoresistance is different from anisotropy magnetoresistance. In our experiment the measurement results was mainly from the DWMR effect instead of AMR. The advantage of our spin-valve to prove the existence of DWMR is that there is only a single domain inside each pad, and a single domain wall inside the bridge. It is easier to analyse the physics by looking at a single effect instead of superposed ones.

A head to head wire DWMR structure was reported by Haug *et al* in 2009 [8]. Their domain wall was a head to head 180° domain wall. The high coercive side is 500 nm wide, the low coercive side is 1.2 μm wide. The neck width is 30 nm. The measured magnetoresistance ratio is about 0.06% according to their *in situ* (measured inside Lorentz) measurement result. Compared to our device, the line-shaped domain pads are much larger, so the domain wall inside the bridge may not be single. The resistance change in their magnetoresistance curve may be caused by vortex wall or multi walls. In line-shaped devices, the magnetoresistance effect is relatively small because the classic resistance of domain pad hides the DWMR effect. Their negative magnetoresistance may come from the AMR effect, because in a parallel state the magnetisation inside the constriction area is parallel to the current whereas antiparallel state sees the magnetisation perpendicular to the current. According to the AMR effect, the resistance when the magnetisation is perpendicular to the current is smaller than when they are parallel.

Another example whose DWMR may be caused by AMR effect would be a 90° domain wall magnetoresistance reported by Montero *et al* in 2004 [14]. The domains of the device are deposited in different planes, with a nano constriction point in between. Since the PMMA and MMA is a soft polymer, the structure is not stable and the magnetoresistance behaviour disappeared in two days after being fabricated. The DWMR in this type of structure is also within the range of expected AMR generated effect.

To compare, our magnetoresistance can be proved not to be AMR effect, because the magnetisation inside the bridge always follows the bridge direction before or after the domain wall appearance. If it was due to AMR effect, the angle θ between bridge magnetisation and the current direction should have changed significantly before and after the domain wall appears. In practice, we can calculate the difference of the AMR caused by the appearance of the domain wall from Equation 2.19 as,

$$AMR = \frac{\Delta\rho_{_{AMR}}}{\rho_{av}} = \frac{\left(\rho_{//} - \rho_{\perp}\right)}{\rho_{av}} \left(\cos^2\theta_P - \cos^2\theta_{AP}\right) \tag{4.3}$$

where $\rho_{_{AMR}}$ is the resistivity of the Ni when considering AMR effect, and $\Delta\rho_{_{AMR}}$ is the resistivity change due to the AMR effect when the switchable domain pad switches. ρ_{av}, $\rho_{//}$ and $\rho_{\perp}$ is the average, high (parallel) and low (perpendicular) AMR resistivity respectively, θ_P and θ_{AP} are the angles between the current and magnetisation of our device at parallel state and anti-parallel state respectively.

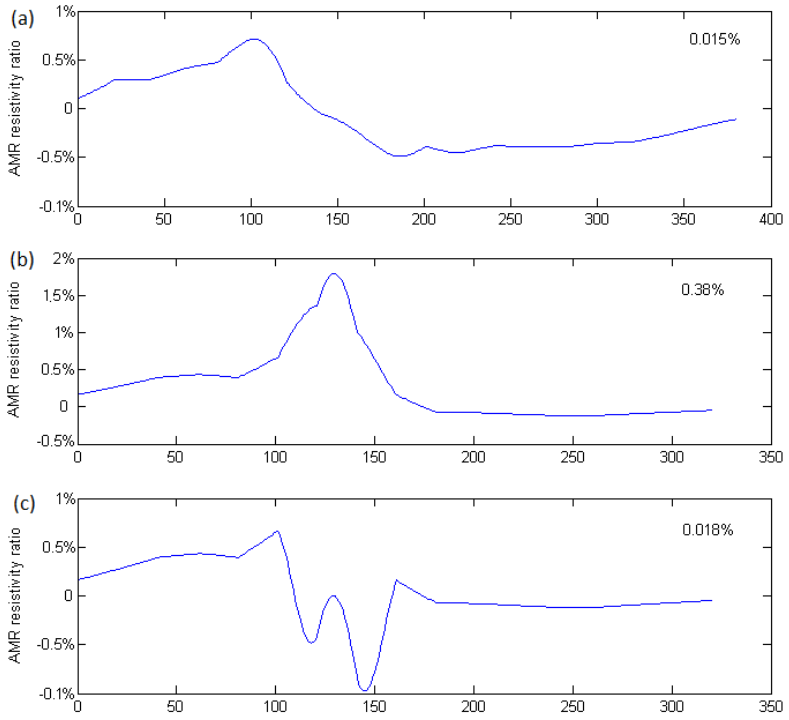

FIGURE 4.11: AMR resistivity ratio distribution across the device. (a) is calculated from the device with 100 nm bridge length, (b) is from 30 nm in ideal case, (c) is the 30 nm with strain inside the bridge. The percentage on the right top of each figure is the average resistivity change

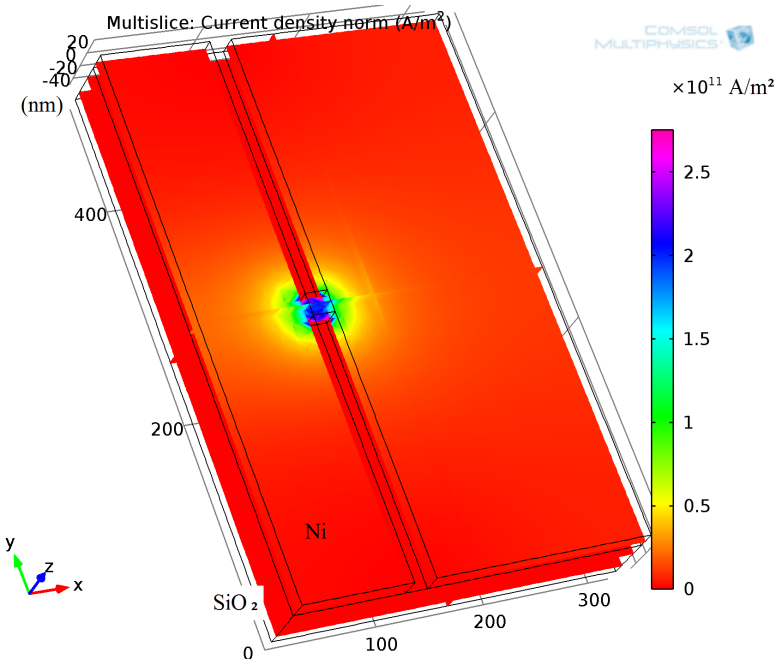

FIGURE 4.12: 3-D plot structural model of current density distribution simulated by COMSOL 4.2a. The simulation is based on the 32 nm long bridge HIM made device including the SiO_2 substrate.

With Equation 4.3, the resistivity changes at different positions (Figure 4.11) of the spin-valve, which can be calculated from the OOMMF magnetisation simulation (Figure 4.8). It can be seen that the resistance change caused by the AMR effect (0.02%) is significantly smaller than DWMR (0.2%). The average AMR was calculated by the resistivity ratio distribution (Figure 4.11) and current density (simulated via COMSOL 4.2a Figure 4.12) as shown,

$$AMR_{av} = \frac{\int_0^w AMR(x) \times R(x)dx}{R} \tag{4.4}$$

where w is the width of the spin-valve, AMR is the AMR ratio before and after the domain wall appears in the bridge, $AMR(x)$ is the same ratio of a dx wide area around position x, R is the resistance of the whole device and $R(x)$ is the resistance of a dx-wide part at the position x. Why the AMR effect in our spin-valve is so low can be explained by the magnetisation inside the bridge. In a long bridge no matter whether there is a domain wall in the bridge or not, the magnetisation inside the bridge follows the width direction. Therefore, there is almost no AMR effect for 94 nm long bridge. This agrees with what Ngo *et al* reported in 2011 [88]. However when the bridge length is decreased the exchange interaction forces the magnetisation to follow the domain's magnetisation direction which is perpendicular to the current in the parallel state. In anti-parallel state as the domain wall type is Néel-type [89] the magnetisation inside the bridge is always parallel to the current. In this case when switch happens the AMR gives an additional value to the magnetoresistance. This proves the magnetoresistance we found is DWMR but not AMR. When further scaling the constriction width of the H-shaped spin-valve the AMR will give a positive effect (up to 0.4% as shown in Figure 4.11(b)) to the total magnetoresistance, but at that size the DWMR could be expected to be as large as 2%. Therefore in our structure the DWMR is always the main contribution to the total magnetoresistance.

As a reference, the AMR was measured in a 185 nm long, 78 nm wide and 14 nm thick Ni nano-wire (Figure 4.13) fabricated in the same as our DWMR spin-valve. An external magnetic field was applied perpendicular to the nano-wire. The magnetoresistance measurement result is shown in Figure 4.14. At small field the magnetisation inside the nano-wire follows the wire direction and it is in high resistivity state. At large field the magnetisation inside the nano-wire is saturated perpendicular to the current therefore it is in low resistivity state. The AMR ratio of Ni thin film fabricated by e-beam lithography lift-off is about 0.6%.

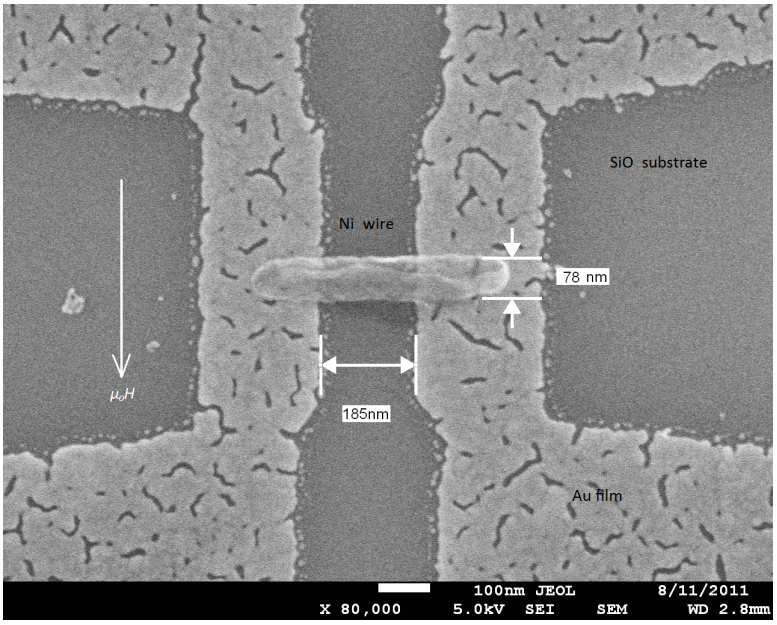

FIGURE 4.13: SEM micrograph of a piece of Ni nano wire. The length of Ni wire is 185 nm and width is 78.5 nm, where the resistance was measured by the 4-point measurement. A constant current was driven through the bridge from two terminals of the gold wires and the voltage was monitored at the other two ends.

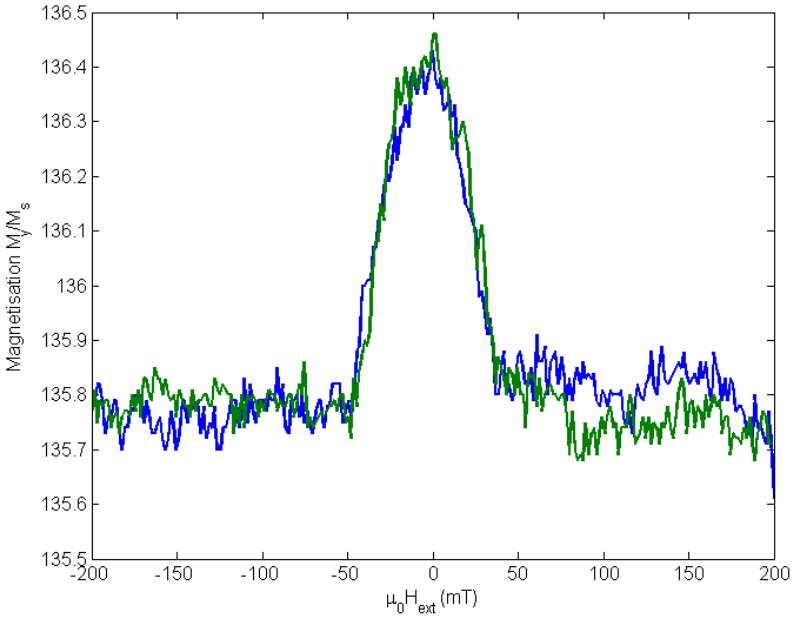

FIGURE 4.14: A plot of resistance against external magnetic field of the Ni nano wire shown in Figure 4.13. The external magnetic field was perpendicular to the nano wire and parallel to the substrate. The sweeping speed of the field was 20 mT/min, the value of resistance was sampled at a rate of 1 point per second

4.4 Measurement resolution and noise

The measurement of DWMR effect is influenced by numerous factors such as thermal noise, noise form magnetic field generator, the resolution of voltmeter, current source and environmental mechanical noise. The signal of domain wall magnetoresistance is about several μV in a 1 kΩ system. Any electric noise larger than 0.5 μV could hide small magnetoresistance. Due to the small size of the device, we cannot always increase current to get a good signal to noise ratio. The noise analyse is essential in this type of experiment.

The thermal noise $\bar{v}_{tn}$ in the system comes from the resistance of measurement cable, contact and gold wires. The value can be calculated by Equation 4.5. At room temperature and a sampling speed of 1 point per second, 1 kΩ's noise is about 4 nV. For a measurement current of 5 μA the signal (0.1% magnetoresistance ratio) to noise ratio is about 250 : 1. This noise can be reduced by reducing the resistance of gold wires, contact resistance (eg: wire bonding) or measurement temperature. This the reason why the gold wires' resistance is kept as low as possible during fabrication, even through they do not show up in 4-point measurement.

$$\bar{v}_{tn} = \sqrt{4k_B T R f} \tag{4.5}$$

where $\bar{v}_n$ is the voltage variation caused by thermal noise, k is Boltzmann's constant, T is temperature, R is the resistance of the wires and f is sampling frequency.

The noise from the magnetic field generator is mainly from the sweeping of the magnetic field. At an uniform speed, according to Maxwell - Faraday equation 4.6, there is a value shift in voltage measurement result. However if $\partial B^2/\partial^2 t$ is not zero, there is a noise in the whole circuit as shown in Equation 4.7.

$$\oint_C \vec{E} dl = \int_S \frac{\partial \vec{B}}{\partial t} dA \tag{4.6}$$

where C is the length of the circuit, $\vec{E}$ is the electric field, dl is an infinitesimal element of C, S is the area inside the close loop of C, $\vec{B}$ is the magnetic field, dA is an infinitesimal element of S. The magnetic noise is now given by,

$$\bar{v}_{mn} = \int_S \frac{\partial B^2}{\partial^2 t} dA \tag{4.7}$$

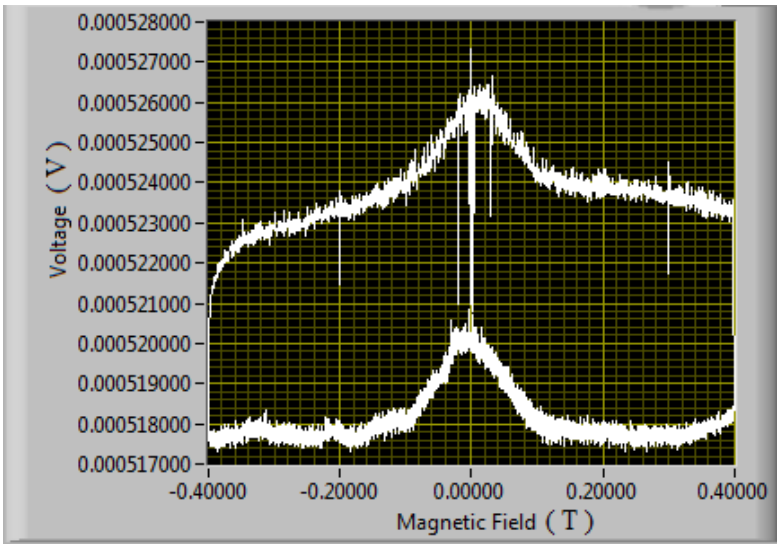

FIGURE 4.15: The magnetoresistance curve captured from the Labview window which controls the whole measurement system. The horizontal axes shows the magnetic field. The vertical axes is the voltage between two ends of a Ni nanowire. Each grid represents 20 mT and 200 nV.

This noise does not change with the power supply or measurement instrument in the circuit. It can be detected by comparing the measurement results with and without an external magnetic field. The gain setting of the magnetic field generator should be optimised in order to minimise this noise. Figure 4.15 shows the voltage sampling curve with different settings. The sweeping speed of the top curve was +20 mT/min and the bottom curve was −5 mT/min. The plus and minus shows the difference of field direction. The noise of about 500 nV exists in both curves. This value increases when the proportional gain value increases. A large signal is visible when the magnetic field switches direction. These peaks as large as 7 μV (in the middle of the top curve in Figure 4.15) can be reduced by decreasing the sweeping speed. The noise in the bottom curve of Figure 4.15 is the lowest that the optimised conditions can achieve in this system. When the magnetic field sweeping was switched off, the noise was about 50 nV, reduced by a factor of 10. This proves that the major noise was from the magnetic field generator during sweeping. If a current of 5 μA was used in the measurement, the signal (0.1% magnetoresistance) to noise is about 2 : 1. The magnetoresistance signal is almost invisible at this noise level. Therefore a large current (eg: 20 μA) is required to compensate the noise generated by sweeping the external magnetic field.

The measurement curve shown in Figure 4.15 was taken from the latest experimental setting with Keithley current source 6430 and nano voltmeter 2182. The

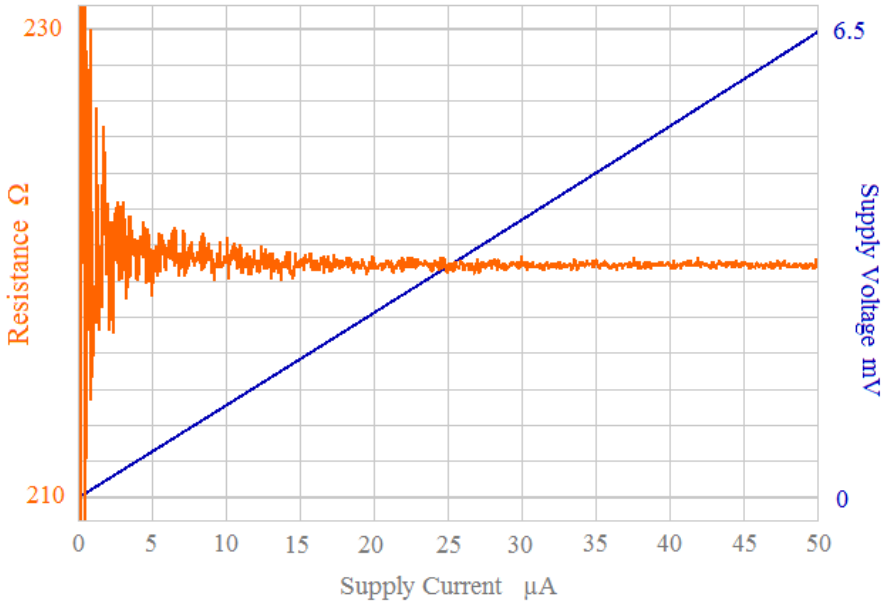

FIGURE 4.16: A plot of resistance of a spin-valve against measurement current. The left Y axis is the resistance of the device. The right Y axis is the supply voltage of the current source. The X axis is the current through the bridge of the spin-valve. The integration time for each measurement point was 0.1 s. It can be seen that the value of resistance variation, noise is reduced when current increases. The system's I-V curve shows that the whole circuit is ohmic.

resolution of the voltmeter is about 10 nV which is much better than the Agilent B1500's 500 nV. All the DWMR devices we mentioned in this report were measured by Agilent B1500, for we did not have a Keithley nano voltmeter at the time we measured the spin-valves. The variation caused by the voltmeter's resolution is about 500 nV. Adding to the noise caused by sweeping magnetic field, the total noise was 1 μV. This 1 μV total noise means that the current needs be increased to 50 μA to get 5 : 1 signal to noise ratio. A curve showing the relation between noise and current was measured by Agilent B1500 (Figure 4.16) at room temperature, without external magnetic field. From the curve we can see the noise level of supply current and voltage are both stable during the sweeping, only the noise of resistance measured by 4-point set up increase with the decrease of the measurement current. This is the reason why our devices were measured at 50 μA.

By replacing Agilent B1500 with a Keithley current source and voltmeter, the instrument variation can be reduced to 10 nV, but the magnetic generator's noise is still 500 nV. Another way we tried is to use a function generator (AC current source) and a lock-in amplifier to do AC measurement. This has been reported in many papers as an efficient way to remove noise. However, we found the system

we have could blow off any devices connected to the measurement circuit. The reason is still not known yet. These are the reasons why we cannot reduce the measurement current. The problem caused by the large current is mainly to cause the broken devices.

4.5 Failure analyse

Besides the successfully working devices there were a significant number of failures in experiments. Some of the fabrication could not be processed due to the limitation of the instruments and materials involved. For example the Ni evaporation was done at room temperature instead of high temperature. The drawback of this method is that there may be many grains in the film due to the lack of energy for Ni atoms to relocate. However in the lift-off process there is photo (or e-beam) resist on top of the substrate. It becomes hard if the substrate is being heated during evaporation and will be very difficult to remove. The annealing could be done after lift-off but needs much higher temperature than during the evaporation. However all the furnaces in our cleanroom are bought for semiconductor development purpose but not allowed to process metal contaminated samples especially Au contained samples. So we do not have chance to do this unless we build our own furnace in the future.

The formation of NiO on the unprotected Ni film surface(or side wall) could influence the switching behaviour. The room temperature grown Ni film contains grains due to the lack of energy for Ni atoms to relocate. We can use 1-2 nm Au film to protect the top surface of the Ni film. However the side wall of the device is still exposed to the air which oxidise the outer layer of Ni. If the grains are separated by NiO, the switching behaviour will not be predicable. Therefore no step-like DWMR shows up during measurement. For the device level circuit a non-conducting capping layer can be used after lift-off process, but the devices need be kept in dry N_2 all the time during processes, which is not possible in our cleanroom.

Some of the measurement could not be carried out due to the lack of protection of the device against being blown off. For example, in the EMTTP4 magnetic cryogenic probe system the substrate supports the angular dependent measurement which was not carried out in this experiment. The difficulty was that to rotate the sample holder we need lift up the probes and put them down afterwards. Each time when we put the probe on the pad there is a risk that the sample being

blown off. This process definitely needs wire bonding. The sample problem exists in the wire bonding process that once the pin touches a pad the bridge is blown off immediately. The cryogenic measurement which was not carried out needs wire bonding as well, because when the sample's temperature is decreasing the probe scratches pads because the pads are contracting with cold. The measurement is very sensitive to the quality of contact that people closing doors will result in spikes in measurements or even blowing off the bridge. The same lift-up and put down procedures exist in the cooling down process. One solution could be that shorting all 4 pads with gold wires at the beginning and brake then with FIB (focus ion beam) after wire bonding.

The measurement current was to too high that 70% of device did not show any magnetoresistance signal. According to the Comsol simulation (Fiture 4.12) the current density in the bridge could be as high as $2 \times 10^{12}\mathrm{A/m^2}$. Fangohr *et al* at 2011 [90] reported that in a nano wire constriction whose cross section area is 20 nm $\times$ 20 nm, a $10^{12}\mathrm{A/m^2}$ current could generate over 1000 K temperature by passing a current pulse over 15 ns. This is over the Curie temperature of Ni. Therefore the bridge may become non-magnetic because of this heat. Secondly the spin torque effect could couple two domains together when the current density is very large. As we discussed in Section 2.5 (Figure 2.21 [61]), a magnetic domain can be switched by the current from the other side of a domain wall. In our device, when the current flows from high coercive side to low coercive pad, the low coercive pad will not switch untill the reversed field passes the point which switches the high coercive pad. In this case the domain wall does not appear during the whole external field sweeping. When the current flows from low coercive to high coercive pad, both pads switch together when the field passes the low coercive point. Even if the two pads are not completely coupled, the spin torque caused by the large current reduces the width of high resistane step in the DWMR curve. As we discussed in the previous section, the DC current cannot be reduced anymore due to the noise in our system. A solution could be using AC current source and lock-in amplifier to measure the resistance. However, our lock-in amplifier blowed off any devices once put the probe down on the pad.

It's better to measure the magnetisation directly inside the film during sweeping the external magnetic field. This requires Lorenz TEM or spin polarized SEM, which we do not have in the cleanroom. We looked at the magnetisation inside the spin-valve indirectly by OOMMF simulation and magnetoresistance curve. This is also the reason why a single domain wall device is better than multiple domain walls. Especially when there is not enough space for the second domain wall to

show up, we can say the step-like resistance increase is due to the only domain wall inside the bridge.

4.6 DWMR Theory

The domain wall magnetoresistance can be also explained by an energy model. The domain wall appears in the bridge when the low coercive pad switches before the high coercive one. During this process the magnetisation direction inside the wide pad inverts about 180°. This increases the Zeeman energy of the spin polarised conducting electrons. We assume all additional energy due to the switching comes from the power supply. The free electron spins in magnetised material such as Ni

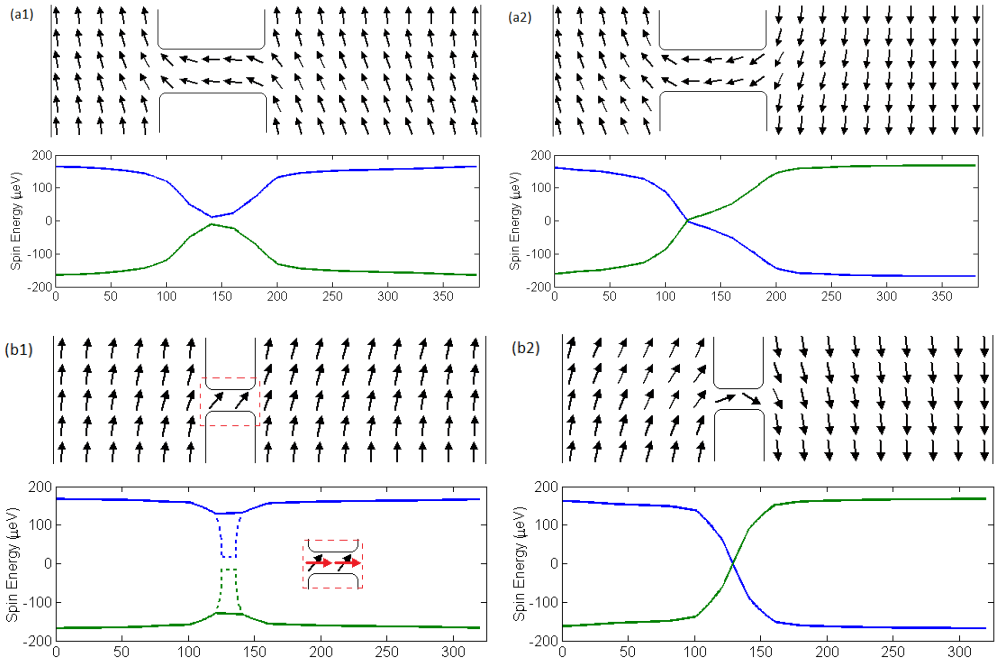

FIGURE 4.17: The energy distribution of the spin down (blue lines) and spin up (green lines) of the device with a bridge length of 100 nm in parallel state (a1) and antiparallel state (a2), with a bridge length of 30 nm in parallel state (b1) and antiparallel state (b2). The black arrows indicate magnetization directions simulated by OOMMF inside the spin valve before and after switching. In Figure (b1) the black arrows show the simulated result without considering the influence of strain inside the bridge. The red arrows in the bridge shows the magnetization under the influence of strain. The dashed curve shows the energy distribution corresponding this influence.

thin film are not randomly distributed as in non-magnetic materials. The reason is that electron spins with the same magnetic orientation as the magnetization

direction have a lower energy (Figure 4.17). The energy difference between spin up and down can be calculated by,

$$E = -\mu_0 \vec{m} \bullet \vec{M} = -\mu M_S^2 cos\theta \tag{4.8}$$

where E is the energy density; $\vec{m}$ is the magnetic moment of the unpaired 3d8 electrons of Ni atom; $\vec{M}$ is the magnetisation of Ni; θ is the angle between the electron spin and magnetisation. M_s is the saturation magnetisation of Ni ($M_s = 4.5 \times 10^5$ A/m); μ is the permeability of Ni (μ is said to be 100 to 600 times μ_0 [91]). The energy density of the spins antiparallel to the magnetisation is 2.54469×10^7 J/m^3 or 168 μeV/atom ($\rho_{Ni} = 8.908$ g/cm^3, $A_r = 58.6$ g/mol, 1 mol contains 6.02214×10^{23} atoms). The energy density distribution inside the domain and domain wall can be calculated from OOMMF simulation results using Equation 4.8. Figure 4.17 shows the energy distribution of spin up and down in the spin-valve with bridge length 100 nm, at parallel (a1) and anti-parallel (a2) state. The magnetisation of the two states were taken from OOMMF simulation whose parameters were based on measured spin-valves. Figures 4.17(b1, b2) show the same simulation results from the spin-valve with a bridge length of 30 nm. In theory, when the bridge length is scaled down to 30 nm, at parallel state, the magnetisation direction inside the bridge would follow the domains' because of the exchange interaction. However, in our experiment we use helium ion beam milling to create the bridge structure so there is large strain inside the bridge which forces the magnetisation to follow the bridge direction. This is because the magnetoelastic interaction (Equation 2.10) exceeds the exchange interaction (Equation 2.2). In this case the energy distribution is as shown in Figure 4.17(b1) dashed lines. This influences the result as a negative impact on DWMR ratio. The explanation is given in the following discussions.

The voltage increase at constant current, ΔV (measured directly by the voltage meter in the 4-point measurement) due to the appearance of a domain wall can be represented by,

$$\Delta V I = \Delta P n_e v_e A_{cross} E_{gap} \tag{4.9}$$

where ΔP is the change in average spin polarisation where scattering occurs at antiparallel state. n_e is the free electron concentration in Ni film. v_e is the velocity of the electrons travelling from the bridge to the switchable pad. A_{cross} is the cross-section area of the Ni bridge. E_{gap} is the energy difference between spin up and spin down state, which is 2 times the of value $|E|$ (Equation 4.8). ΔV

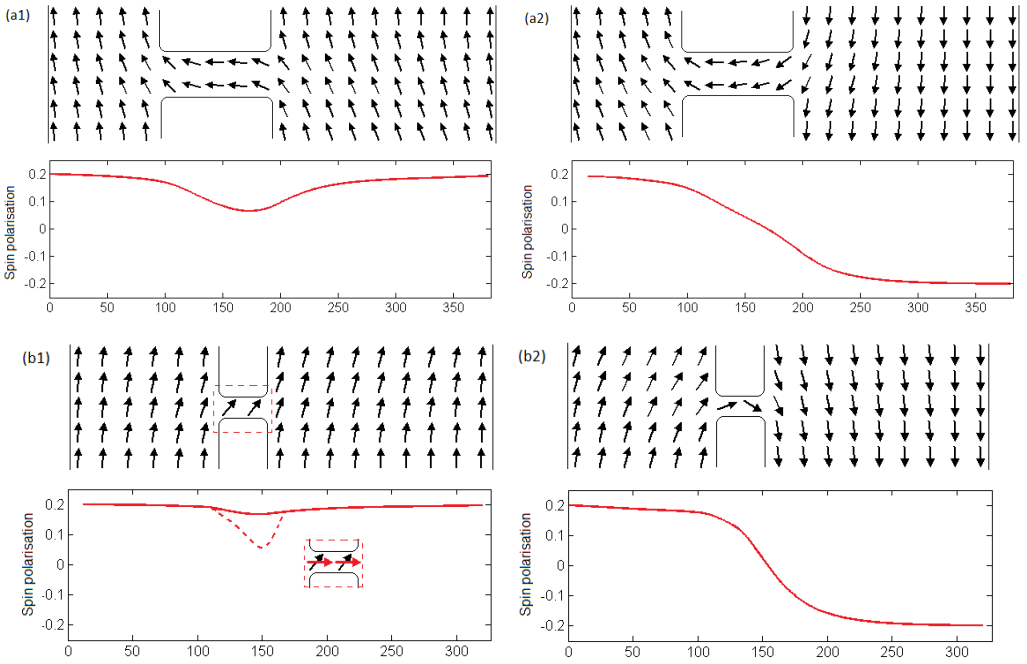

FIGURE 4.18: Spin polarisation distribution of the device with 100 nm long bridge at parallel (a1) and antiparallel (a2) states and the device with 30 nm long bridge at parallel (b1) and antiparallel (a2) states. The spin polarisation is defined as $P = \frac{P_\uparrow - P_\downarrow}{P_\uparrow + P_\downarrow}$. In Figure (b2) the solid line shows the simulated result without considering the influence of strain inside the bridge. The dashed curve shows the spin polarisation corresponding to this influence

is the voltage increase caused by the switching of the spin-valve from parallel to antiparallel state. I is a constant current supply during the measurement. The left side of Equation 4.9 is additional power consumption at the current source to keep the constant current when domain wall appears. We assume the energy cost of spins of passing through the domain wall is completely from the additional energy consumption of the current source when domain wall appears. Thus the right side is the required energy of polarized conducting electrons when passing through the domain wall. If the equation $I = q_e n_e v_e A_{cross}$ is put in Equation 4.9, the resulting equation is Equation 4.10,

$$\Delta V = \Delta P E_{gap} / q_e \tag{4.10}$$

where ΔP and E_{gap} are the same as in Equation 4.9 and q_e is the electric charge of an electron, 1.602×10^{-19} C. Equation 4.10 shows that when the device switches from the parallel to anti-parallel state, a percentage of ΔP electrons enter a higher energy state. When we keep a constant measurement current, the additional energy comes from the increase of the voltage supply. The value ΔP can be calculated

by the spin accumulation model introduced in Section 2.5 (Equation 2.29),

$$P(l) = P_0 e^{-\frac{l}{\lambda}} \tag{4.11}$$

where P is the spin polarisation at a distance l in a non-magnetised region. P_0 is the spin polarisation in the magnetised region. λ is the spin diffusion length. An exponential model is used because the spins lose their orientation in a diffusion way. From this exponential decay model the spin relaxation between two position with magnetisation direction θ_i to θ_{i+1} is proposed as,

$$P_{i+1} = P_i - (P_i - P_0 \cos\theta_{i+1}) \left(1 - e^{-(\alpha+\beta\cos\theta_i)\frac{L}{\lambda}}\right) \tag{4.12}$$

where P_i and P_{i+1} are the spin polarisations at the position with magnetisation θ_i and θ_{i+1} respectively, L is the distance between θ_i and θ_{i+1}, we assume $d\theta/dl$ is constant within distance L, λ is the spin diffusion length, α is the magnetic-independent scattering constant and β is the magnetic scattering constant. These parameters have been fitted to match the experimental results. When electrons travel in magnetic conductor the spin orientation tends to follow the magnetisation orientation. However the change of spin orientation does not happen the same time when the electron enters a different region such as from θ_i to θ_{i+1}. In this case the change of spin orientation follows a diffusion model, so in the model we can calculate the spin polarisation of position i+1 from its neighbour position i where current follows from. Equation 4.12 shows how spins lose their polarisation inside a magnetised material. The spin relaxation model shown in Equation 4.11 is a special situation when $\theta \equiv 90°$ and $\alpha \equiv 1$, the spins lose the polarisation in a non magnetised or randomly magnetised region. The calculated spin polarisation against position in the spin-valve based on the OOMMF simulation results can be seen in Figure 4.18. $P = \frac{P_\uparrow - P_\downarrow}{P_\uparrow + P_\downarrow}$ is the spin polarisation and positive value means there are more up-arrowed spins. Figures 4.18(a1, a2) show the spin accumulation inside a 100 nm long bridge of parallel and antiparallel states, respectively, while Figures 4.18(b1, b2) show the 30 nm case. The value $\alpha = 3$ and $\beta = 3$ was fitted according to the measurement result of the 100 nm constriction. In theory the value of α should be 1, but in experiments, the Ni film's defect and interface (Au on top and SiO_2 at the bottom) spin collision reduces the spin diffusion length to $\lambda_{eff} = \lambda/\alpha$.

If we put the spin polarisation of the parallel and anti-parallel state together, the amount of spins whose energy is increased by the switching of the domain magnetisation is shown in Figure 4.19. The slashed area shows the amount of spins entering

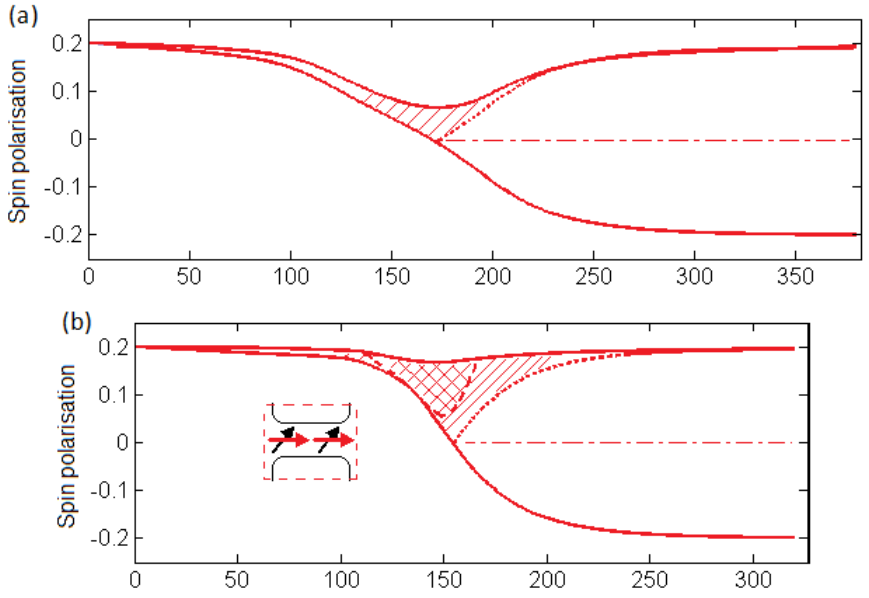

FIGURE 4.19: The spin accumulation when switching happens (domain wall appears). The slashed areas in (a) (100 nm long bridge) and (b) (100 nm long bridge) indicate the percentage of electrons entering the high spin energy state. The crosshatched area in (b) is the reduction caused by the strain inside the 30 nm long bridge.

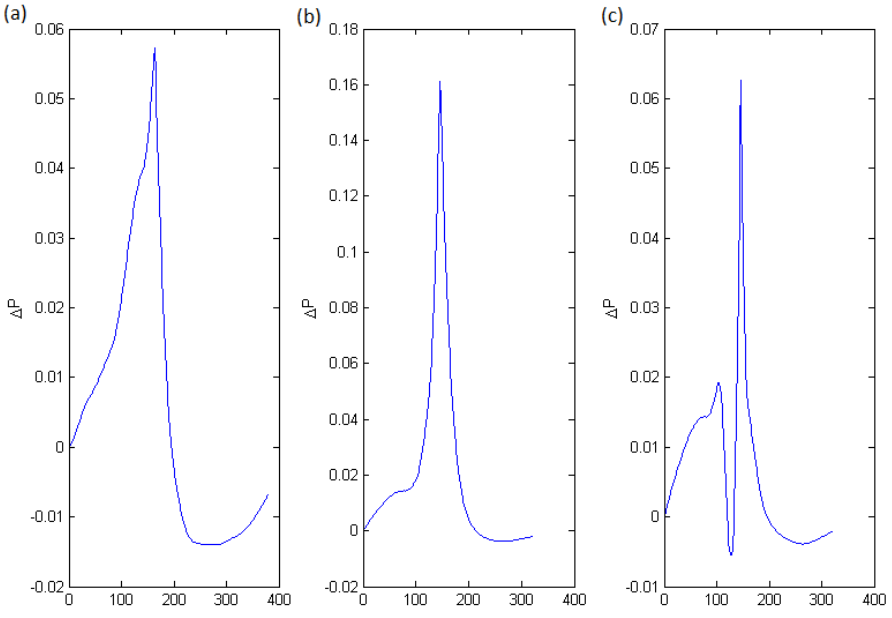

FIGURE 4.20: Spin polarisation difference distribution of the spin-valve with 100 nm long bridge (a), the spin-valve with 30 nm long bridge without considering the influence of strain (b) and the spin-valve with 30 nm long bridge by taking the strain into account (c)

the high energy state when the free pad switches. The crosshatched area shows the amount of spins which lose their polarisation before switching because of the strain inside the bridge. The high magnetostriction of Ni results high magnetoelastic energy when strain is applied inside the bridge. The He ion patterned bridge contains large strain because patterned bridge size changed from 20 nm-wide and 20 nm-long to 13 nm-wide and 30 nm-long. The magnetoelastic energy could force the magnetisation around the bridge follow the strain orientation, which increases the domain wall width. By plotting the spin polarisation difference, the relation between ΔP and position in the device is established as shown in Figure 4.20. Figure 4.20(a) indicates 5.8% of the electrons enter the high energy state when domain wall appears in the 100 nm-long bridge. Figure 4.20(b) shows 16% of this type of electrons in the 30 nm unstrained bridge, and Figure 4.20c shows that this ratio has been reduced to 6% due to the strain introduced by substrate swalling caused by helium ion beam milling. We take the peak values in Figures 4.20(a, c) as the value of ΔP in Equation 4.10. The calculated ΔV in both case is about 20 μV. The reduction is domain wall width does not lead to an increase in magnetoresistance as the magnetoelastic forces the $2 \times 90^{\circ}$ domain walls to appear. The change in ΔR is therefore equal in both e-beam and helium ion beam fabricated structures. The respective ΔR value is 0.4 Ω, which agrees with the measurement results.

4.7 Conclusion

Domain wall magnetoresistance of 0.1% has been measured in an H-shaped spin-valve with a constriction fabricated by e-beam lithography (width = 94 nm) and 0.2% in a constriction fabricated by helium ion beam milling (width = 32 nm). The strain introduced by the substrate swelling increases the domain wall width by increasing the magnetoelastic energy and results in negative impact on the magnetoresistance ratio. The anisotropic magnetoresistance analysis shows that the AMR effect is only 10% of the domain wall magnetoresistance in our H-shaped spin-valve. In order to keep the signal to noise ratio larger than 2:1 the measurement current needs to be larger than 5 μA. A spin accumulation model has been created to analyse the domain wall magnetoresistance based on experimental results. The step in the spin-valve curve is explained in terms of Zeeman energy during switching. According to the spin accumulation model, a larger spin polarisation or a shorter domain wall constriction width gives higher domain wall magnetoresitance ratio.

The smallest gap in the H-shaped spin-valve we have achieved is about 5 nm. The resistance measurement shows the milling has been through to the bottom and the bridge is still conducting. However, the magnetoresistance measurements do not show magnetoresistance signal. In theory, the 5 nm spacing should be sufficient to prevent coupling as simulations show that coupling only happens below 1 nm. Thus, due to the edge roughness in the experiment, some coupling might exist. In future work, if possible it is better to measure the magnetisation of the pads during the switching to explore what exactly happens inside the constricted domain wall experimentally. A function generator and lock-in amplifier system can be used to largely reduce the noise and therefore the measurement current. However, this requires wire bonding and protection circuit to prevent the spin-valve from being blown off.

Chapter 5

Plasmonic nanoantennas

5.1 Introduction to plasmonic nanoantennas

As being discussed in the E-beam fabrication section, this PhD thesis contains research on plasmonic nanoantennas. The research on surface plasmon resonance (SPR) has become popular because of its wide range of successful applications in biomedical sensing [92, 93, 94], material sensing [95, 96, 97] and high speed communications [98]. The SPR is the resonant oscillation of valence electrons in a solid stimulated by illumination. The plasmonic nanoantenna is one type of SPR devices, which is potentially capable of resulting in ultrafast integrated photonic circuits because of its high speed and sensitivity.

The surface plasmons are surface electromagnetic waves in a direction parallel to the interface of the metal and the optical transparent material. The resonance happens when the field intensity at extremes of the metal reaches a local maximum value. In a relative field intensity spectrum there may be multiple resonances corresponding to different wavelengths. The near-field is electromagnetic field within 1 wavelength of the reflecting surface. Its amplitude is proportional to the relative intensity which is the antenna reflection intensity to the reflection intensity of the background (I/I_O or $\Delta R/R$). The near-field intensity is often used in the simulation results because this is what we can get from the FDTD (finite different time domain) calculation. In contrast the extinction cross section (σ) is often used in measurement result because this is what can be measured by reading the energy integration signal of a CCD receiver. We can understand in this way that due to the plasmonic resonance of an antenna, the near-field intensity in the gap increases, so both the optical reflection and absorption increases, which

can be seen as equivalent to the increase of extinction cross section. The surface plasmonic resonance is very sensitive to the shape of the metal and the refractive index of the optical transparent material. This is why it is often used in sensing applications.

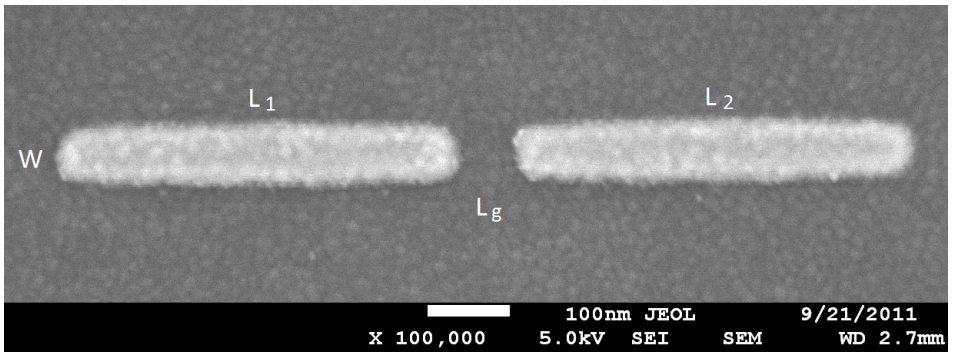

FIGURE 5.1: SEM micrograph of a plasmonic nanoantenna. The antenna was made of 25 nm thick Au on top of an Indium Tin Oxide, ITO-coated glass substrate. The length of the left rod is L_1 and the right one is L_2. The width of the rods is W. The width of the gap is L_g. In our experiment, we keep $L_1 + L_2$ a constant value.

The dimer nanoantenna is a type of localised surface plasmon resonance device made of two pieces of nanometer-sized metal rods (Figure 5.1). The optical characteristics of the antenna are determined by the length of rods L_1, L_2, width of rods W, film thickness T, gap width L_g and interface material's refractive index [99]. There are several types of antennas reported by different researchers (Table 5.1). Properly designed antennas could have their incident electromagnetic field enhanced by several orders. Figure 5.2 [100] shows a symmetric antenna structure at its maximum gap intensity. Moreover the absorption peak is very sensitive to the electric properties of the material inside the gap as reported by Alù *et al* in 2008 [101].

Figure 5.3 shows the scattering resonance shift due to the different permittivity of materials inside the gap of a dimer nanoantenna. It can be seen that there is a redshift on the resonant frequency when permittivity increases. The Au and Ag filling the gap has the same resonant frequency, thus the resonant frequency reaches the lowest value when the material filling the gap is highly conductive. However, there is no clear relation between the resonant frequency and the material's conductivity. According to a paper published by Brongersma, the dimer nanoantenna is very sensitive to the gapping materials electric property including not only the permittivity (capacitance) but permeability (inductance) and mobility (resistance) as well [94].

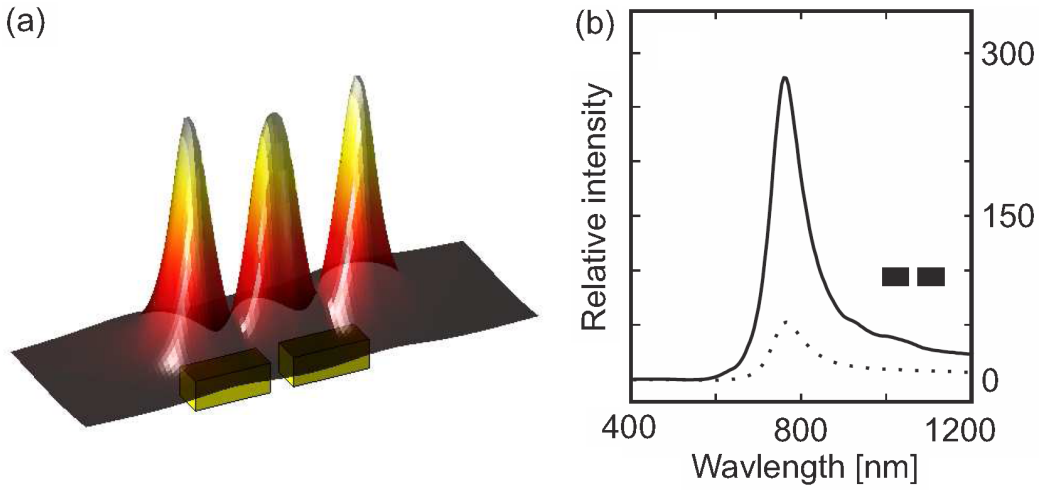

FIGURE 5.2: (a) Near-field intensity distribution 20 nm above a symmetric dimer antenna at wavelength 760 nm. (b) Relative field intensity spectra in the gap (solid line) and at the extremity (dotted line) for the dipole antennas. This is a simulated result based on the geometrical size $L_1 = L_2 = 230$ nm, $L_g = 30$ nm. The effective wavelength λ_{eff} of this antenna is 460 nm. After Fischer *et al* [100], copyright OSA

TABLE 5.1: Antennas research work

Structure	Researcher	year	Found
Rectangular	Cubukcu *et al* [102]	2006	plasmonic laser antennas
	Muskens *et al* [103]	2007	dark field scattering spectrum
	Alu *et al* [101]	2008	tunable scattering resonance
	Abb *et al* [104]	2011	injecting carriers into substrate
Bow-tie	Farahani *et al* [105]	2005	sensing single quantum dots
	Merlein*et al* [106]	2008	two dipole plasmon resonances
Stacks	Lévêque *et al* [107]	2006	tuning resonance wavelength
	Su *et al* [108]	2006	tunable surface plasmon
Quantum dots	Curto *et al* [109]	2010	controllable emission
V-shaped	Zhang *et al* [110]	2007	high enhancement factors

In this chapter we are going to introduce a hybrid asymmetric dimer ITO antenna fabricated by e-beam lithography and Au lift-off. It contains two pieces of Au rods with the length L_1, L_2 and a gap width L_g. Different combinations of these parameters can result in various optical behaviours.

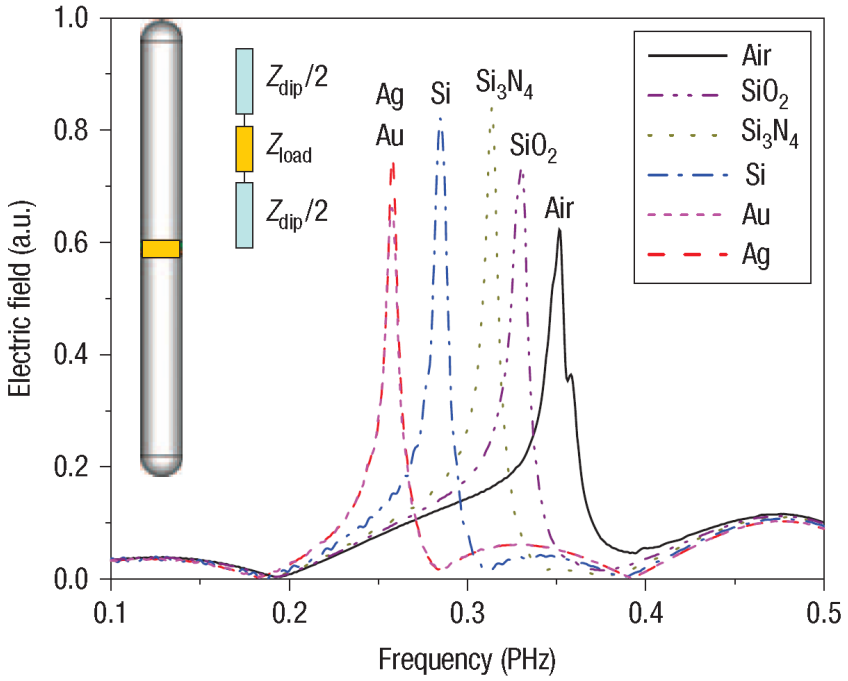

FIGURE 5.3: Numerical simulation of scattering resonance shift as a function of frequency of the symmetric dimer nanoantennas with different materials filling the gap. From the right hand side to the left the peaks are from materials of air (ϵ_0), SiO_2 ($\epsilon_{SiO2} = 2.36\epsilon_0$), Si_3N_4 ($\epsilon_{Si3N4} = 4.01\epsilon_0$), Si ($\epsilon_{Si} = 13.35\epsilon_0$), Au and Ag. The plots of Au and Ag are mostly overlapped but the peak of Ag is slightly higher than Au. After Alú *et al* [101], copyright Nature

5.2 Fabrication results

The plasmonic nanoantennas were fabricated on an ITO-coated glass substrate via electron beam lithography and lift-off (Figure 5.1). ITO stands for Indium Tin Oxide or Tin-doped Indium Oxide. Typically it is In_2O_3 with 1% - 10% SnO_2. It is a kind of transparent conductor whose electron carrier concentration can be as large as 10^{22} /cm^3. Because ITO is highly conductive, the sample is not charged up during exposure. However, the ITO has grain sizes of 10 - 100 nm depending on its thickness. The point spread function of the substrate is not calculatable due to the roughness. The result is that a dose test is required for every new designs, because each design contains the different pattern density. Furthermore we cannot avoid proximity effect correction and use single dose for the exposure, because there are both large and small patterns in the same area show in Figure 5.4.

Figure 5.4(a) is the micrograph of a pattern exposed with single dose without proximity effect correction (PEC). It can be seen that the patterns close to the 100 μm pad are brighter than the ones far away. All the nano antennas have

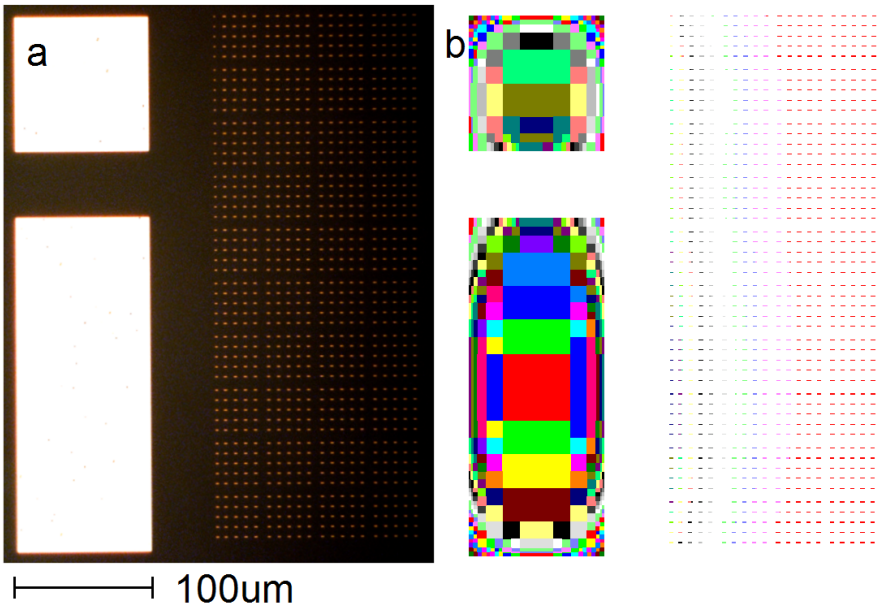

FIGURE 5.4: (a) Optical microscope micrograph of a group of patterned nanoantennas with eye mark on the left hand side. The eye mark could help to locate samples in optical measurement. (b) the dose map of the nanoantennas' pattern file.

the same total length of 600 nm and should look like the same brightness under optical microscope. The difference on the brightness was caused by the different of exposure doses on each individual patterns. The additional dose of the small patterns is mainly from the big area. And the influence distance is more than 100 μm. The point spread functions (PSF) of the back scattered electrons from a flat SiO_2 surface only has the length of around 30 μm shown in Figure 5.5. The conducting surface on top of SiO_2 only increases the energy distribution within a 10 μm range. Therefore we load an ideal Gaussian PSF whose maximum energy distribution distance is as large as 50 μm and do the coarse PEC (Figure 5.5b) and leave all the rest to the dose test. In addition, a size sweeping from 2 nm to 50 nm on the critical dimension was used to avoid failure caused by the dose drift.

The result of e-beam exposure on the critical dimension, gap width W_g of the nanoantenna structure is shown in Figure 5.6. Compared to the domain wall magnetoresistance fabrication the difference is that there is no bridge between the rods for the nanoantenna structure. The minimum gap size of DWMR spin-valve by e-beam lithography only process is 60 nm whereas for nanoantenna it is 10 nm. The EBL technique with the bi-layer resist approach leads to an undercut which facilitates the lift-off procedure. An SEM image of the under-cut created by the bi-layer resist is shown in Figure 5.7. The size of the under-cut varies from 30 nm to

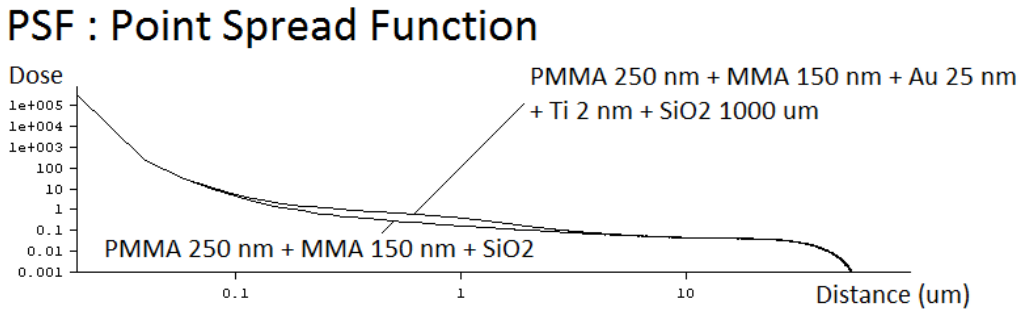

FIGURE 5.5: The dose distribution of the point spread function for SiO_2 substrate and Ti-Au coated SiO_2 substrate

100 nm and is determined by the pattern density, exposure dose, resist thickness, developer MIBK : IPA ratio and development time. A successfully-defined H-device pattern is shown in the SEM image in Figure 5.8b. If there is no bridge in between two pads, the gap can be made as narrow as sub-20 nm with this method, because the top layer resist can be supported by the two ends even when the area underneath is cleared. However, when the bridge is included in the design, the minimum size of the gap between the two sides of the device over which the bridge extends is limited by the undercut to 60 nm. If the gap is defined to be smaller than 60 nm, undercuts from either side can connect. The top layer of resist is then no longer supported and so is unstable and prone to distortion, as shown in Figure 5.8c.

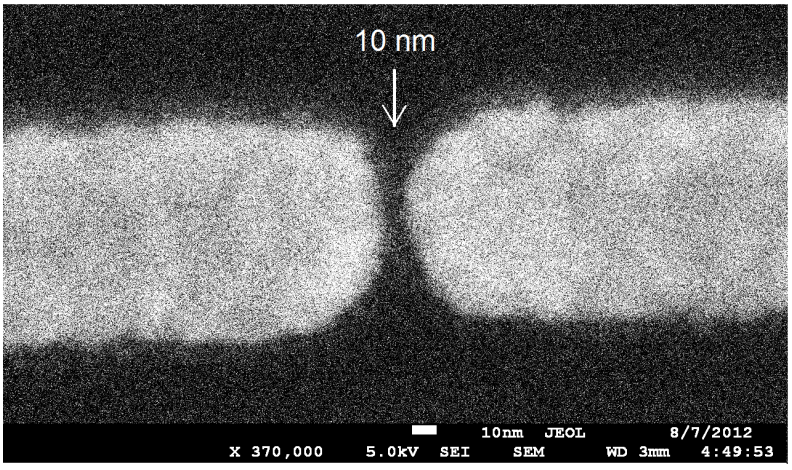

FIGURE 5.6: SEM micrograph of the critical dimension W_g of a nanoantenna. The minimum gap width we can get with this method is 10 nm. A size sweep with a step of 2 nm is required to prevent failure from the dose drift (a slight dose change between each exposures due to the difference in the resist preparation and development processes).

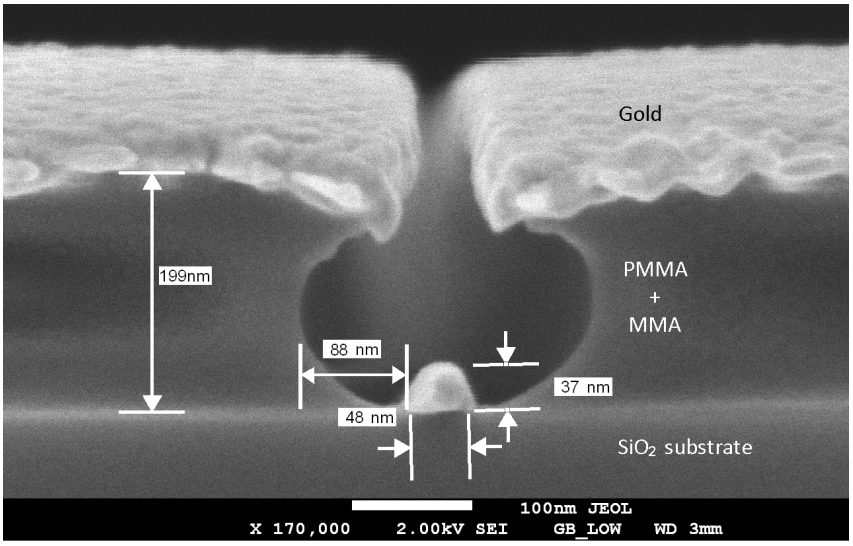

FIGURE 5.7: SEM cross-sectional view of the bi-layer resist under-cut. From top to bottom there is a gold layer by evaporation, PMMA + MMA spin coated electron beam lithography resist and thermally grown SiO_2. The width of the half under-cut can be as large as 80 nm.

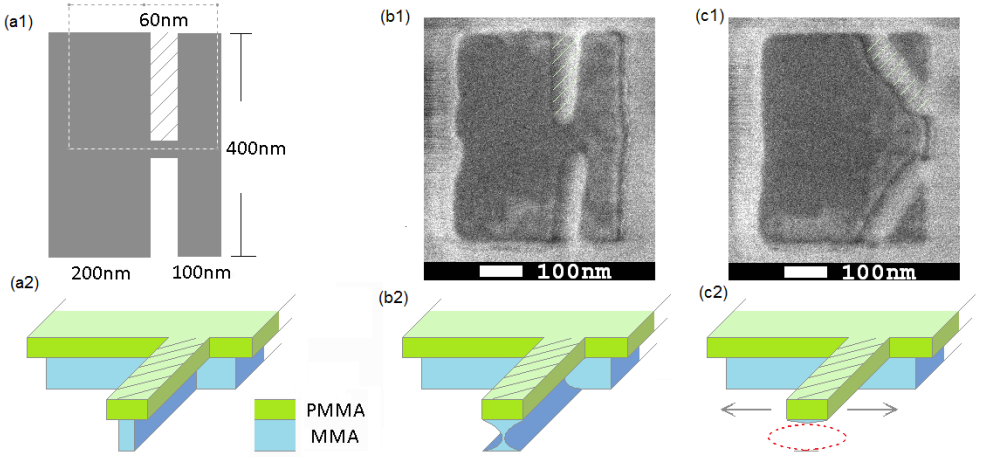

FIGURE 5.8: (a1) Ni device pattern design. After the evaporation process, the Ni device is surrounded with electron beam resist. (a2) The ideal shape of the bi-layer electron beam lithography resist with undercut 3-D view. (b1) SEM micrograph of a device fabricated with the design of (a1). (b2) resist undercut of the device (b1) by inference. (c1) SEM image of a failed device. (c2) Over-etched undercut by inference. It can be seen that the e-beam resist area shown in (a1) is slanted. The undercuts are overlapping, which results in the OMMA layer floating. This will lead to a failed device, as in (c1).

5.3 Theorical results

In our device (Figure 5.1) the total length of the two rods, $L_1 + L_2$ is always 600 nm. The length of the gap, L_g changes from 20 nm to 100 nm in steps of 5 nm. The width of the rods W is about 60 nm, and the thickness T is 25 nm. In a simple analytical formula of a single rod length to the resonant wavelength, the rod is assumed to be cylindrical. In first approximation we can assume our rod to be cylindrical with a radius $R = \sqrt{\frac{WT}{\pi}} = 20$ nm.

The length of the rods influences the effective resonant wavelength of the incident light. The relation is the same to the classic antenna and electromagnetic wave shown as [111],

$$L_x = n \times \frac{1}{2}\lambda_{eff}, [x = (1, 2)] \tag{5.1}$$

The plasma resonance reaches the highest intensity in the rod when $n = 1, 3, 5...$ and the lowest at $n = 2, 4, 6....$ However the effective wavelength does not exactly equal to the wavelength of incident light [99], because incident light is not perfectly reflected by a metal surface due to the oscillations of the free electron gas. The relation between effective and resonant wavelength is given by (Novotny *et al* in 2007 [99]),

$$\frac{\lambda_{eff}}{2\pi R} = 13.74 - \frac{0.12\left[\varepsilon_\infty + \varepsilon_s 141.04\right]}{\varepsilon_s} - \frac{2}{\pi} + \frac{\lambda}{\lambda_P} 0.12 \frac{\sqrt{\varepsilon_\infty + \varepsilon_s 141.04}}{\varepsilon_s} \tag{5.2}$$

where λ_{eff} is the effective wavelength, R is the radius of the rod, ε_∞ is the high frequency limit of the dielectric function (for Au $\varepsilon_\infty \approx 11$, for Ag $\varepsilon_\infty \approx 3.5$), ε_s is the dielectric function of surrounding material (such as air and ITO), n is the order of the mode, and L is the length of the nano-rod. To get this simplified equation, the substrate material is assumed to be highly conductive and $4R < L$, $R << \lambda$. Figure 5.9 shows the plot of Equation 5.2 for Au and Ag when R is 5 nm, 10 nm and 20 nm.

Figure 5.10 shows the expected behaviour of our asymmetric nanoantennas. Figures 5.10(a, d) indicate the spectral positions of the L_1 and L_2's resonances against L_2. The contour plots in Figures 5.10(b, c, e, f) show the extinction cross section, σ_{ext} as a function of L_2 and λ. The interaction between the long and short rods are identifiable. Total rods' length $L_1 + L_2$ is a constant value, either 600 nm in Figures 5.10(a, b, c) or 1000 nm in Figures 5.10(d, e, f), thus if L_2 increases, L_1 decreases correspondingly. If we put Equation 5.1 and 5.1 together, the resonant

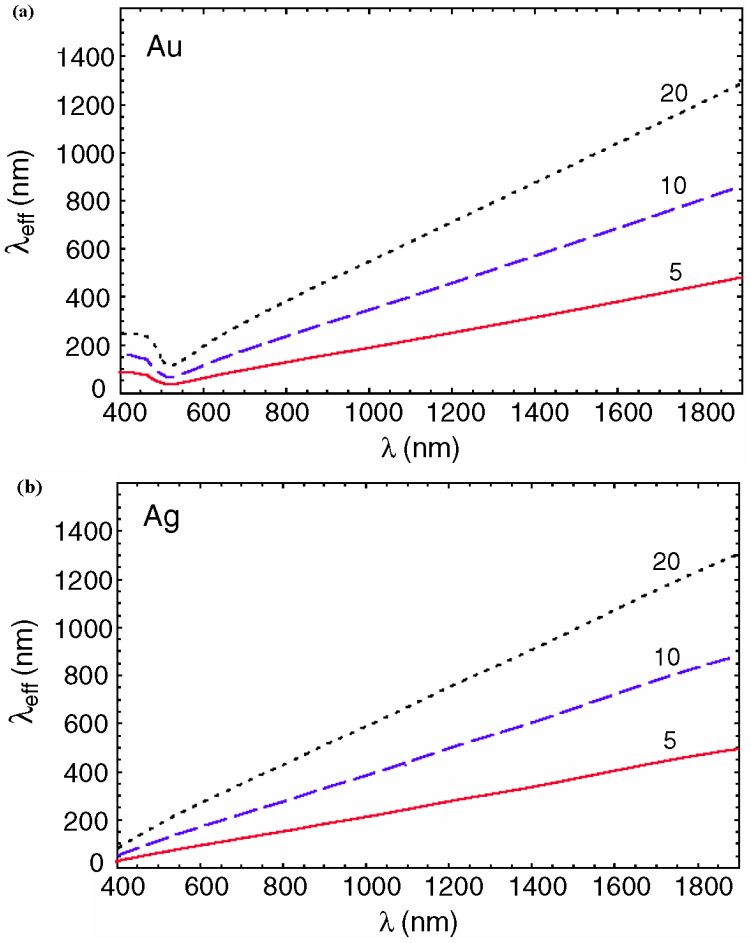

FIGURE 5.9: Plot of effective wavelength against wavelength of incident light of (a) Au and (b) Ag. The solid red lines indicate when $R = 5\ nm$, blue dashed lines indicate when $R = 10\ nm$, black dotted lines indicate when $R = 20\ nm$. After Novotny *et al* [99], copyright AIP

wavelength as a function of L_1 and L_2 can be expressed by,

$$\lambda = \left(\frac{\lambda_p \varepsilon_s}{0.12\sqrt{\varepsilon_\infty + 141.04\varepsilon_s}}\right)\left(\frac{nL}{4\pi R} - 13.74 - \frac{0.12}{\varepsilon_s}\sqrt{\varepsilon_\infty + 141.04\varepsilon_s} - \frac{2}{\pi}\right) \quad (5.3)$$

The plots of resonant wavelength as a function of L_1 and L_2 in the 1st, 2nd and 3rd orders are shown in Figure 5.10(a) ($L_1 + L_2 = 600$ nm). The solid lines are in bright mode whereas dashed lines are in dark mode. The red lines represent the long rod L_2 and blue lines are for the short rod L_1. The circles indicate the places where the 1st order resonant wavelength of L_1 crosses the higher orders of L_2. The light scattering simulation based on such an asymmetric nanoantenna result is shown in Figure 5.10(b, c). The photonic resonance of substrate and rectangular antenna were simulated by a finite difference in time domain (FDTD) method.

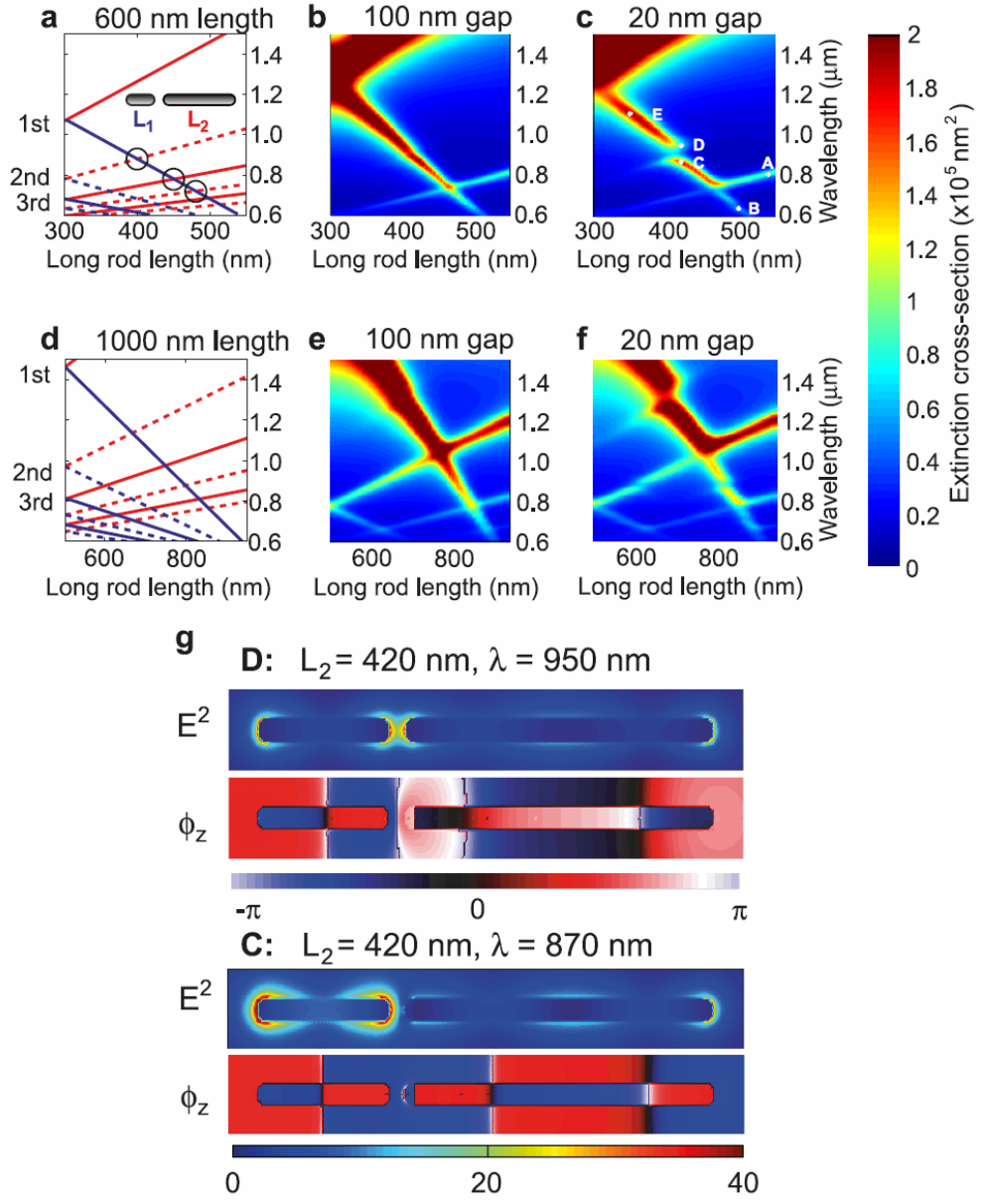

FIGURE 5.10: (a, d) Plot of spectral positions of the resonances, λ as a function of length of an individual rod(L_1, L_2) in an asymmetric nanoantenna with $L_1 + L_2 = 600$ nm (a) and $L_1 + L_2 = 1000$ nm (d). Red lines show the incident wavelength to excite the long rod ($300 \leq L_2 \leq 600$), whereas the blue lines show the short rod's ($300 \geq L_1 \geq 0$). The solid lines indicate the bright mode ($n = 1, 3, 5...$) whilst the dashed lines indicate the dark mode ($n = 2, 4, 6...$). (b, c, e, f) contour plot of extinction cross-section (σ_{ext}) as a function of L_2 and λ. (b) $L_1 + L_2 = 600$ nm, $L_g = 100$ nm. (c) $L_1 + L_2 = 600$ nm, $L_g = 20$ nm. (e) $L_1 + L_2 = 1000$ nm, $L_g = 100$ nm. (f) $L_1 + L_2 = 1000$ nm, $L_g = 20$ nm. (g) Near-field enhancement modulus and phase distribution in the antenna plane at the spectral positions of C and D shown in Fig.(c). C and D have the same geometrical size $L_1 = 180$ nm, $L_2 = 420$ nm, $L_g = 20$ nm. (Thanks to Martina Abb)

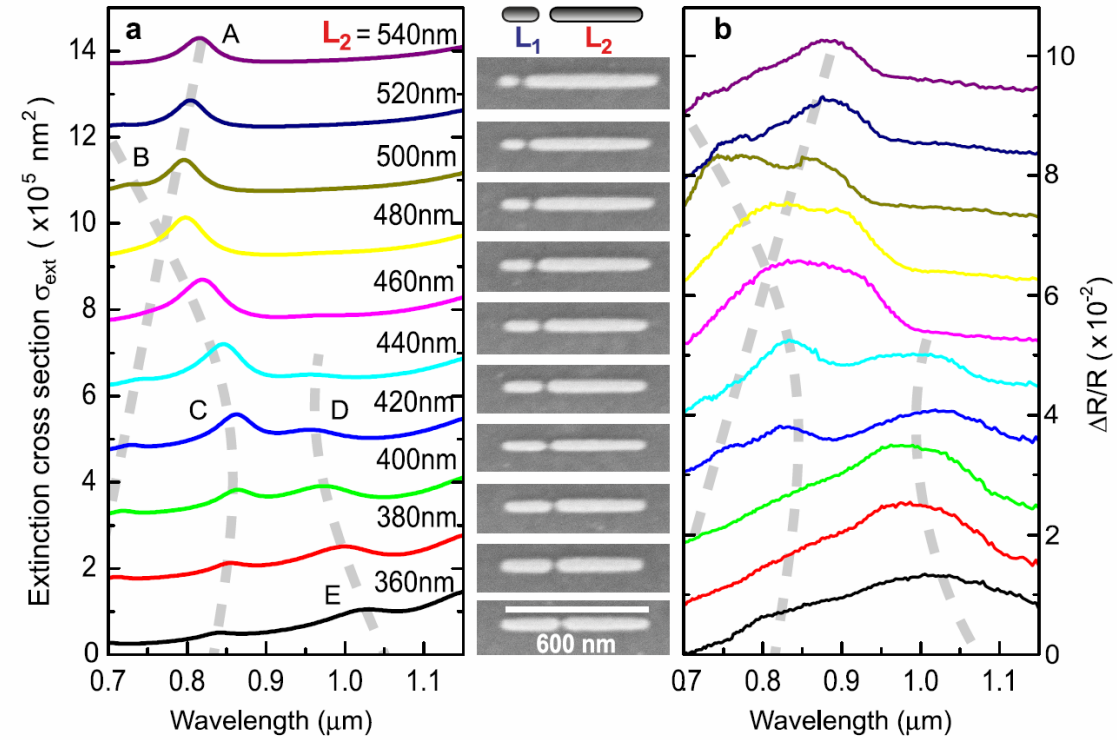

FIGURE 5.11: (a) Theoretical and (b) experimental plots of extinction cross sections against wavelength of incident light of asymmetric nanoantennas whose L_2 changes from 360 nm to 540 nm with a step of 20 nm. Corresponding SEM micrographs are shown in the center. The total length of L_1 and L_2 is 600 nm. The gap width, L_g is 20 nm. The letters, A-E in (a) indicate the same simulation points in Figure 5.10 (c). Dashed gray lines are guides of the bright modes to the eye. The axis $\Delta R/R$ in (b) is the relative reflection (proportional to σ_{ext}) of the nanoantennas measured by a lock-in amplifier. (Thanks to Martina Abb)

The dependence of coupled resonance between two rods on the different antenna parameters were performed by using boundary element method (BEM). From Figure 5.10(b), it can be seen that when the gap size is 100 nm the superposition of a bright mode and a dark mode shows bright. This means that the interaction between two excited Au rods is very small around the gap width of 100 nm. If there is no interaction we can only see the bright mode, but we cannot tell whether the dark mode is still there or not. When the gap width is reduced down to 50 nm or below, the superposition of a bright mode and a dark mode results in a dark mode. This can be clearly seen in Figure 5.10(c), as the blue area between C and D is caused by the 2nd order dark mode of L_2. Moreover we can only see the dark mode when it cuts off the curve of a bright mode. Figure 5.11 shows the experimental result corresponding the simulation as shown in Figure 5.10(c). The dashed lines are guide to the eye of the bright modes. The interaction between the bright

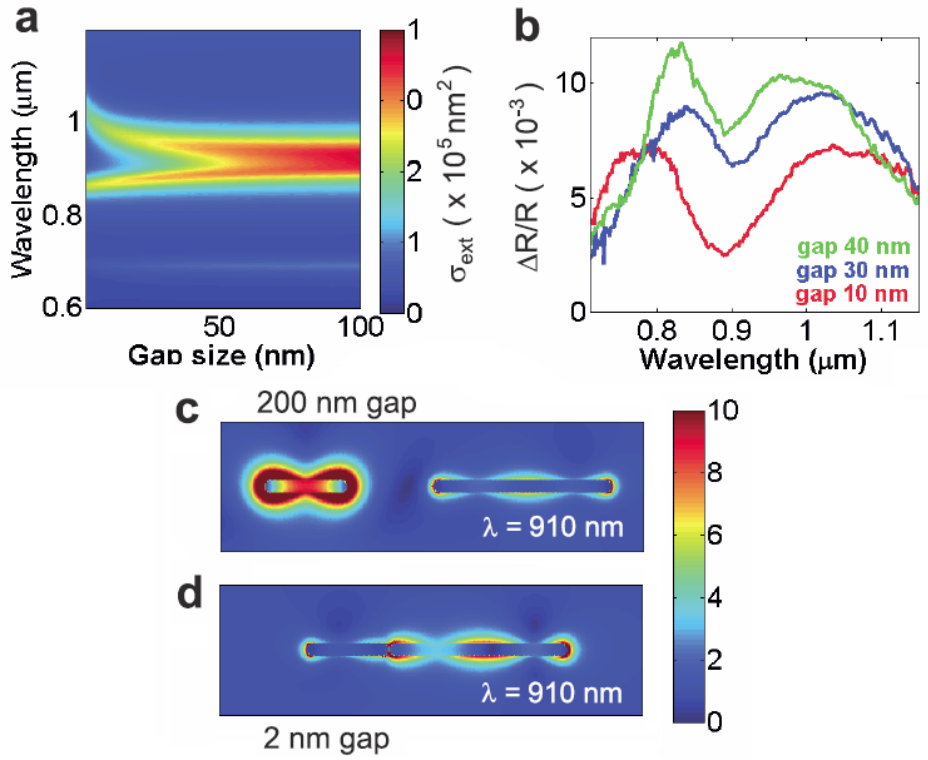

FIGURE 5.12: (a) Contour plot of extinction cross-section as a function of gap width and resonant wavelength, W_g of an asymmetric antenna with $L_2 = 420$ nm and $L_1 = 180$ nm. (b) Experimental spectra of differential reflectance for the same asymmetric antenna for three different gap sizes. (c, d) Near-field intensity maps at a wavelength of 910 nm for $W_g = 200$ nm and $W_g = 2$ nm respectively. (Thanks to Martina Abb)

mode and dark mode can be further explained by the near-field phase distribution of an asymmetric nanoantenna as shown in Figure 5.10(g). When the two rods are close enough, the two resonances inside the gap with a phase difference of π neutralise. More detailed analyse can be found in Figure 5.12 which is about the influence of the gap width to the interaction between the bright and dark modes. Figure 5.12(a) shows the simulation result of a critical gap width of 50 nm below which the superposition shows the dark mode. Figure 5.12(b) shows a group of measurement results corresponding to the simulation of gap size 10 nm, 30 nm and 40 nm. The vertical axes is proportional to the reflection of incident light. The bottom between two reflection peaks agrees with the superposed bright and dark modes. The splitting is also known as electromagnetically induced transparency. The strong coupling between a dark mode and a bright mode results in a near-perfect transparency instead of an otherwise strong absorption line.

5.4 Conclusions

The asymmetric nanoantennas show strong interaction effects when the gap width is smaller than 30 nm. These effects were proved by both simulation and experimental results. These nanoantennas can be used as nanofilters, for the spectrum can be tuned by the geometrical parameters. The field intensity inside the gap can either be enhanced by two bright mode resonances or reduced by one dark mode resonance in any one rod.

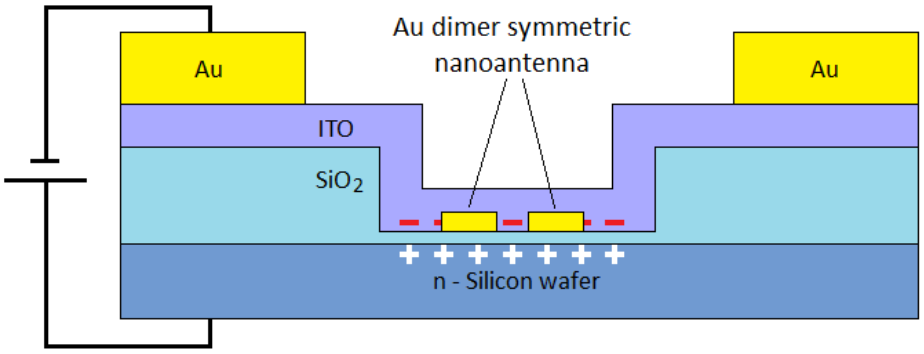

FIGURE 5.13: Schematic diagram of a dimer nanoantenna ITO MOSFET. From bottom to top, there are n-type silicon bottom gate, gate SiO_2, trench SiO_2, symmetric nanoantenna, surrounding ITO, and Au contact. If a bias is applied there will be positive charge appear on the silicon side of the gate SiO_2 whereas negative charge on the ITO side of the gate SiO_2 interface.

Figure 5.13 shows our design of the structure and operation of a dimer nanoantenna ITO MOSFET. When applying a negative bias the concentration of free electrons in ITO is reduced whilst a positive bias increases it. The increase of carrier concentration in ITO decreases the real part of permittivity [104], which results blue shift in the resonant spectrum [101]. This effect was analysed by Feigenbaum *et al* in 2010 [112]. The concentration of free electrons inside the gap of a nanoantenna may influence its resonant wavelength. The plasmonic resonant frequency of a dimer nanoantenna with a empty gap is half of the one with Au in the gap. We assume that if the electron concentration of the ITO inside the gap can be controlled by a gate bias, the resonant frequency can be controlled continuously. For example, when the gate voltage changes from negative to positive (e.g. from -2 V to 2V) the peak of the resonant spectrum moves from short wavelength to long wavelength (e.g. from 0.8 μm to 1.2 μm). In another view, if we keep the wavelength of an incident light constant, such as 0.8 μm, and increase the gate voltage from -2 V to +2 V, the absorption of the 0.8 μm light changes from high

to low whereas the reflection of the light changes from low to high. Thus when the gate bias is below a threshold V_t, the reflection of the light can be seen as in the off-state. When it is above V_t, the reflection of the light is in the on-state. This behaviour is the similar to a MOSFET, but the drain-source current is replaced by the incident-reflection light.

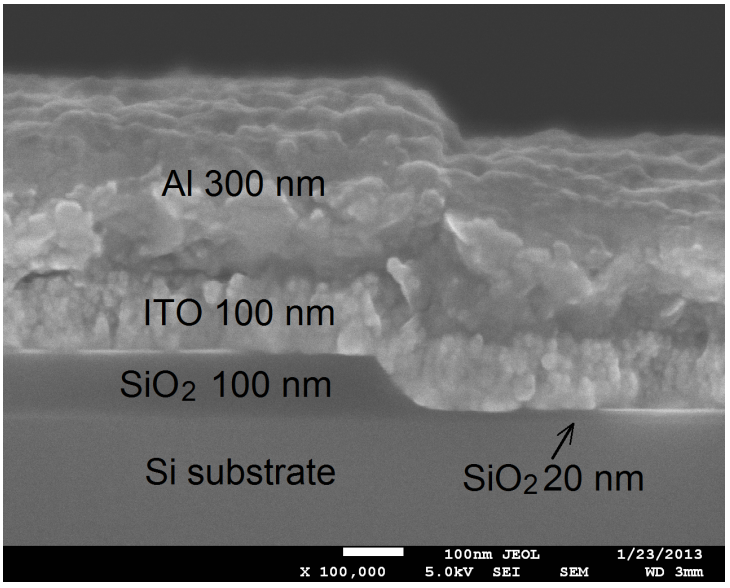

FIGURE 5.14: SEM micrograph of the cross sectional view of the dimer nanoantenna ITO MOSFET.

Figure 5.14 shows the completed result of the fabrication of the dimer nanoantenna ITO MOSFET. We start with a piece of N-type highly doped Si $<100>$ substrate. A 100 nm SiO_2 thin film was thermally grown on top by wet oxidation. A window of 20 nm thick SiO_2 was created by wet etch. Nano-antennas were deposited in the window on top of 20 nm-thick SiO_2 by electron beam lithography and lift-off. Then 100 nm thick ITO was deposited by evaporation with an oxygen pressure of 4×10^{-4} mBar. Four hours annealing was followed by ITO lift-off to calibrate the electron concentration of ITO film to 3.84×10^{20} /cm^2. An Al electrode was deposited at last to allow probing and wire bonding. The uniformity of thermal oxidation in a 6 inch area is ± 2 nm. The 20 nm thick gate oxide uniformity is ± 2 nm. The maximum voltage can be applied between the 20 nm gate oxide is ± 3 V. The measurement of the antennas requires further calibration on the geometrical size of the nano-antennas, thickness of gate SiO_2 and conductivity of ITO.

Chapter 6

Summary

In this thesis, the world's first smallest functional single domain wall magnetoresistance spin-valve has been reported. The constriction width of the magnetic domain wall has been scaled down to 30 nm with a combination of e-beam lithography and helium ion beam milling. A 5-layered circuit structure has been developed to connect the measurement wire from the 200 μm-wide 300 nm-thick measurement pads to the 100 nm wide and 14 nm thick magnetic film. The room temperature magnetoresistance has been measured with a 4-point measurement setup in a sweeping external magnetic field. It shows clearly the difference in resistance between parallel and antiparallel configuration. The room temperature magnetoresistance ratio has been found to be around 0.1% with 90 nm and 0.2% with 30 nm constriction width. A spin accumulation model has been analysed to explain what happens inside the bridge including the electron spins collision, anisotropy magnetoresistance contribution and domain wall extension caused by the strains.

In the e-beam lithography, a checkerboard dose sensor has been developed to detect the base dose of any type of e-beam resist. A dose proximity effect correction is developed with the base dose to process the complex exposure. The PMMA and MMA bi-layer resist is found to be suitable for a lift-off with minimum gap width of 10 nm (without bridge) and 60 nm (with bridge). A structure of 3 e-beam layers is developed to connect wires to sub-100 nm region without process damage. A combination of photo and e-beam lithography is developed to reduce the e-beam exposure time.

Sub-20 nm gap is achieved by using the combination of e-beam lithography and helium ion beam milling. A resistance to milling depth model has been used to detected the milling depth with a resolution of 2 nm which is difficult to measure

with either AFM or cross-section SEM. The substrate swelling has been analysed carefully to determine the limitation of this fabrication method and the influence on the magnetic behaviour. Because of the linear relation between swelling width and milling width, a suggested maximum milling width of 20 nm has been found. The milling parameters of 30 kV, 1 pA, 10 μs dwell time and 1 nm pixel size are optimised by considering the sub-surface swelling, beam spot size, substrate drifting and side wall re-sputtering. The milling efficiency was found to be 0.044 atoms/ion which is the half of the SRIM simulated result of 0.09 atoms/ion. The step-like magnetoresistance curve shows that the magnetic behaviour is not completely destroyed by the implanted He atoms.

Asymmetric dimer nanoantennas have been fabricated by e-beam lithography and Au lift-off. The measured resonant spectrum agrees to the simulated results showing the light and dark modes. The interaction between light and dark modes was found only when the gap width is below 50 nm which fully agrees with the theoretical result. A near-perfect transparency was found in a strong coupling between a dark and bright mode when the rods lengths are 420 nm and 180 nm. As the electron concentration of the ITO thin film can be controlled by a back-side SiO_2 gate, an electric controllable plasmonic dimer nanoantenna has been designed in this thesis which will be fabricated and analysed in future work. A wavelength shift based on the changing of the gate bias is expected to be seen. Further applications such as an electric controlled optical switch can be developed based on this phenomena.

The magnetoresistance in our current devices is too small to be technologically relevant. In future work, a device with reduced geometrical size will be designed to detect magnetoresistance when the constriction width is below 30 nm. A more stable setup of the cryogenic magnetic measurement system will need to be developed, to allow the temperature dependence of the domain wall magnetoresistance spin valve to be analysed.

Bibliography

[1] M. N. Baibich, J. M. Broto, A. Fert, F. Nguyen Van Dau, F. Petroff, P. Eitenne, G. Greuzet, A. Friederich, and J. Chazelas, "Giant Magnetoresistance of (001) Fe/ (001) Cr Magnetic Superlattices," *Physical Review letters*, vol. 61, no. 21, pp. 2472–2475, 1988.

[2] Jagadeesh Subbaiah Moodera, Lisa R. Kinder, Terrilyn M. Wong, and R. Meservey, "Large magnetoresistance at room temperature in ferromagnetic thin film tunnel junctions," *Physical Review Letters*, vol. 74, no. 16, pp. 3273 – 3276, 1995.

[3] Behtash Behin-Aein, Deepanjan Datta, Sayeef Salahuddin, and Supriyo Datta, "Proposal for an all-spin logic device with built-in memory.," *Nature nanotechnology*, vol. 5, no. 4, pp. 266–70, Apr. 2010.

[4] M. Kläui, C. A. F. Vaz, J. Rothman, J. A. C. Bland, W. Wernsdorfer, G. Faini, and E. Cambril, "Domain Wall Pinning in Narrow Ferromagnetic Ring Structures Probed by Magnetoresistance Measurements," *Physical Review Letters*, vol. 90, no. 9, pp. 097202–1–4, Mar. 2003.

[5] C. C. Chen, C. C. Chang, Y. C. Chang, C. T. Chao, C .Y. Kuo, L. Horng, J. C. Wu, T. Wu, G. Chern, C. Y. Huang, M. Tsunoda, and M. Takahashi, "Angular Dependence of Magnetoresistance During Magnetization Reversal on Magnetic Tunnel Junction Ring," *IEEE Transactions on Magnetics*, vol. 43, no. 2, pp. 920–922, 2007.

[6] Mei-Feng Lai, Zung-Hang Wei, Ching-Ray Chang, J. C. Wu, J. H. Kuo, and Jun-Yang Lai, "Influence of vortex domain walls on magnetoresistance signals in Permalloy rings," *Physical Review B*, vol. 67, no. 10, pp. 104419–1–5, Mar. 2003.

[7] S. Lepadatu, J. S. Claydon, C. J. Kinane, T. R. Charlton, S. Langridge, A. Potenza, S. S. Dhesi, P. S. Keatley, R. J. Hicken, B. J. Hickey, and

C. H. Marrows, "Domain-wall pinning, nonadiabatic spin-transfer torque, and spin-current polarization in permalloy wires doped with vanadium," *Physical Review B*, vol. 81, no. 2, pp. 020413–1–4, Jan. 2010.

[8] T. Haug, K. Perzlmaier, and C. H. Back, "In situ magnetoresistance measurements of ferromagnetic nanocontacts in the Lorentz transmission electron microscope," *Physical Review B*, vol. 79, no. 2, pp. 024414–1–6, Jan. 2009.

[9] L. K. Bogart and D. Atkinson, "Domain wall anisotropic magnetoresistance in planar nanowires," *Applied physics Letters*, vol. 94, no. 4, pp. 042511–1–3, 2009.

[10] T. Arnal, A. Khvalkovskii, M. Bibes, B. Mercey, Ph. Lecoeur, and A.-M. Haghiri-Gosnet, "Electronic properties of domain walls in La2/3Sr1/3MnO3: Magnetotransport measurements on a nanopatterned device," *Physical Review B*, vol. 75, no. 22, pp. 220409, June 2007.

[11] C. Rüster, T. Borzenko, C. Gould, G. Schmidt, L. W. Molenkamp, X. Liu, T. J. Wojtowicz, J. K. Furdyna, Z. G. Yu, and M. E. Flatté, "Very Large Magnetoresistance in Lateral Ferromagnetic (Ga,Mn)As Wires with Nanoconstrictions," *Physical Review Letters*, vol. 91, no. 21, pp. 216602–1–4, Nov. 2003.

[12] U. Ebels, A. Radulescu, Y. Henry, L. Piraux, and K. Ounadjela, "Spin accumulation and domain wall magnetoresistance in 35 nm Co wires," *Physical review letters*, vol. 84, no. 5, pp. 983–986, Jan. 2000.

[13] Andrei Sokolov, Chunjuan Zhang, Evgeny Y Tsymbal, Jody Redepenning, and Bernard Doudin, "Quantized magnetoresistance in atomic-size contacts," *Nature nanotechnology*, vol. 2, pp. 171–175, 2007.

[14] M. I. Montero, R. K. Dumas, G. Liu, M. Viret, O. M. Stoll, W. A. A. Macedo, and Ivan K. Schuller, "Magnetoresistance of mechanically stable Co nanoconstrictions," *Physical Review B*, vol. 70, no. 18, pp. 184418–1–5, Nov. 2004.

[15] J. L. Tsai, S. F. Lee, Y. D. Yao, C. Yu, and S. H. Liou, "Magnetoresistance study in thin zig zag NiFe wires," *Journal of Applied Physics*, vol. 91, no. 10, pp. 7983–7985, 2002.

[16] Y. B. Xu, C. A. F. Vaz, A. Hirohata, H. T. Leung, C. C. Yao, J. A. C. Bland, E. Cambril, F. Rousseaux, and H. Launois, "Magnetoresistance of a domain wall at a submicron junction," *Physical Review B*, vol. 61, no. 22, pp. R14901–14904, June 2000.

[17] A. Ruotolo, A. Oropallo, F. Miletto Granozio, G. P. Pepe, P. Perna, U. Scotti Di Uccio, and D. Pullini, "Current-induced domain wall depinning and magnetoresistance in La0.7Sr0.3MnO3 planar spin valves," *Applied Physics Letters*, vol. 91, no. 13, pp. 132502–1–3, 2007.

[18] D. Claudio-Gonzalez, M. K. Husain, C. H. de Groot, G. Bordignon, T. Fischbacher, and H. Fangohr, "Journal of Magnetism and Magnetic Materials Fabrication and simulation of nanostructures for domain wall magnetoresistance studies on nickel," *Journal of Magnetism and Magnetic Materials*, vol. 322, pp. 1467–1470, 2010.

[19] P Bruno, "Geometrically Constrained Magnetic Wall," *Physical Review Letters*, vol. 83, no. 12, pp. 2425–2428, 1999.

[20] A. I. Morosov and A. S. Sigov, "Domain wall contribution to the magnetoresistance of magnetic multilayers," *Journal of Magnetism and Magnetic Materials*, vol. 272-276, pp. e1439–e1440, 2004.

[21] J. Ieda, S. Takahashi, M. Ichimura, H. Imamura, and S. Maekawa, "Spin accumulation and resistance due to a domain wall," *Journal of Magnetism and Magnetic Materials*, vol. 310, pp. 2058–2060, Mar. 2007.

[22] J. M. van Ruitenbeek, A. Alvarez, I. Pineyro, C. Grahmann, P. Joyez, M. H. Devoret, D. Esteve, and C. Urbina, "Adjustable nanofabricated atomic size contacts," *Review of Scientific Instruments*, vol. 67, no. 1, pp. 108–111, 1996.

[23] Hongkun Park, Andrew K. L. Lim, A. Paul Alivisatos, Jiwoong Park, and Paul L. McEuen, "Fabrication of metallic electrodes with nanometer separation by electromigration," *Applied Physics Letters*, vol. 75, no. 2, pp. 301–303, 1999.

[24] A. F. Morpurgo, C. M. Marcus, and D. B. Robinson, "Controlled fabrication of metallic electrodes with atomic separation," *Applied Physics Letters*, vol. 74, no. 14, pp. 2084–2086, 1999.

[25] B. Doudin and M. Viret, "Ballistic magnetoresistance?," *Journal of Physics: Condensed Matter*, vol. 20, no. 8, pp. 083201–1–18, 2008.

[26] W. F. Egelhoff Jr, L. Gan, H. Ettedgui, Y. Kadmon, C. J. Powell, P. J. Chen, A. J. Shapiro, R. D. McMichael, J. J. Mallett, and T. P. Moffat, "Artifacts that mimic ballistic magnetoresistance," *Journal of Magnetism and Magnetic Materials*, vol. 287, pp. 496–500, Feb. 2005.

[27] S. H. Flórez, *Domain Wall Engineering of Nanoscale Ferromagnetic Elements and its Application for Memory Devices*, Ph.D. thesis, University of Maryland, 2006.

[28] D. C. Gonzalez, *Design, Fabrication and Characterization of Magnetic Nanostructures*, Ph.D. thesis, University of Southampton, School of Electronics and Computer Science, 2008.

[29] F. Bloch, "Zur theorie des austauschproblems und der remanenzerscheinung der ferromagnetika," *Z. Phys.*, vol. 74, no. 5-6, pp. pp. 295–335, 1932.

[30] Hans Fangohr, Jurgen P. Zimmermann, Richard P. Boardman, David C. Gonzalez, and Cornelis H. de Groot, "Numerical investigation of domain walls in constrained geometries," *Journal of Applied Physics*, vol. 103, no. 7, pp. 07D926–1–3, 2008.

[31] C. Hassel, S. Stienen, F. M. Römer, R. Meckenstock, G. Dumpich, and J. Lindner, "Resistance of domain walls created by means of a magnetic force microscope in transversally magnetized epitaxial Fe wires," *Applied Physics Letters*, vol. 95, no. 03, pp. 032504–1–3, 2009.

[32] Y. Murakami, H. Kasai, J. J. Kim, S. Mamishin, D. Shindo, S. Mori, and A. Tonomura, "Ferromagnetic domain nucleation and growth in colossal magnetoresistive manganite," *Nature Nanotechnology*, vol. 5, pp. 37–41, 2009.

[33] A. Mougin, M. Cormier, J. P. Adam, P. J. Metaxas, and J. Ferré, "Domain wall mobility , stability and Walker breakdown in magnetic nanowires," *Europhysics Letters*, vol. 78, pp. 57007–p1–6, 2007.

[34] S. H. Florez, M. Dreyer, K. Schwab, C. Sanchez, and R. D. Gomez, "Magnetoresistive effects in planar NiFe nanoconstrictions," *Journal of Applied Physics*, vol. 95, no. 11, pp. 6720, 2004.

[35] S. H. Florez, C. Krafft, and R. D. Gomez, "Spin-current-induced magnetization reversal in magnetic nanowires with constrictions," *Journal of Applied Physics*, vol. 97, no. 10, pp. 10C705, 2005.

[36] S. Lepadatu, O. Wessely, A. Vanhaverbeke, R. Allenspach, A. Potenza, H. Marchetto, T. R. Charlton, S. Langridge, S. S. Dhesi, and C. H. Marrows, "Domain-wall spin-torque resonators for frequency-selective operation," *Physical Review B*, vol. 81, no. 6, pp. 060402–1–4, Feb. 2010.

[37] M. Julliere, "Tunneling between ferromagnetic films ," *Physical Review A*, vol. 54, no. 3, pp. 225–226, 1975.

[38] T. Yaoi, S. Ishio, and T. Miyazaki, "Dependence of magnetoresistance on temperature and applied voltage in a 82Ni-Fe/Al-Al2O3/Co tunneling junction ," *Magnetism and Magnetic Materials*, vol. 54, no. 1-3, pp. 430–432, 1993.

[39] T. R. Mcguire and R. I. Potter, "Anisotropic Magnetoresistance in Ferromagnetic 3d Alloys," *IEEE Transactions on Magnetics*, vol. MAG-11, pp. 1018–1038, 1975.

[40] W. P. Pratt, SF Lee, JM Slaughter, R Loloee, P. A. Schroeder, and J. Bass, "Perpendicular giant magnetoresistances of Ag/Co multilayers," *Physical review letters*, vol. 66, no. 23, pp. 3060–3063, 1991.

[41] F. Muñoz Rojas, J. Fernández-Rossier, and J. J. Palacios, "Giant Magnetoresistance in Ultrasmall Graphene Based Devices," *Physical Review letters*, vol. 102, pp. 136810–1–4, 2009.

[42] Zisen Li, Cornelis De Groot, and Jagadeesh H Moodera, "Gallium oxide as an insulating barrier for spin-dependent tunneling junctions," *Applied Physics Letters*, vol. 77, no. 22, pp. 3630–3632, 2000.

[43] M N Khan, J Henk, and P Bruno, "Anisotropic magnetoresistance in Fe/MgO/Fe tunnel junctions," *Journal of Physics: Condensed Matter*, vol. 20, no. 15, pp. 155208, Apr. 2008.

[44] Enrique Cobas, Adam L Friedman, Olaf M J van 't Erve, Jeremy T Robinson, and Berend T Jonker, "Graphene as a tunnel barrier: graphene-based magnetic tunnel junctions.," *Nano letters*, May 2012.

[45] L. Sheng, D. Y. Xing, and D. N. Sheng, "Large magnetoresistance induced by quantum charge fluctuations in magnetic double dots," *Solid State Communications*, vol. 138, pp. 9–12, 2006.

[46] Ireneusz Weymann, Jürgen König, Jan Martinek, Józef Barnaś, and Gerd Schön, "Tunnel magnetoresistance of quantum dots coupled to ferromagnetic

leads in the sequential and cotunneling regimes," *Physical Review B*, vol. 72, no. 11, pp. 1–13, Sept. 2005.

[47] Kazuhito Tsukagoshi, BW Alphenaar, and Hiroki Ago, "Coherent transport of electron spin in a ferromagnetically contacted carbon nanotube," *Nature*, vol. 401, no. October, pp. 572, 1999.

[48] C. Feuillet-Palma, T. Delattre, P. Morfin, J. M. Berroir, G. Fève, D. C. Glattli, B. Plaçais, A. Cottet, and T. Kontos, "Conserved spin and orbital phase along carbon nanotubes connected with multiple ferromagnetic contacts," *Physical Review B*, vol. 81, no. 11, pp. 115414–1–8, 2010.

[49] Y. V. Nazarov and Y. M. Blanter, *Quantum Transport: Introduction to Nanoscience*, Cambridge Press, 2009.

[50] E. L. Nagaev, "Colossal-magnetoresistance materials : manganites and conventional ferromagnetic semiconductors," *Physics Reports*, vol. 346, pp. 387–531, 2001.

[51] Iosif G. Deac, Romulus Tetean, Istvan Balasz, and Emil Burzo, "Low-temperature magnetic ordering in the perovskites Pr1-xAxCoO3 (A=Ca, Sr)," *Journal of Magnetism and Magnetic Materials*, vol. 322, pp. 1185–1188, 2010.

[52] Soumen Mandal, "Magnetoresistance studies of La2/3Sr1/3MnO3 - YBa2Cu3O7 -La2/3Sr1/3MnO3 trilayers with ferromagnetic coupling along the nodal direction of YBa2Cu3O7," *Physical Review B*, vol. 81, no. 1, pp. 014515, 2010.

[53] Vilas Shelke, Subhash Khatarkar, Rashmi Yadav, Avneesh Anshul, and R. K. Singh, "Colossal magnetoresistance in La0.7Ca0.3-xHgxMnO3 System over wide temperature range," *Journal of Magnetism and Magnetic Materials*, vol. 322, pp. 1224–1227, 2010.

[54] H. Q. Yin, J. S. Zhou, K. Sugawara, and J. B. Goodenough, "Production and characteristics of La0.67Sr0.33MnO3 /La0.85Sr0.15MnO3 /La0.67Sr0.33MnO3 tri-layer tunneling magnetoresistance device," *Journal of Magnetism and Magnetic Materials*, vol. 222, pp. 115–120, 2000.

[55] Mark Johnson and R. H. Silsbee, "Interfacial Charge-Spin Coupling: Injection and Detection of Spin Magnetization in Metals," *Physical Review Letters*, vol. 55, no. 17, pp. 1790–1793, 1985.

[56] Qingtian Zhang, K. S. Chan, and Zijing Lin, "Spin current generation by adiabatic pumping in monolayer graphene," *Applied Physics Letters*, vol. 98, no. 3, pp. 032106, 2011.

[57] Jack Bass and William P Pratt, "Spin-diffusion lengths in metals and alloys, and spin-flipping at metal/metal interfaces: an experimentalists critical review," *Journal of Physics: Condensed Matter*, vol. 19, no. 18, pp. 183201, May 2007.

[58] Yasuhiro Fukuma, Le Wang, Hiroshi Idzuchi, Saburo Takahashi, Sadamichi Maekawa, and YoshiChika Otani, "Giant enhancement of spin accumulation and long-distance spin precession in metallic lateral spin valves.," *Nature materials*, vol. 10, no. 7, pp. 527–31, July 2011.

[59] Tao Yang, Takashi Kimura, and Yoshichika Otani, "Giant spin-accumulation signal and pure spin-current-induced reversible magnetization switching," *Nature Physics*, vol. 4, no. 11, pp. 851–854, Oct. 2008.

[60] S. Lepadatu and Y. B. Xu, "Discontinuous Resistance Change and Domain Wall Scattering in Patterned NiFe Wires With a Nanoconstriction," *IEEE Transactions on Magnetics*, vol. 40, no. 4, pp. 2688–2690, July 2004.

[61] S. Lepadatu and Y. Xu, "Direct Observation of Domain Wall Scattering in Patterned Ni80Fe20 and Ni Nanowires by Current-Voltage Measurements," *Physical Review Letters*, vol. 92, no. 12, pp. 12720, Mar. 2004.

[62] D a Allwood, G Xiong, C C Faulkner, D Atkinson, D Petit, and R P Cowburn, "Magnetic domain-wall logic.," *Science (New York, N.Y.)*, vol. 309, no. 5741, pp. 1688–92, Sept. 2005.

[63] K. Miyake, K. Shigeto, K. Mibu, T. Shinjo, and T. Ono, "Geometrical confinement of a domain wall in a nanocontact between two NiFe wires," *Journal of Applied Physics*, vol. 91, no. 5, pp. 3468–3470, 2002.

[64] C Yu, S. F. Lee, Y. D. Yao, M. S. Wong, E. W. Huang, Y. R. Ma, J. L. Tsai, and C. R. Chang, "Fabrication and physical properties of permalloy nano-size wires," *Physica B*, vol. 327, pp. 247–252, Apr. 2003.

[65] L. Gao, L. Yuan, L. Nicholl, R. Sabirianov, Z. Y. Liu, S. Adenwalla, and S. H. Liou, "Domain structure and magnetoresistance in Ni81Fe19 zigzag wires," *Journal of Magnetism and Magnetic Materials*, vol. 272-276, pp. E1301–E1303, May 2004.

[66] M. C. Hickey, D. Atkinson, C. H. Marrows, and B. J. Hickey, "Controlled domain wall nucleation and resulting magnetoresistance in Ni81Fe19 nanoconstrictions," *Journal of Applied Physics*, vol. 103, no. 7, pp. 07D518, 2008.

[67] José Prieto, Mark G. Blamire, and Jan E. Evetts, "Magnetoresistance in a Constricted Domain Wall," *Physical Review Letters*, vol. 90, no. 2, pp. 027201–1–4, Jan. 2003.

[68] Katsuyoshi Matsushita, Jun Sato, and Hiroshi Imamura, "Magnetic Structure of Domain Walls Confined in a Nano-Oxide Layer," *IEEE Transactions on Magnetics*, vol. 44, no. 11, pp. 2616–2619, 2008.

[69] Jun Sato, Katsuyoshi Matsushita, and Hiroshi Imamura, "The origin of dispersion of magnetoresistance of a domain wall spin valve," *Journal of Physics: Conference Series*, vol. 200, no. 6, pp. 062023, Jan. 2010.

[70] Azar Maalouf, Michel Gadonna, and Dominique Bosc, "An improvement in standard photolithography resolution based on Kirchhoff diffraction studies," *Journal of Physics D: Applied Physics*, vol. 42, no. 1, pp. 015106, Jan. 2009.

[71] E. Slot, M. J. Wieland, G. de Boer, P. Kruit, G. F. ten Berge, a. M. C. Houkes, R. Jager, T. van de Peut, J. J. M. Peijster, S. W. H. K. Steenbrink, T. F. Teepen, a. H. V. van Veen, and B. J. Kampherbeek, "MAPPER: high throughput maskless lithography," *Proceedings of SPIE*, vol. 6921, pp. 69211P–1–9, 2008.

[72] Nezih Unal, Martin D.B. Charlton, Yudong Wang, Ulrike Waizmann, Thomas Reindl, and Ulrich Hofmann, "Easy to adapt electron beam proximity effect correction parameter calibration based on visual inspection of a Best Dose Sensor," *Microelectronic Engineering*, vol. 88, no. 8, pp. 2158–2162, Aug. 2011.

[73] Jingyue Liu, "H igh-Resolution and Low-Voltage FE-SEM Imaging and Microanalysis in Materials Characterization," *Materials characterization*, vol. 44, pp. 353–363, 2000.

[74] D. C. Joy, "SMART a program to measure SEM resolution and imaging performance," *October*, vol. 208, pp. 24–34, 2002.

[75] D. C. Bell, M. C. Lemme, L. A. Stern, J. R. Williams, and C. M. Marcus, "Precision cutting and patterning of graphene with helium ions.," *Nanotechnology*, vol. 20, no. 45, pp. 455301, Nov. 2009.

[76] S A Boden, Z Moktadir, D M Bagnall, H Mizuta, and H N Rutt, "Microelectronic Engineering Focused helium ion beam milling and deposition," *Microelectronic Engineering*, vol. 88, no. 8, pp. 2452–2455, 2011.

[77] Max C Lemme, David C Bell, James R Williams, Lewis A Stern, Britton W H Baugher, Pablo Jarillo-herrero, and Charles M Marcus, "Etching of Graphene Devices with a Helium Ion Beam," *ACS Nano*, vol. 3, no. 9, pp. 2674–2676, 2009.

[78] Jijin Yang, David C Ferranti, Lewis A Stern, Colin A Sanford, Jason Huang, Zheng Ren, Lu-chang Qin, and Adam R Hall, "Rapid and precise scanning helium ion microscope milling of solid-state nanopores for biomolecule detection," *Nanotechnology*, vol. 285310, 2011.

[79] J. F. Zeigler, J. P. Biersack, and U. Littmark, "The Stopping and Range of Ions in Solids.," 1985.

[80] J. P. Biersack and L. G. Haggmark, "A Monte Carlo Computer Program for the Transport of Energetic Ions in Amorphous Targets," pp. 257–269, 1980.

[81] S. A. Boden, Z. Moktadir, F. M. Alkhalil, H. Mizuta, H. N. Rutt, and D. M. Bagnall, "Nanofabrication with the Helium Ion Microscope," in *MRS Proceedings Fall Meeting*. 2011, p. in press, MRS.

[82] Richard Livengood, Shida Tan, Yuval Greenzweig, John Notte, and Shawn McVey, "Subsurface damage from helium ions as a function of dose, beam energy, and dose rate," *Journal of Vacuum Science & Technology B: Microelectronics and Nanometer Structures*, vol. 27, no. 6, pp. 3244, 2009.

[83] M.D. Kluge and J.R. Ray, "Elastic constants and density of states of a molecular-dynamics model of amorphous silicon," *Physical Review B*, vol. 37, no. 8, pp. 4132, 1988.

[84] Larry Scipioni, David C. Ferranti, Vincent S. Smentkowski, and Radislav a. Potyrailo, "Fabrication and initial characterization of ultrahigh aspect ratio vias in gold using the helium ion microscope," *Journal of Vacuum Science & Technology B: Microelectronics and Nanometer Structures*, vol. 28, no. 6, pp. C6P18, 2010.

[85] J. R. Sambles, K. C. Elsom, and D. J. Jarvis, "The electrical resistivity of gold films," *Philosophical Transactions of the Royal Society of London. Series A, Mathematical and Physical Sciences*, vol. 304, no. 1486, pp. pp. 365–396, 1982.

[86] WL Roth, "Magnetic structures of MnO, FeO, CoO, and NiO," *Physical Review*, vol. 523, no. 1950, 1958.

[87] Andreas Knittel, Matteo Franchin, Farzad Nasirpouri, Simon J. Bending, and Hans Fangohr, "Effect of rounded corners on the magnetic properties of pyramidal-shaped shell structures," *Journal of Applied Physics*, vol. 111, no. 7, pp. 07D127, 2012.

[88] D. T. Ngo, M. C. Hickey, and D. McGrouther, "Formation of Magnetic Structure by Domain Wall Confinement in Nanoconstriction," *Magnetics, IEEE*, vol. 47, no. 10, pp. 2511–2514, 2011.

[89] Z. J. Yang, L. Sun, X. P. Zhang, M. Cao, X. Y. Deng, A. Hu, and H. F. Ding, "Control of ultranarrow Co magnetic domain wall widths in artificially patterned H-bar structures," *Applied Physics Letters*, vol. 94, no. 6, pp. 062514–1–3, 2009.

[90] Hans Fangohr, Dmitri S. Chernyshenko, Matteo Franchin, Thomas Fischbacher, and Guido Meier, "Joule heating in nanowires," *Phys. Rev. B*, vol. 84, pp. 054437, Aug 2011.

[91] Hyperphysics.phy-astr.gsu.edu, "Magnetic properties of ferromagnetic materials," Retrieved 25 - 4 - 2012.

[92] Leif J Sherry, Rongchao Jin, Chad a Mirkin, George C Schatz, and Richard P Van Duyne, "Localized surface plasmon resonance spectroscopy of single silver triangular nanoprisms.," *Nano letters*, vol. 6, no. 9, pp. 2060–5, Sept. 2006.

[93] T. H. Taminiau, F. D. Stefani, F. B. Segerink, and N. F. van Hulst, "Optical antennas direct single-molecule emission," *Nature Photonics*, vol. 2, no. 4, pp. 234–237, Mar. 2008.

[94] Mark L. Brongersma, "Engineering optical nanoantennas," *Nature Photonics*, vol. 2, pp. 270–272, 2008.

[95] N. Felidj, J. Aubard, G. Levi, J. R. Krenn, a. Hohenau, G. Schider, a. Leitner, and F. R. Aussenegg, "Optimized surface-enhanced Raman scattering on gold nanoparticle arrays," *Applied Physics Letters*, vol. 82, no. 18, pp. 3095, 2003.

[96] Hui Wang, Daniel W Brandl, Fei Le, Peter Nordlander, and Naomi J Halas, "Nanorice: a hybrid plasmonic nanostructure.," *Nano letters*, vol. 6, no. 4, pp. 827–32, Apr. 2006.

[97] Weihua Zhang, Xudong Cui, Boon-Siang Yeo, Thomas Schmid, Christian Hafner, and Renato Zenobi, "Nanoscale roughness on metal surfaces can increase tip-enhanced Raman scattering by an order of magnitude.," *Nano letters*, vol. 7, no. 5, pp. 1401–5, May 2007.

[98] Lavinia Rogobete, Franziska Kaminski, Mario Agio, and Vahid Sandoghdar, "Design of plasmonic nanoantennae for enhancing spontaneous emission.," *Optics letters*, vol. 32, no. 12, pp. 1623–5, June 2007.

[99] Lukas Novotny, "Effective Wavelength Scaling for Optical Antennas," *Physical Review Letters*, vol. 98, no. 26, pp. 1–4, June 2007.

[100] Holger Fischer and Olivier J F Martin, "Engineering the optical response of plasmonic nanoantennas.," *Optics express*, vol. 16, no. 12, pp. 9144–54, June 2008.

[101] Andrea Alù and Nader Engheta, "Tuning the scattering response of optical nanoantennas with nanocircuit loads," *Nature Photonics*, vol. 2, no. 5, pp. 307–310, Apr. 2008.

[102] Ertugrul Cubukcu, Eric a. Kort, Kenneth B. Crozier, and Federico Capasso, "Plasmonic laser antenna," *Applied Physics Letters*, vol. 89, no. 9, pp. 093120, 2006.

[103] O L Muskens, V Giannini, J a Sánchez-Gil, and J Gómez Rivas, "Optical scattering resonances of single and coupled dimer plasmonic nanoantennas," *Optics express*, vol. 15, no. 26, pp. 17736–46, Dec. 2007.

[104] Martina Abb, Pablo Albella, Javier Aizpurua, and Otto L Muskens, "All-optical control of a single plasmonic nanoantenna-ITO hybrid.," *Nano letters*, vol. 11, no. 6, pp. 2457–63, June 2011.

[105] J. N. Farahani, D. W. Pohl, H.-J. Eisler, and B. Hecht, "Single Quantum Dot Coupled to a Scanning Optical Antenna: A Tunable Superemitter," *Physical Review Letters*, vol. 95, no. 1, pp. 1–4, June 2005.

[106] Jörg Merlein, Matthias Kahl, Annika Zuschlag, Alexander Sell, Andreas Halm, Johannes Boneberg, Paul Leiderer, Alfred Leitenstorfer, and Rudolf

Bratschitsch, "Nanomechanical control of an optical antenna," *Nature Photonics*, vol. 2, no. 4, pp. 230–233, Mar. 2008.

[107] G. Leveque and Olivier J.F. Martin, "Tunable composite nanoparticle for plasmonics," *Optics letters*, vol. 31, no. 18, pp. 2750–2752, 2006.

[108] K. H. Su, Q. H. Wei, and X. Zhang, "Tunable and augmented plasmon resonances of AuSiO2Au nanodisks," *Applied Physics Letters*, vol. 88, no. 6, pp. 063118, 2006.

[109] Alberto G Curto, Giorgio Volpe, Tim H Taminiau, Mark P Kreuzer, Romain Quidant, and Niek F van Hulst, "Unidirectional emission of a quantum dot coupled to a nanoantenna.," *Science (New York, N.Y.)*, vol. 329, no. 5994, pp. 930–3, Aug. 2010.

[110] Jiasen Zhang, Jing Yang, Xiaofei Wu, and Qihuang Gong, "Electric field enhancing properties of the V-shaped optical resonant antennas," *Optics express*, vol. 15, no. 25, pp. 16852–9, Dec. 2007.

[111] T. T. Milligan, *Modern Antenna Design*, New York, 1985.

[112] Eyal Feigenbaum, Kenneth Diest, and Harry a Atwater, "Unity-order index change in transparent conducting oxides at visible frequencies.," *Nano letters*, vol. 10, no. 6, pp. 2111–6, June 2010.